

A robust real-time gait detection method for spinal cord injury rehabilitation

Hari Prasanth

Technische Universiteit Delft



A ROBUST REAL-TIME GAIT DETECTION METHOD FOR SPINAL CORD INJURY REHABILITATION

by

Hari Prasanth

in partial fulfillment of the requirements for the degree of

Master of Science
in Mechanical Engineering

at the Delft University of Technology,
to be defended publicly on Monday March 04, 2019 at 14:00.

Student number:	4619749	
Supervisors:	Prof. dr. H. Vallery,	TU Delft
	Dr. J. Zitzewitz,	GTXmedical
Thesis committee:	Dr. D. Dodou,	TU Delft
	Dr. M. Kok,	TU Delft
	Ir. P. M. Baines,	TU Delft

This thesis is confidential and cannot be made public until March 03, 2023.

An electronic version of this thesis is available at <http://repository.tudelft.nl/>.

ACKNOWLEDGEMENT

I am extremely thankful to my supervisor Dr. Joachim Von Zitzewitz (GTXmedical) for giving me this opportunity, always being available, listening with utmost patience and giving all the necessary support throughout the duration of the thesis. I am equally thankful to Prof. Heike Vallery (TU Delft) for spending her valuable time in giving regular supervision, critical feedback and comments.

I am grateful to Niek Borgers for being my daily supervisor during the early days of the project and Miro Caban (and the STIMO team) for taking the effort to provide those crucial patient datasets. I also acknowledge Maryse van't Klooster for sharing the necessary clinical information and ensuring anonymity of the patient datasets. I am also grateful to everyone else at GTXmedical for providing me a conducive environment to work with.

I am thankful to the fellow master students and PhD candidates at the Delft Bio robotics lab, especially Saher Jabeen and Christian Schumacher for their help and guidance during the data collection sessions. I would also like to thank my academic counsellor Lourdes Pujana for the valuable support during the toughest of times. I also acknowledge the time and effort spared by my good friends Ashwin George, Christine Palm, Davide Lombardo, Jesil John Kurian and Nathan Fopma in reviewing and/or proof reading this report.

Last, but not least, I am extremely thankful to my family for their valuable support both financially and emotionally throughout the course of my masters.

*Hari Prasanth
Delft, January 2019*

ABSTRACT

In a recent first-in-human clinical study, a therapy based on targeted epidural electrical stimulation together with body weight support has been validated to restore voluntary locomotion in chronically paralyzed subjects with Spinal Cord Injury (SCI). However, the system is currently open-loop controlled, meaning that the stimulation pattern cannot be influenced by the patient. Introducing closed-loop control with real-time motion feedback is expected to improve activity-based plasticity and thereby the therapy, to which this thesis will be contributing. To be specific, this thesis investigates the possibility of a robust real-time gait event detection method for SCI patients, to be used to synchronize the stimulation to movement in real-time. The gait of SCI patients deviates remarkably from the gait of a healthy subject. We identified several factors contributing to the deviation and studied them separately. Datasets were created by mimicking various walking scenarios observed from video references of patients from the ongoing clinical study. A robust real-time gait detection method with three variations of it – one using zero crossings of angular velocity in sagittal plane, another using high frequency contents extracted using wavelet transform and a third using additional trunk kinematics - is proposed and tested in this study with IMU signals from foot, shank and trunk. The results were promising when tested on the mimicked datasets and was then tested on the limited patients available. For patient with motor incomplete paralysis (AIS-D), the method seemingly identified events correctly 9 out of 10 times both for TO and HS detection. The performance dropped noticeably for TO detection (to around an F1 score of 0.24) for motor complete patient (AIS-B) while still maintaining the HS detection performance (at around an F1 score of 0.83). We conclude that patient-group-specific strategies might be necessary and that motor complete patients may require additional motion intention recognition strategies. In addition to this, a method to emulate IMU signals from motion capture datasets when limited number of markers are used, is also presented in this study, so as to be able to convert the already existing motion capture datasets to IMU datasets, and to time-synchronize these datasets explicitly when they are collected using independent sensors. Correlation values as high as 0.977 were observed between the emulated IMU signals (sagittal plane angular velocity) and that of the actual IMU signals.

LIST OF ABBREVIATIONS AND SYMBOLS

LIST OF ABBREVIATIONS

AIS	ASIA Impairment Score
ASIA	American Spinal Injury Association
BM	Benchmark Method
EES	Epidural Electrical Stimulation
GT	Ground Truth
HFC	High Frequency Content
HS	Heel Strike
IMU	Inertial Measurement Unit
ISw	Initial Swing
LR	Loading Response
MSt	Mid-Stance
MSw	Mid-Swing
PSw	Pre Swing
SCI	Spinal Cord Injury
St	Stance Phase
STFT	Short-Time Fourier Transform
STIMO	STImulation of Movement Overground
Sw	Swing Phase
TK	Trunk Kinematics
TO	Toe Off
TSt	Terminal Stance
TSw	Terminal Swing
UID	Unique IDentifier
WT	Wavelet Transform
ZC	Zero Crossing

LIST OF SYMBOLS

g	Acceleration due to gravity
\vec{a}_{st}	Accelerometer signal measured from a static IMU
\vec{a}_t	Accelerometer signal measured from trunk mounted IMU
\vec{a}_s	Accelerometer signal measured from shank mounted IMU
\vec{a}_f	Accelerometer signal measured from foot mounted IMU
\vec{a}_{th}	Accelerometer signal measured from thigh mounted IMU
$\vec{\omega}$	Angular velocity (vector form)

$\tilde{\omega}$	Angular velocity (matrix-vector form)
ω_t	Angular velocity signal in sagittal plane, measured from trunk mounted IMU
ω_s	Angular velocity signal in sagittal plane, measured from shank mounted IMU
ω_f	Angular velocity signal in sagittal plane, measured from foot mounted IMU
$\omega_{t,FP}$	Angular velocity signal in frontal plane, measured from trunk mounted IMU

CONTENTS

1	Introduction	1
1.1	Background and motivation	1
1.2	State of the art	4
1.3	Research questions	9
1.4	Contribution and outline of study	10
2	Methods	11
2.1	Data	11
2.1.1	Data from clinical study and open database	11
2.1.2	New dataset collection based on patient video references	12
2.2	Gait detection	12
2.2.1	Investigating the prominent features	12
2.2.2	Method design: heuristics-based gait detection	16
2.2.3	Method testing	18
2.3	IMU emulation	18
2.3.1	Rotation matrix and axis stability	19
2.3.2	Angular velocity and linear acceleration in body-fixed frame	20
2.3.3	Time synchronization	23
3	Results	25
3.1	Gait detection	25
3.1.1	Zero crossing with peak heuristics	25
3.1.2	High frequency content with peak heuristics	25
3.1.3	Trunk kinematics with peak heuristics	27
3.1.4	Benchmarking	29
3.1.5	Testing with patient datasets	30
3.2	IMU emulation	33
3.2.1	Segment axis stability	33
3.2.2	Creating synthetic IMU data	33
3.2.3	Time synchronizing IMU and motion capture data	33
4	Discussion	35
4.1	Gait detection	35
4.1.1	Peak heuristics improves robustness	35
4.1.2	Foot IMU signal alone may be insufficient for SCI gait detection	36
4.1.3	Shank/trunk kinematics enhances robustness of heel strike prediction	36
4.1.4	Wavelet transform might be unsuitable for real-time applications	37
4.1.5	Limitations of the mimicked dataset	37
4.1.6	Causal dilemma: patient-group-specific strategies might be necessary	38
4.2	IMU emulation	38
4.2.1	Angular velocity	38
4.2.2	Linear acceleration	38
4.2.3	Time synchronization	39
4.3	Conclusion and future work	39
A	Wavelet Transform	41
A.1	Introduction	41
A.2	Theory	41
A.3	Wavelet transform illustration	43
A.4	Wavelet transform and gait signals	45
A.5	Cone of influence and inherent delay	47

B	Supplementary Images	49
C	MATLAB Script And Settings	53
C.1	Simulated real-time environment	53
C.2	MATLAB built-in function settings	54
	Bibliography	55

1

INTRODUCTION

1.1. BACKGROUND AND MOTIVATION

SPINAL CORD INJURY

Bipedal walking in human beings is a complex task involving real-time control of hundreds of muscles working in synergy with each other. The resulting smooth movement is aided through bones, joints and ligaments, and coordinated through millions of neurons in the brain and the spinal cord. This cannot happen without taking real-time feedback from various sensors present throughout the body including vision, vestibular, proprioceptive and tactile feedback. We almost always do such a complex task of walking without having to think about each aspect of it consciously, thanks to involuntary tasks being carried out by brain and spinal cord in the background. Every year, nearly 500,000 people across the world lose this ability (to walk) resulting from traumatic Spinal Cord Injury (SCI) [1]. Post injury, their quality of life is significantly compromised [1].

Lesion induced in the spinal cord during injury results in detachment of neurons running down from the brain to the spinal cord, partially or completely, depending on the degree of injury. The location of injury decides which limbs will be affected [2]. For instance, a lesion around the lumbar segment in the spinal cord may lead to the subject becoming paraplegic while a lesion around the cervical segment may lead to the subject becoming tetraplegic [2]. The American Spinal Injury Association (ASIA) introduced the ASIA Impairment Score (AIS) to quantify the degree/severity of injury, ranging from AIS-A to AIS-E. AIS-A corresponds to complete sensory and motor impairment while AIS-E corresponds to normal sensory and motor functions, but with prior deficits [2]. Our further discussion will be limited to motor incomplete (chronic) paraplegic patients of the category AIS-B to AIS-D.

Potential treatment methods being researched include wearable exoskeletons [3], bone marrow cell transplantations [4], stem cell implantations [5],[6], Functional Electrical Stimulation (FES) [7],[8] and Epidural Electrical Stimulation (EES) [9], [10] of the spinal cord. This thesis will focus on an EES based therapy.

EPIDURAL ELECTRICAL STIMULATION AND STIMO CLINICAL STUDY

To reduce the chronic pain due to traumatic spinal cord injury, implantable electrical stimulators are often used. These Epidural Electrical Stimulation (EES) devices are used to send electrical signals to affected regions in the spinal cord for treatment of pain. Researchers are investigating the possibility of using such EES devices to activate the neurons going into the leg muscles, thereby re-enabling walking in patients with spinal cord injury [10]. (Note that this approach is different from FES where stimulation is given directly to the particular muscle(s) of interest [7], [8].)

Prof Gregoire Courtine and his team at EPFL have been researching innovative ways of restoring motor functions after neurological deficits such as spinal cord injury. They demonstrated the possibility of restoring voluntary control in rats with spinal cord injury, through a combination of spatio-temporal EES (as opposed to tonic stimulation used for pain relief) and robot assisted rehabilitation training [11]. The idea of spatio-temporal EES is to stimulate at the "right place" and at the "right time". Pre-clinical and early human research has identified precise stimulation sites in the spinal cord to induce left/right leg flexion and extension (the "right place"). By real-time motion feedback from sensors in the lower limbs, the timing of the stimulation pulses can be synchronized with the walking pattern (the "right time"). This opened up the possibility of a new treatment paradigm through which voluntary locomotion can be restored in chronic

SCI patients. STIMO (STimulation of Movement Overground) is a first-in-human study [9] from the team to demonstrate the feasibility of spatio-temporal EES in combination with overground robot assisted rehabilitation for improving recovery of lower limb motor functions for patients suffering from chronic SCI. The investigational device currently being used in the clinical study is illustrated in Figure 1.1. The rehabilitation process lasts several months and includes a pre-implantation period (up to 6 weeks), device implantation and optimization period (up to 6 weeks) and finally the over-ground rehabilitation training (for 5 to 6 months) which is done with the spatio-temporal EES and BWS. Coordination between muscles, necessary for walking, is achieved by selectively stimulating for certain duration, regions in the spinal cord that cater to the flexion and extension muscle groups of each joint [9]. The current system is largely open-loop controlled, which means the duration to which each muscle group should be stimulated in each gait cycle is pre-programmed (see Figure 1.2) and so the patient needs to adjust to the stimulation rather than the stimulation adjusting to the patient. This could be made more flexible by introducing a closed loop wherein the trigger of each stimulation block is decided on the go, based on gait events detected in real-time.

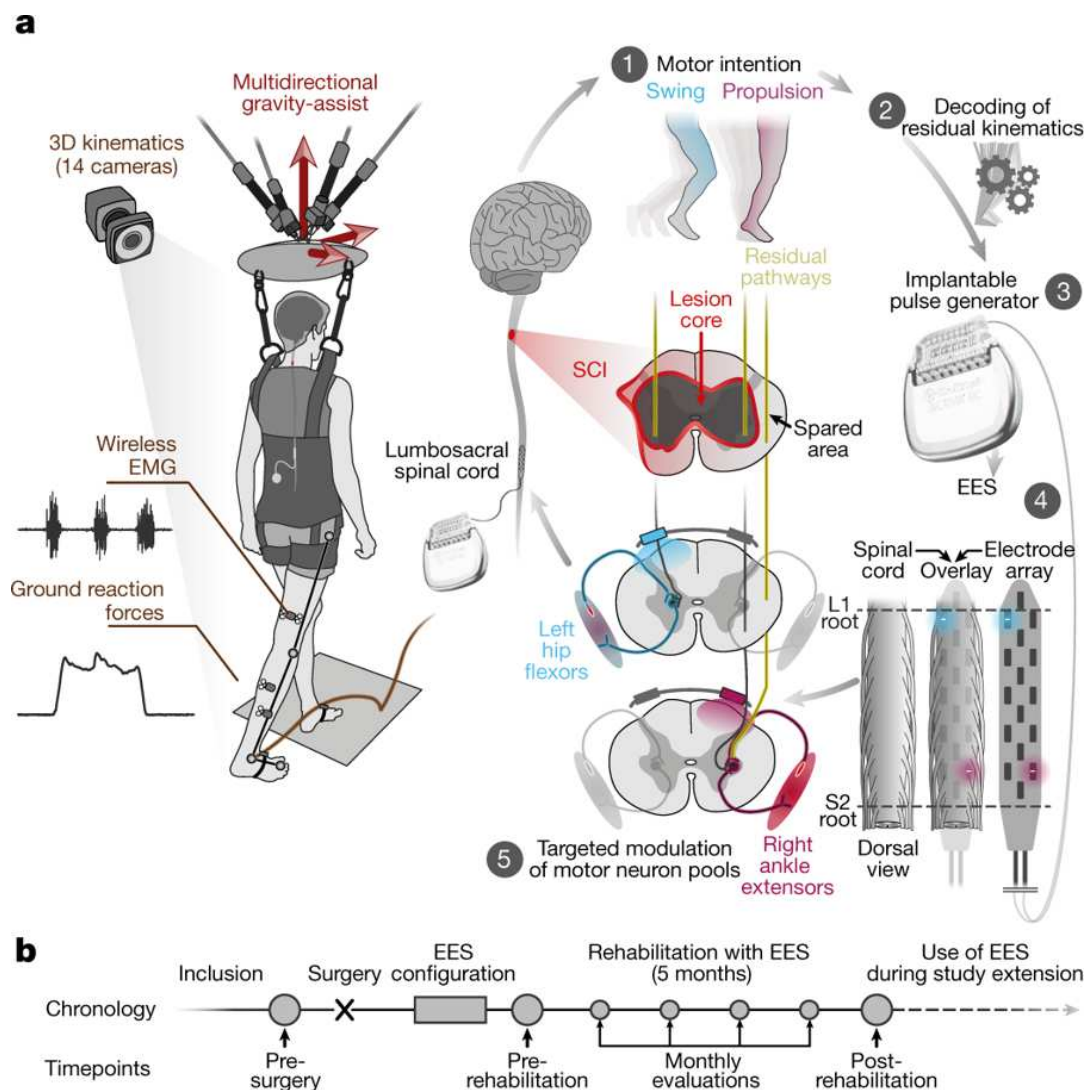


Figure 1.1: STIMO clinical study set up: The investigational device currently being used in the clinical study involves an overhead-mounted intent-driven Body Weight Support (BWS) system (RYSEN), a motion capture system (Vicon), a multi-electrode array (from Medtronic) implanted at the epidural space of the spinal cord and stimulated through an Implantable Pulse Generator (IPG) and the software system (running on a PC) controls the stimulation wirelessly. Image reprinted by permission from Springer Nature [9], © COPYRIGHT (2018).

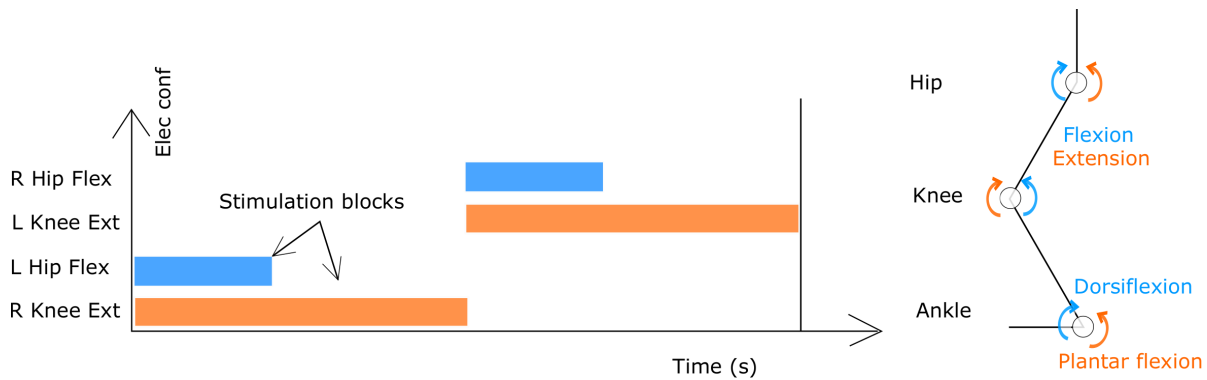


Figure 1.2: A simplified stimulation pattern for one full gait cycle is shown in the left figure. The stimulation begins with left leg swing phase (thus left hip flexion) during which the right leg should be in stance phase (thus right knee extension). During the second half of the gait cycle, the same pattern is repeated, but the other way around, as shown in the figure. The right figure shows the direction of flexion and extension for each joint.

GO-2

The current STIMO set up mentioned above is limited to laboratory environment. GO-2 is an integrated wearable solution being developed by GTX medical, a spin-off of EPFL that aims to bring this therapy to healthcare and extend the use of therapy beyond laboratories, such as for patients to train at home or even outdoors. To make the system wearable, GO-2 intends to replace the motion capture system with wearable sensors, primarily IMUs (see Figure 1.3). For reasons beyond the scope of this thesis, a 2 IMU configuration was preferred in the GO-2 system; one on each foot. During the course of this thesis, this was updated to a 3 IMU configuration, taking advantage of the motion controller at the abdomen to which the third (onboard) IMU could be added. The idea is to use these IMUs to estimate the gait events in real-time so as to enable closed-loop neuro-stimulation using the GO-2 system, which serves as the motivation for this thesis. It was also unclear at this point whether the choice of foot for IMU placement or addition of trunk kinematics are of any help for robust gait detection, which will also be investigated in this thesis.

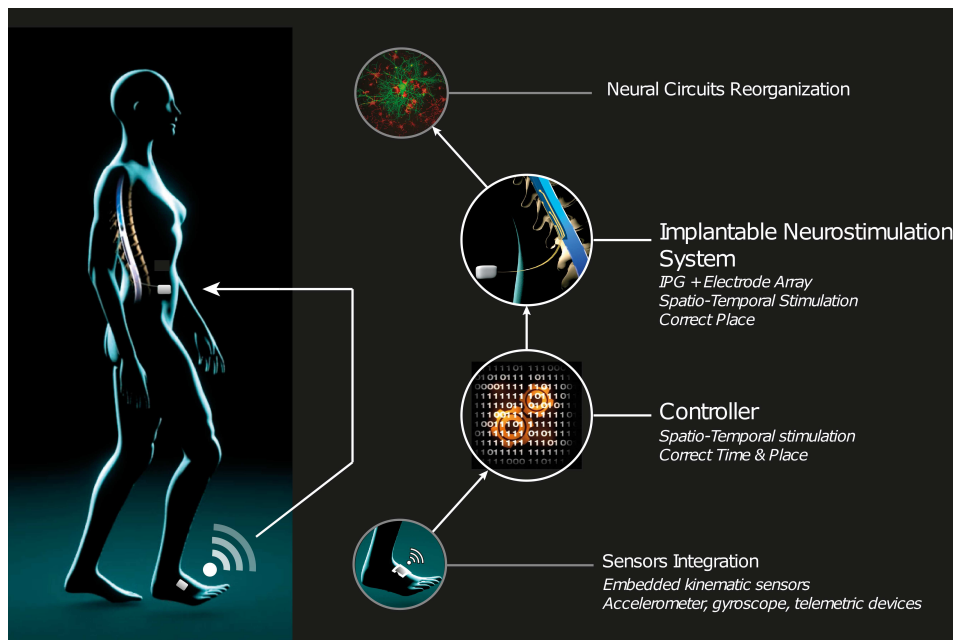


Figure 1.3: High-level representation of the GO-2 system. Notice that the motion capture system is replaced by wearable sensors (IMU).

1.2. STATE OF THE ART

A systematic review was carried out to identify a comprehensive list of gait detection methods used in literature. The study, carried out across five major scientific databases and after screening nearly a thousand articles through the PRISMA standard, identified several gait detection techniques as listed in Table 1.1. A detailed report of the study was submitted earlier as a separate deliverable [12], however, some relevant sections of the study will be discussed below briefly.

Domain	Algorithm	No. of studies		
Time domain	Tailor-Made Rule-Based Techniques (TMRB)	31 (11)	48	
	Fuzzy Inference System (FIS)	5 (2)		
	Machine Learning (ML)/ Pattern recognition	HMM		6 (2)
		kNN		1 (0)
		SVM		1 (1)
	Phase Portrait (PP)	1 (0)		
	Auto-correlation	1 (1)		
	Look-up table	1 (1)		
Other	1 (0)			
Frequency domain	Adaptive Oscillator (AO)	2 (0)	4	
	Spectral analysis	2 (0)		
Time-frequency domain	Short-Time Fourier Transform (STFT)	1 (0)	5	
	Wavelet Transform (WT)	3 (0)		
	Empirical Mode Decomposition (EMD)	1 (1)		

Table 1.1: Gait detection methods identified from the systematic review. Number of studies which involved pathological gait is listed in parenthesis for each category. (HMM - Hidden Markov Model, kNN - k Nearest Neighbours, SVM - Support Vector Machine).

TAILOR-MADE RULE-BASED METHOD

Tailor-Made Rule-Based (TMRB) methods are the most widely used gait detection techniques. It primarily includes threshold based, peak detection based and zero crossing based methods, often implemented through a set of custom rule-bases using if-else and (in)equality constraints. Simplicity, effectiveness and low computational complexity could be what led to nearly 60% of the studies (see Table 1.1) using TMRB in real-time environments with limited availability of computational resources. This motivated the investigation of the TMRB methods in detail.

Threshold-ing is the simplest rule-based approach used by many researchers for gait detection. Some of the simplest works such as [13] include distinguishing swing and stance phase using threshold on linear acceleration or angular velocity. This is based on the idea that at stance phase, the gravity-free acceleration components and the angular velocity of the foot are close to zero in a healthy gait. Although effective for healthy subjects, a simple threshold on angular velocity was observed to be not suitable for SCI gait, as observed by a previous master student in his report [14]. Instead of using hard-coded thresholds, [15] proposed an adaptive threshold-based method which automatically computes and updates the threshold in real-time through what they call "dynamics of sensor data". Dynamics of sensor data is calculated as the sum of magnitude of acceleration, change in acceleration and angular velocity, and is averaged over the last five data samples. This is used as an adaptive threshold to distinguish between swing and stance phases. According to the authors, such an approach helps in reducing spurious errors during the stance phase.

Angular velocity signals, particularly in the sagittal plane involves peaks which coincide with the occurrence of various gait phases; for instance, peaks corresponding to pre-swing and mid-swing in sagittal plane foot angular velocity (see Figure 1.4 for an overview of various gait phases in a healthy subject). Peak detection and cross-correlation between gait phases of both legs (ipsi-lateral Mid-Stance (MSt), Terminal Stance (TSt) and Pre-Swing (PSw) overlap with contra-lateral Initial Swing (ISw), Terminal Swing (TSw) and Loading Response (LR), respectively in the time domain) were used by [16] for gait detection and reported 99.8% detection reliability when tested with five healthy subjects walking on treadmill. A quasi-real-time method was proposed by [17], detecting peaks in derivative of filtered shank angular velocity profile to detect gait events. The method reported 100% detection reliability when tested on healthy subjects. In yet another method, [18] identified peaks in shank sagittal plane angular velocity together with a minimum threshold to identify Mid-Swing (MSw) and then in turn identified TO and HS as the LR peak and PSw peak respectively. The method reported 100% reliability when tested on healthy subjects, transfemoral and transtibial amputees (while wearing prosthetic devices) with an overall latency less than +/-50ms. It is to be noted that peak detection would have some inherent delay when used in real-time gait detection since one needs to wait until

a major portion of the falling edge of the peaks to appear (to confirm that it is a peak and also to ignore peaks with less prominence), before the peak and the corresponding gait event can be confirmed.

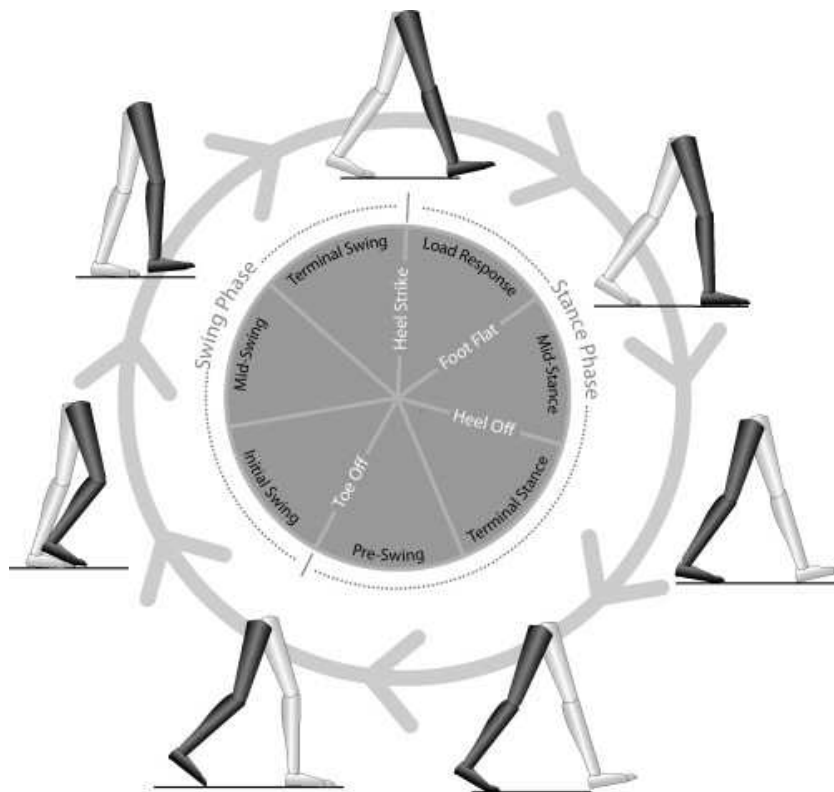


Figure 1.4: Illustration of gait phases and gait events. Image reprinted from [19], © Copyright (2018), with permission from Elsevier.

A zero crossing is the point where the angular velocity of the segment changes its direction (i.e. direction of rotation changes from clockwise to counter clockwise or vice-versa). The significance of zero-crossing associated with foot angular velocity in sagittal plane is that it is the point where the push-off by toe ends, resulting in toe-off event closely overlapping with zero-crossing (particularly at low cadence). Zero crossing of ankle angular velocity together with a threshold on hip angular velocity was used by [20] to identify HS while TO was identified based on the threshold of both hip and ankle angular velocity. Zero crossing of sagittal plane shank angular velocity was used by [16] to identify the onset of loading response peak as well as mid-swing peak. The study was tested only on healthy subjects and it can be noticed that the robustness of such a method relies on the assumption that the angular velocity curve crosses the zero line only at the two instances (near TO and HS). However, we noticed that this does not hold up well with pathological gaits as will be demonstrated later in this report. To the best of the author's knowledge, these are the only two studies that used zero crossing to identify gait events/phases while it can surprisingly be noticed that none of the studies used zero crossing to identify TO.

PHASE PORTRAIT

Continuous gait phase estimation using phase portrait was first proposed in a study carried out by [21]. The authors used the angle subtended by phase portrait (between sagittal plane segment angle and segment angular velocity) on the X-axis and tested it across all the three lower body segments (thigh, shank and foot). The success of the method relies on the "circle-ness" of the phase portrait, or in other words, how linearly and monotonically the chosen variable is increasing, thereby being representative of the continuous gait phase. They observed that the thigh phase angle is nearly monotonically increasing, but the raw signal had to be smoothed and scaled to be close to circular orbit. A quasi-real-time implementation of the method was tested on healthy subjects by [22] and reported satisfactory performance but was unclear about any latency introduced by the filtering (filtering was used to ensure the linearity of the phase portrait variable). It is also unclear how the method would hold up against pathological gait involving fast motion transitions and other artifacts. Nevertheless, the method in the current form was not considered a suitable solution for GO-2 since

IMU could not be used at the thigh and continuous gait phase estimation was not deemed necessary at this point.

ADAPTIVE OSCILLATOR

Real-time continuous gait phase estimation using adaptive oscillators was tested by [23] and [24]. However, both the versions were tested only on healthy gait (15 and 6 healthy subjects respectively). Although both methods reported satisfactory performance with healthy subjects, it was unclear how the method would hold up against impaired gait. An implementation of adaptive oscillator on SCI patients from the STIMO clinical study by a student from EPFL [25] has observed that the method did not result in satisfactory performance. It was reported that the method is only suitable for stable gait and that it would take around three gait cycles before it can start outputting reliable estimates of the gait phase. However, for the patients to be able to walk, this method needs to work in the first place, which is a causality dilemma. This was made worse by the fact that the STIMO clinical setup was restricted to a room where the patient can walk only few steady strides after which they have to make a turn (walking constrained to an elliptical path (see Figure 2.8), therefore cadence changes after every few steps), essentially not letting the gait cycles become steady. This observation of lack of robustness to fast motion transitions is not surprising, because frequency domain techniques are fundamentally based on decomposing the signal into infinitely long sinusoids as in the Fourier transform.

SHORT-TIME FOURIER TRANSFORM (STFT)

One way to extract cadence is through frequency spectrum analysis. The two prominent peaks in frequency spectrum analysis of gait signals (such as angular velocity of foot) corresponds to step frequency and stride frequency (first and second harmonics) from which cadence (steps/min) can be directly evaluated. However, to extract cadence in real-time, we need to perform Fourier transform (FT) over a window of data streamed continuously; the so-called short time Fourier analysis.

Extracting principal gait frequency automatically from frequency spectrum of single axis accelerometer when mounted at the abdomen lacks robustness according to [26]. For this reason, they used tri-axial cross-power spectrum analysis to remove unnecessary frequencies based on dominant frequencies in each axis. However, the robustness when the sensor is mounted at lower body segments such as thigh, shank or foot is not well documented in literature, either for the gyroscope or the accelerometer signal. An illustration of my own implementation of STFT in real-time, extracting the first and second harmonics is shown in Figure 1.5. The corresponding time-frequency domain plot is shown in Figure 1.6.

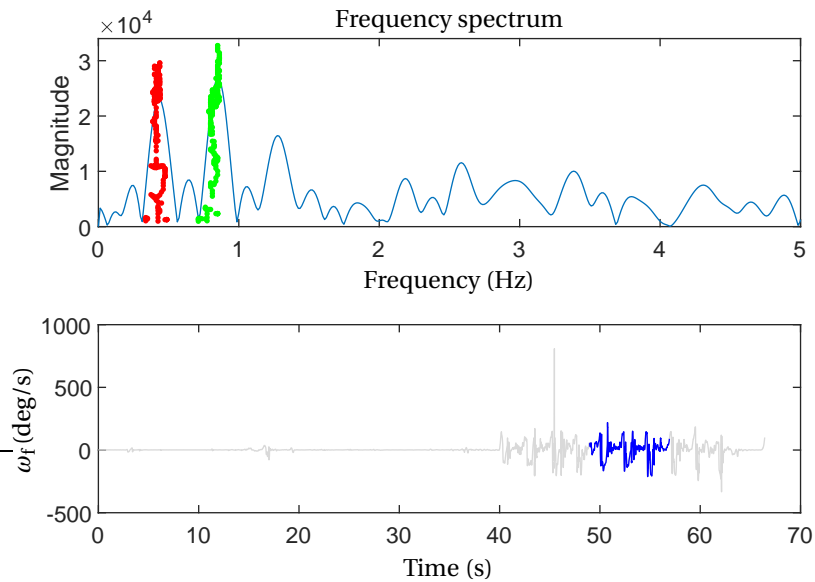


Figure 1.5: An illustration of STFT implementation in real-time. In the lower plot, the sagittal plane angular velocity (ω_f) of the foot is shown in grey and the window during the snapshot is highlighted in blue. In the upper plot, the frequency spectrum corresponding to the window at the moment is shown. The red dots represent path traced over the duration by the peak corresponding to the first harmonic (stride frequency) and the green represents the second harmonic (step frequency).

STFT suffers from the demerit that it has poor resolution in both time and frequency simultaneously ([27]). To improve the resolution in one domain, the resolution in the other domain has to be compromised.

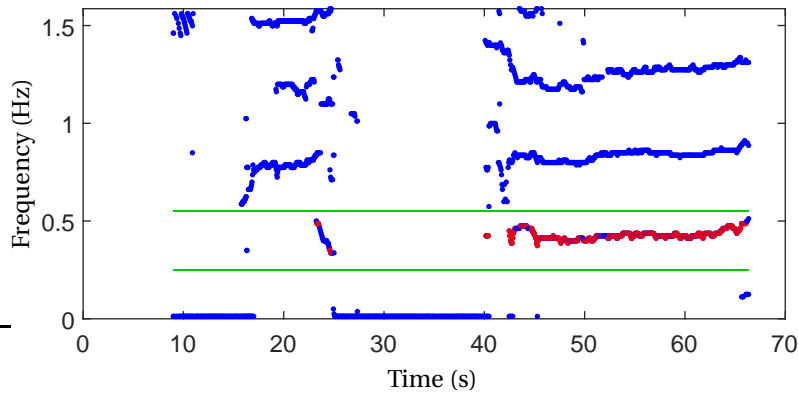


Figure 1.6: Time-frequency domain plot corresponding to Figure 1.5 is shown here. It can be observed that there is a clear separation between the first, second and third harmonics. The identified instances of first harmonic are marked in red dots.

For instance, to get better resolution of frequency content, we need to provide it with a larger time window of data, reducing the resolution in time domain and resulting in output cadence evaluated over a larger interval. Hence STFT can be considered as a suitable technique for long duration steady-state walking (quasi-periodic with no abrupt changes), but unsuitable for fast motion transitions ([27]).

WAVELET TRANSFORM

The aforementioned demerit of resolution dependence on each other can be overcome with Wavelet Transform (WT). Much like Fourier Transform (FT), WT also decomposes the signal in terms of a set of basis functions. While with Fourier transform, these basis functions are sinusoids, the basis functions in the case of WT are wavelets. The difference is that while sinusoids only differ in their frequencies, wavelets are localized both in time and frequency domain. Consequently, unlike STFT which uses windows of fixed size, WT allows variable window size, increasing the time resolution with high frequency signals and vice-versa (see Figure 1.7). The wavelet can be stretched/shrunk using a scale parameter and shifted along the time domain which is then multiplied by the signal and the transform is computed across the time domain. Readers who are unfamiliar with the method are encouraged to have a look at Appendix A for a better understanding of the method.

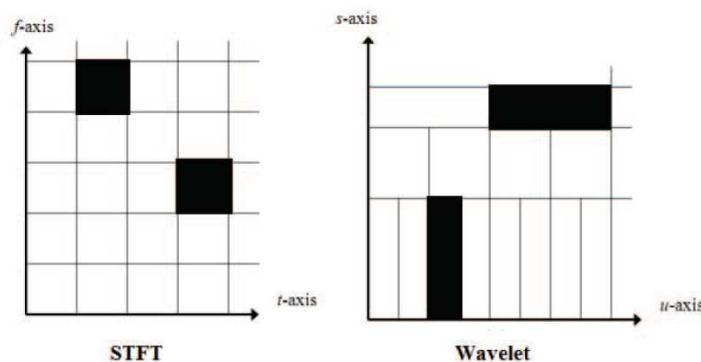


Figure 1.7: Contrasting WT with STFT: Illustrating the variation of window size with frequency in WT as opposed to constant window size in the case of STFT. The t and f axis in STFT refer to time and frequency axes and the squares refer to the resolution in each domain. The s and u axes refer to scale and shift parameters of WT which can be considered analogous to time and frequency axes (see Appendix A for more details.) © 2014 IEEE. Reprinted, with permission, from [27].

Previous studies in literature used wavelet transform for step detection and step frequency estimation. Step detection using Discrete Wavelet Transform (DWT) with Daubechies wavelet was carried out by [28] wherein the signal was drilled down into the so-called detail levels and then reconstructed with detail levels spread across 0.8 Hz to 3.2 Hz, followed by step detection using a threshold. A comparison study by [27] used DWT to extract step frequency/cadence and reports that WT performed better than STFT in estimating step frequency when fast motion changes occur. Note that there are two variants of DWT. The first variant, where the word 'discrete' implies discretized time and frequency (scale) domains while otherwise being identical to

Continuous Wavelet Transform (CWT) as described in [29] and implemented in [27] and the second variant, which is filter bank based as described in [30] and implemented in [28]. Note that MATLAB implementations of both version of DWT are available, but the former is called by the name `cwt` (because of its resemblance to CWT) while the latter is called by the name `dwt`. Although [28] and [27] carried out the study in real-time, these studies were limited to step detection and step frequency (and not intra-stride gait events).

TO and HS events consist of combined features that can be well resolved in time-frequency domain, according to [31]. They identified distinctive features in the shank angular velocity involving some medium and high frequency contents with sharp characteristic peaks as shown in Figure 1.8. DWT (filter bank based) with Coiflet wavelet of fifth order was used to enhance gait events in the signal, thereby enabling easier identification of global maxima/minima corresponding to the gait events followed by which customized rules were used to identify specific peaks within the locality to confirm TO and HS. Coiflet wavelet was chosen for its resemblance to the characteristic peaks noted. Although the study reported accurate temporal estimation of TO and HS, it is to be noted that the study was tested only on healthy subjects and was implemented only for offline analysis.

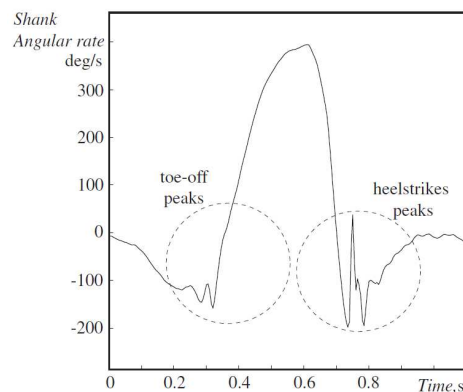


Figure 1.8: Characteristic peaks corresponding to HS and TO identified in shank angular velocity of healthy subjects. Image reprinted from [31], © Copyright (2018), with permission from Elsevier.

Although the three studies discussed before separately investigated WT in real-time for cadence and WT for gait event detection, neither of the three studies attempted WT in real-time for gait event detection. Because WT involves comparing the signal to wavelets, the transform at the beginning and end of the signal are less reliable since the wavelet cannot be overlapped completely with the extreme ends of the signal. This leads to the so called cone of influence, a region outside of which the result of wavelet transform is not reliable anymore (see Figure A.9). This is usually of low significance in offline analysis since the entire signal is available for analysis at once, and the transform at extreme ends is only affected. The longer the signal, the better it is. In the case of real-time gait event detection, the cone of influence becomes more significant since what we are interested in every iteration of the transform is the latest signal coming in and that is exactly where the reliability is poor (region outside of the cone of influence; see Figure A.9). However, it depends on how much close to real-time the system should be and what frequency components someone is interested in; the delay increases with lower frequency components and vice-versa. In the next chapter, we will build up on this idea to extract high frequency content of the signal, for real-time gait event detection.

MACHINE LEARNING

Machine learning (ML) methods are the second most widely used gait detection methods and are gaining more popularity in recent times as all eight studies are from 2012 or later. Hidden Markov Model (HMM) is the most favoured with six out of eight studies using it. Angular velocity in sagittal plane was the preferred signal for most studies; [32] used sagittal plane angular velocity from foot mounted IMU while [33] used sagittal plane angular velocity of thigh, shank and foot mounted IMUs as input to HMM. In both cases, insoles were used for creating the labelled dataset (ground truth) necessary for training the model. In yet another study, [34] used third order fast Fourier transform followed by Principal Component Analysis (PCA) for feature generation which was then fed to Support Vector Machine (SVM) classifier to identify the gait phases. The study used both insole and accelerometer as input signals, essentially making use of multi modal sensor fusion. The study considered five gait phases/events and reported 97.26% success rate for the Initial Contact (IC) event. Many of the studies fed data as individual gait cycles, segmenting them based on prominent peaks

in signals [35] which brought to our attention during the review that time series machine learning methods (for instance, Recurrent Neural Network (RNN) based methods such as Long Short-Term Memory (LSTM) units) are yet to be tested despite the data being time-series based. Over all, the tested machine learning techniques reported significantly higher accuracy with five out of six studies (that reported at least some quantitative metric) reporting above 95% accuracy. It is worth mentioning here that a previous study carried out by a student at EPFL tested a method that can begin learning with few training datasets and improve its model when more data is available; using Gaussian Mixture Regression (GMR) with particle filter [36]. But the method was not deemed successful for the intended application due to variability of SCI gait and that the performance only improves through online learning with sufficient data (performance at early stage is not expected to be good enough) making the early stage testing on human subjects difficult.

In this study, we will not consider machine learning methods due to lack of sufficient systematically collected datasets. Better and more systematic data collection protocols are being proposed for the upcoming STIMO-2 clinical trials to ensure that future datasets can be used to implement machine learning. Further, to convert the current motion capture datasets (based on a minimal set of markers) into corresponding IMU datasets, an IMU emulation method has been developed and tested in this study, as will be discussed later in Chapter 2, which will indeed result in conversion of more datasets to suitable form thus enabling machine learning.

STATE OF THE ART FROM A PATHOLOGICAL POINT OF VIEW

It was noted later in the study that the gait of SCI patients can essentially involve a combination of several gait pathologies including but not limited to gait asymmetry, toe walking, irregular gait, exaggerated hip flexion (similar to steppage gait) and foot crossing (caused by hip abductor under-stimulation similar to trendelenburg gait). A robust gait detection method that is expected to work for SCI gait should ideally be able to address all these "ingredient" gait pathologies. However, among the 52 studies identified from literature, none of those gait pathologies could be noticed. In fact, only one study catered to more than one type of pathological gait and only two studies had SCI patients, and neither of them exclusively based on IMUs (using other additional sensors such as insoles). Thus, it can be observed that the problem of real-time SCI gait detection using IMU is yet to be addressed. Since STIMO is the first-in-human study that is essentially "recreating" walking in paralyzed patients, it is understandably so that there is a dearth of research on gait detection with severely deviating gait patterns. There is thus a need to enhance robustness of gait detection in severely deviating gait patterns.

Healthy	Pathology	No. of studies	Algorithms
Healthy	-	29	TMRB(17), HMM(4), WT(3), Other(1), AO(2), spectral analysis(3), STFT(1), FIS(3)
-	-	6	TMRB (5), ML (1)
-	Parkinson's disease	3	TMRB(3), EMD(1)
Healthy	Amputee	3	TMRB(3)
Healthy	Parkinson's disease	2	TMRB(1), Auto-correlation (1)
Healthy	Hemiplegia	2	kNN(1), TMRB(1)
Healthy	Osteo-arthritis	1	SVM
Healthy	Hemiparetic, Huntington's	1	HMM(1)
Healthy	Stroke	1	TMRB(1)
Healthy	Stroke, SCI	1	TMRB (FSM)
-	SCI (complete SCI (at T7/8))	1	FIS
-	stroke	1	TMRB
-	Cerebral palsy	1	ANFIS

Table 1.2: Distribution of gait detection techniques based on the type of subjects involved in the study.

1.3. RESEARCH QUESTIONS

GAIT DETECTION

Primary motivation behind this thesis is to investigate the possibility of a robust real-time gait detection method using IMUs, to enable closed loop neuro-stimulation in SCI patients. Based on our discussions so far, the main questions we would like to find answers to are:

1. Can real-time gait detection methods based exclusively on IMUs be robust enough to support the rehabilitation of SCI patients?
2. Can the prominent features in IMU signals be made use of, in a computationally limited environment, towards a promising real-time gait detection solution for SCI patients?
3. Can wavelet transform provide a promising real-time gait detection solution?
4. Is placing IMU at the foot advantageous over placing it at the shank?
5. Can addition of trunk kinematics improve robustness of gait detection?

IMU EMULATION

GO-2 requires the gait detection methods to be based on IMU (wearable sensors), but the availability of IMU dataset of SCI patients is limited while a wealth of motion capture data is available from STIMO clinical trials. The IMU measures angular velocity and linear acceleration in body fixed frame (depending on the body segment to which the sensor is attached) while the motion capture system measures the position of markers with respect to the world frame. If we can emulate IMU data from motion capture data, this could enable the design of IMU based gait detection methods based on the currently available patient datasets.

Further, the IMU emulation technique to be developed could also be used for time synchronizing motion capture and IMU data. Currently, there are a few datasets where IMU data is collected together with mocap data during the same session but using independent devices and hence not necessarily time synchronized. Since both datasets measure different variables, in different frames of reference, it is difficult to time-synchronize them directly. However, if one of the two is converted to the same set of variables as the other, represented in the same frame of reference, the latency between both datasets could be easily identified and then that information could be used to time synchronize them explicitly.

The main questions we would like to find an answer to are:

1. Can we (reliably) emulate IMU dataset from motion capture dataset collected using a minimal set of markers?
2. Is there a way to time-synchronize IMU data with motion capture data?

1.4. CONTRIBUTION AND OUTLINE OF STUDY

The main contributions of the thesis are:

1. A robust real-time gait detection method based exclusively on IMUs for rehabilitation of paralysed SCI patients. Three variations of the method are discussed in this thesis, one based on zero crossings, one based on high frequency content extracted using wavelet transform and another one based on additional trunk kinematics.
2. A method to emulate IMU signals from motion capture data collected with minimal set of markers, and to time-synchronize IMU data with motion capture data explicitly.

This thesis is organised as follows. Chapter 2 discusses the sources of data, data generation and conversion of existing data to a suitable form using IMU emulation and the proposed gait detection method. Chapter 3 presents the results of the gait detection methods quantitatively and benchmark the performance with respect to another method from literature. It also presents the IMU emulation results. Finally, chapter 4 discusses the results and is followed by the conclusion. In Appendix A, wavelet transform is explained briefly for readers unfamiliar with the method.

2

METHODS

This chapter is organised as follows: In Section 2.1, (potential) sources of data for this study are described, in Section 2.2, the proposed gait detection method is described and finally, in Section 2.3, the IMU emulation method is described.

2.1. DATA

2.1.1. DATA FROM CLINICAL STUDY AND OPEN DATABASE

In this study, we are mainly interested in IMU datasets of trunk and lower body segments, with ground truth data. Primary source of data for this study was expected to be from the STIMO clinical study. However, data from STIMO study mainly involves (Vicon) motion capture data while, what is of interest here is IMU based dataset. Since the clinical study protocols were originally designed for motion capture dataset, collecting dataset based on IMU was not part of the routine data collection protocol for the clinical team. This limited the number of datasets available for development of GO-2's gait detection algorithms (which relies on IMUs). The limited STIMO datasets that were part of this study are listed in Table 2.1, which includes one dataset each from three patients with AIS scores varying from B to D. The availability of data pertaining to individual body segments differed between datasets as indicated in the table. Note that the third dataset (S3) was only available towards the latter half of this study.

Additionally, more STIMO datasets were available but either with only IMU data or with only motion capture data and/or video references. These datasets, although without IMU data, were still useful to us. It helped us study the gait of SCI patients which in turn helped us mimic the gait of these patients and to recreate similar datasets. This is discussed in Section 2.1.2.

Furthermore, various open (publicly available) databases were also investigated for suitable datasets (at least healthy subject IMU datasets with ground truth validation), including HuGaDB [37], Physionet [38] and

UID	AIS	Usage	Segments	Remark
D1	D	For testing IMU emulation method and gait detection method	Thigh, shank	IMU and motion capture data were time-synchronized. No toe marker was available. Thus motion capture data could not be used for labelling ground truth gait events
D2	C	For testing time-synchronization method (after performing IMU emulation)	Foot	IMU and motion capture data were collected independently and hence not explicitly time-synchronised
D3	B	For testing gait detection method	Thigh, shank and foot	IMU and motion capture data were explicitly time-synchronized. Ground truth gait events were labelled using motion capture data

Table 2.1: One dataset each of three SCI subjects from STIMO clinical trials were involved in our study, as indicated in the table. The corresponding ASIA Impairment Score (AIS) of the subject, the purpose for which the dataset was used, the lower body segments for which data was available and some general remarks about each dataset, are listed in the table.

CASIA [39]. But, none of these databases offered IMU based (impaired) gait data with ground truth validation that we could use in this study.

2.1.2. NEW DATASET COLLECTION BASED ON PATIENT VIDEO REFERENCES

Due to limited availability of data, absence of trunk kinematics data, and to study the SCI gait closely, it was decided to replicate various scenarios (deviating gait patterns) observed in patients after studying the video references from the STIMO clinical study. The mimicking was carried out by myself, reproducing 9 different scenarios at the BioMechaMotionLab, TU Delft. Table 2.2 provides a list of various walking scenarios included in the study and the rationale for the inclusion of each. This dataset is only intended to assess the feasibility of the proposed method and to have a better understanding of the "ingredients" that add to the complexity of SCI gait. The proposed method was later validated with the data from patients.

Some of the scenarios from the dataset are illustrated in Figure 2.1 with bounded plots showing the range of deviations. The first plot (S2) corresponds to normal walking (reference for a typical healthy gait cycle). Note how the profile changes towards the end of swing phase in S4 (toe walking). Although the plot of S5 (foot drag) shows the range of deviation, it does not completely highlight the intensity of deviation during foot drag. Thus, a more detailed plot showing a few gait cycles in this scenario is given in Figure 2.2. Although exaggerated hip flexion (S6) was mimicked using the right leg, the effect can be seen at the corresponding stance interval of left foot angular velocity signal as shown in the figure. Similar pattern of stance phase distortion is also observed when patients are using a walker (see Figure B.3).

UID	Walking scenario	Rationale for inclusion
S1	Low cadence, normal walking	The therapy is often prepared for low cadence walking with stride duration typically ranging from 2.4 to 3.4 s.
S2	Medium cadence, normal walking	To be used as the norm
S3	High cadence, normal walking	To understand the effects of high cadence and to test the robustness of the proposed method.
S4	Toe walking	It is common in SCI patients to have toe strike first as opposed to heel-strike in healthy subjects (heel strike may not even be present in a typical SCI gait)
S5	Foot drag	Foot drag is a common phenomenon observed in most of the SCI patients
S6	Exaggerated hip flexion	Although not common, during rehabilitation, physiotherapists occasionally adjust the therapy to exaggerate joint movements.
S7	Gait asymmetry	Very common in SCI patients
S8	Abruptly changing cadence	Certain gait detection methods have "inertia", in the sense that it takes a few steps before the method adapts to the new cadence (for instance, Adaptive oscillators and other frequency domain-based methods). The proposed methods are to be tested for their ability to adapt to fast motion changes
S9	Walking in elliptical path	The use of body weight support system means that the patient typically walks in an elliptical path in the clinical study center. This can impact the gait in multiple ways, including gradually changing the cadence and adapting step-length during the turns. Algorithms should not go awry in such scenarios

Table 2.2: Various walking scenarios replicated in the dataset collected at BioMechaMotion Lab, Delft. First column is the Unique Identifier (UID) which will be used here after to refer to the corresponding walking scenario listed in second column. Rationale for inclusion of each walking scenario in the dataset is briefly mentioned in the third column.

2.2. GAIT DETECTION

2.2.1. INVESTIGATING THE PROMINENT FEATURES

The mimicked dataset, as discussed in the previous section, was studied from various perspectives. This includes investigating the acceleration components, norm of the accelerometer signal, angular velocity components, pitch angle, low, mid and high frequency contents of these signals, phase portraits and also with short-time fourier transform and wavelet transform. Based on these investigations, a number of features

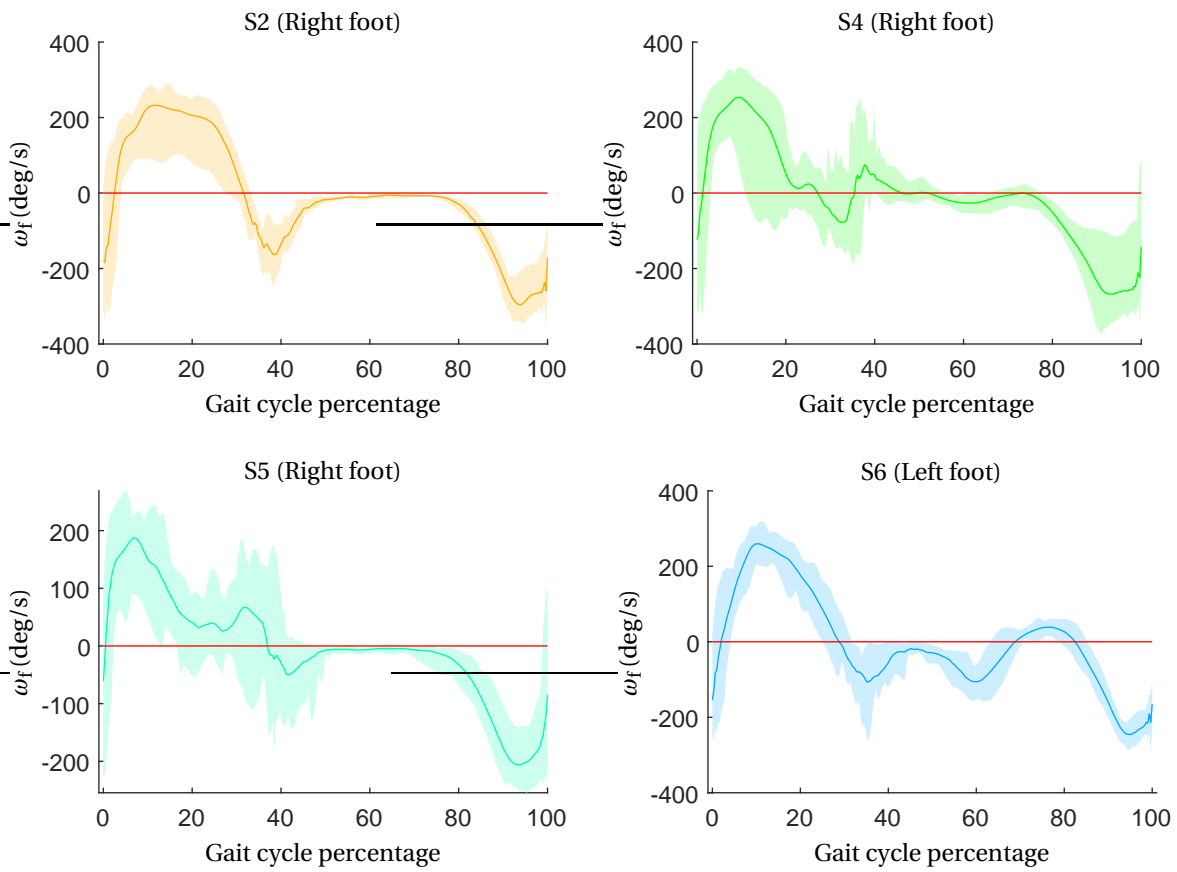


Figure 2.1: The bounded plots showing the variation in sagittal plane angular velocity of foot (ω_f) between gait cycles for some of the scenarios is shown in figure. The darker line through the middle corresponds to the mean plot while the red line corresponds to zero (for reference).

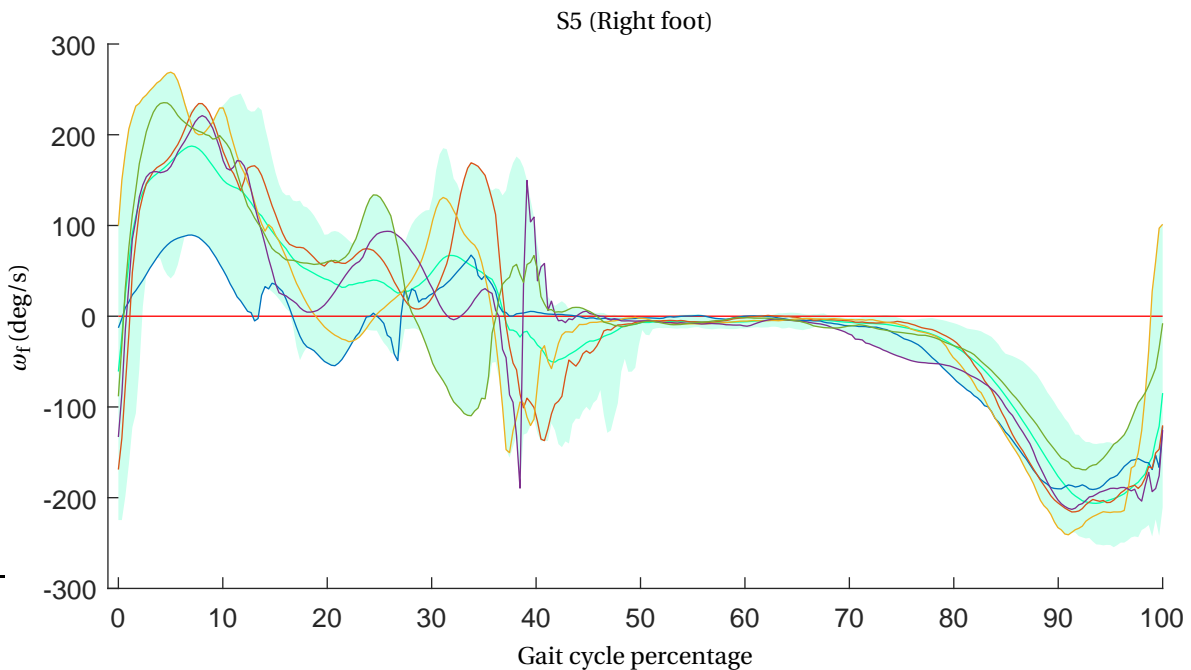


Figure 2.2: Bounded plot highlighting some of the significantly deviating gait patterns during Foot drag. Each line corresponds to a different gait cycle.

were observed to be common in several walking scenarios and thus it was decided to investigate those features across all datasets systematically, the results of which are illustrated in Table 2.3 for the foot.

The inclusion of high frequency content in this investigation was motivated by the fact that we observed a notable increase in high frequency content during foot-ground interaction, especially when the sensor is placed at the foot or the shank. This is also seconded by the fact that [31] noted a characteristic change in frequency during HS and TO, when tested with wavelet transform. The high frequency content in this study was extracted by first decomposing/transforming the signal (the angular velocity in sagittal plane or the norm of the accelerometer signal) into time-frequency domain as shown in the right plot in Figure 2.3. Then the high frequency region was condensed to one dimension by evaluating the cross section area of the magnitude of wavelet transform, resulting in clear sharp distinguishable peaks corresponding to the gait events as shown in the lower left plot in Figure 2.3. (For more insight into wavelet transform, see Appendix A).

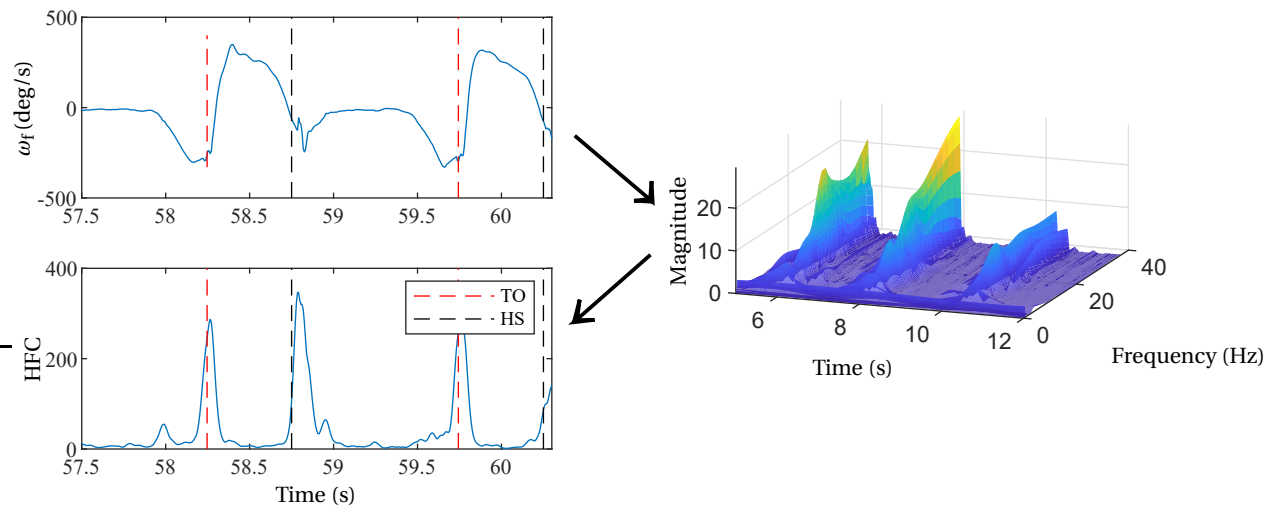


Figure 2.3: The Signal (top left plot) was first decomposed into time-frequency domain (right plot) and then the high frequency region was condensed to one dimension (bottom left plot) by evaluating the cross section area of the magnitude of wavelet transform.

Only the norm of the accelerometer signal is included in this study and not its components, as can be noted from Table 2.3. It makes the system more robust to sensor placement errors with respect to orientation (misalignment between body axes and sensor axes). The norm of the accelerometer signal will be the same value irrespective of how the sensor is oriented. It also helps improve the robustness of stance phase detection since the magnitude of the norm of the accelerometer signal during stance is now nothing but the acceleration due to gravity, thereby eliminating the necessity for calibration. If we were to follow component-wise accelerometer signal, acceleration due to gravity would be split between axes, making it necessary to estimate the component of gravity in each axis, since it would vary depending on how the sensor was placed on the patient each time.

For stance phase detection, two potential features were investigated; deviation in the norm of the accelerometer signal and deviation in the angular velocity during the mid-stance. During mid stance, both the norm of the accelerometer signal and the angular velocity are expected to be almost constant, at least in a healthy subject's gait. Here, we investigate them across all the scenarios to identify any deviations and to see if it is within acceptable ranges. We notice that angular velocity deviates significantly during S6 (exaggerated hip flexion), as illustrated earlier in Figure 2.1, while the norm of the accelerometer signal was observed to be still stable across all the scenarios during the mid-stance interval.

Thigh IMU signals were not part of this study. When we move from foot to shank angular velocity, the prominence of PSw peak decreases while that of MSw peak increases as can be noticed from Figure 2.4. And when we move further up, to the thigh, it can be noticed from the same figure that the two phases can barely be distinguished in thigh angular velocity profile. It is also demonstrated using wavelet transform analysis in Appendix A that the presence of high frequency content in the signal decreases as the sensor is placed higher up in the body. (This could be because frequencies are being naturally filtered out by the soft tissues of the body.) Thus, it was observed that high frequency contents are barely present in the thigh IMU signals. The 3 IMU configuration preferred by GO-2 with on-board IMU at trunk means that it is less advantageous to trade

off foot or shank IMU for thigh IMU. For this reason, the thigh was not part of this study.

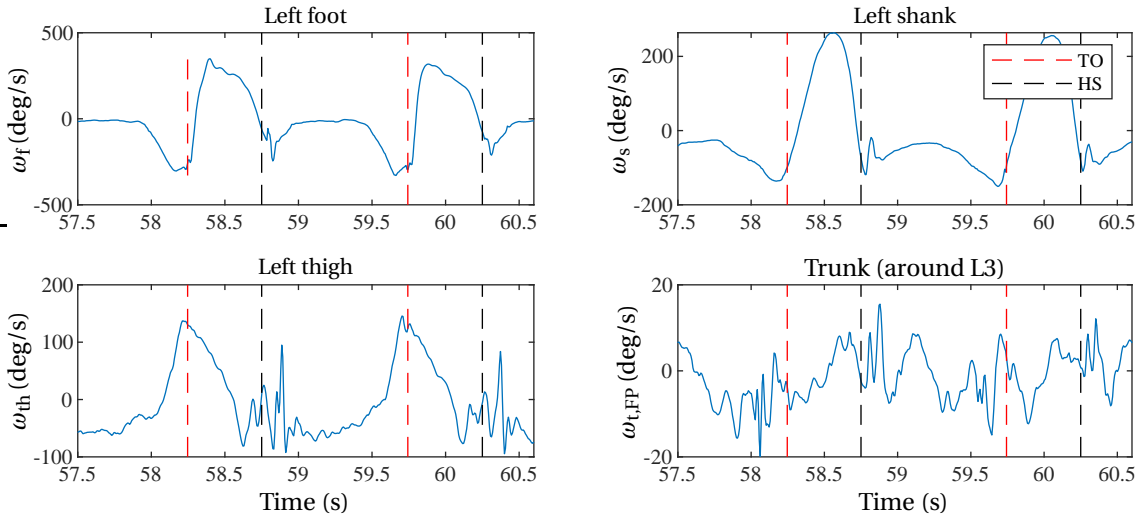


Figure 2.4: Visualisation of angular velocity of the trunk and the lower limbs together with the temporal location of the (ground truth) gait events during normal walking with medium cadence. Note that for the trunk, the angular velocity shown here is in the frontal plane ($\omega_{t,FP}$; the swaying motion of the trunk in lateral direction could only be noticed in this plane) while sagittal plane angular velocity is shown for the other three segments (foot, shank and trunk). For a similar visualisation of the norm of the accelerometer signal of each segment, see Figure B.1.

For the shank, a table identical to the one presented in Table 2.3 for the foot was observed, with the only noticeable difference being in the prominence of PSw peak and MSw peak compared to the foot, as discussed above.

From trunk kinematics, the only prominent feature that could be identified was the sharp, distinguishable peak around HS, although the onset of which was observed to be slightly delayed as noted in Figure 2.5. Since there is a possibility that the trunk IMU may also be worn at the abdomen, we compared the signals from an IMU placed at the trunk to that placed at the abdomen. It was observed in the time domain that the abdominal signal was relatively more oscillatory than that of the trunk. From the frequency spectrum plot shown in Figure 2.6, it can be observed that frequencies in the range 5-25 Hz are more prominent, likely contributed by the soft tissues at abdomen as opposed to relatively rigid support at the trunk (around L3).

	S1	S2	S3	S4	S5	S6	S7	S8	S9
PSw peak	✓	✓	✓	✓	✓	✓	✓	✓	✓
MSw peak	✓	✓	✓	✓	split	✓	✓	✓	✓
LR peak	✓	✓	✓	x	weak	weak	✓	✓	✓
MSt, NoA	✓	✓	✓	✓	✓	✓	✓	✓	✓
MSt, AV	✓	✓	✓	disturbed	✓	disturbed	✓	✓	✓
TO (HFC) NoA	✓	✓	✓	✓	✓	✓	✓	✓	✓
TO (HFC) AV	✓	✓	✓	✓	✓	✓	✓	✓	✓
TO (ZC) AV	✓	✓	✓	✓	✓	✓	✓	✓	✓
HS (HFC) NoA	✓	✓	✓	x	scattered	✓	✓	✓	✓
HS (HFC) AV	✓	✓	✓	x	scattered	✓	✓	✓	✓
HS (ZC) AV	✓	✓	✓	x	weak	✓	✓	✓	✓

Table 2.3: Summary table: Investigating the prominent features in foot IMU signals to identify gait events. TO and HS are investigated for both Zero Crossings (ZC) and High Frequency Contents (HFC) in both the Angular Velocity (AV) signal and the Norm of the Accelerometer (NoA) signal. Features that were not relevant to a particular scenario are marked with a cross while tick mark implies that the feature is present. Features that were not distinguishable at least in normal walking condition at varying cadence (i.e., S1, S2 and S3) were not considered in this study.

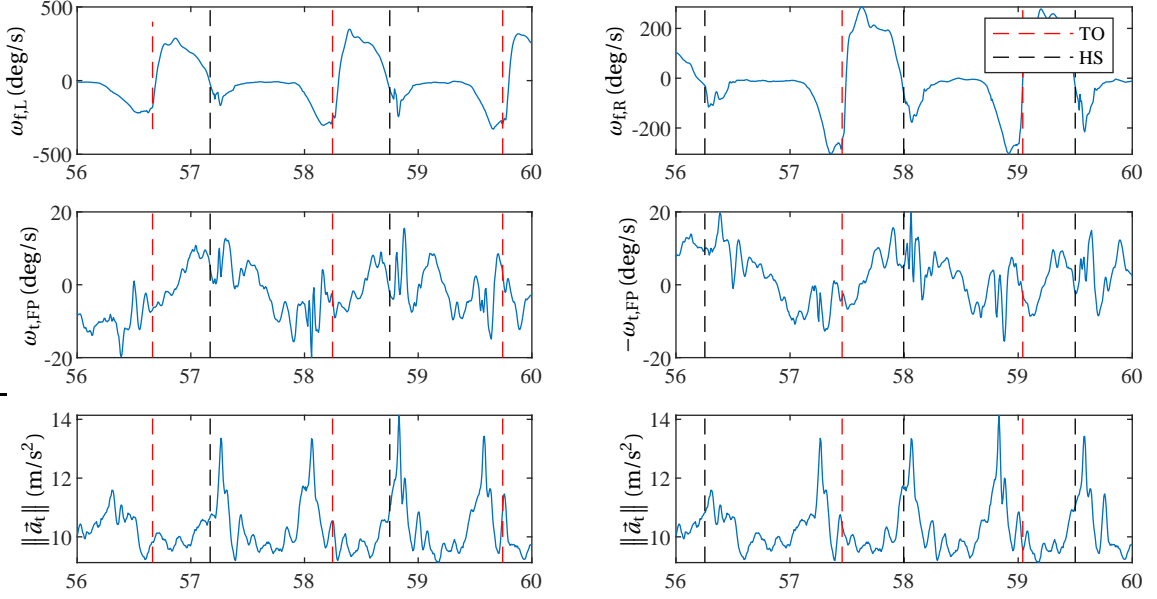


Figure 2.5: Trunk kinematics feature selection: Angular velocity of left ($\omega_{f,L}$) and right foot ($\omega_{f,R}$) are shown in the upper plots for reference. Compare it together with the gait events to the plots below showing the trunk angular velocity in frontal plane (middle left and right plots are the same, except that one is the negative of the other and is shown separately for better comparison with the corresponding left and right side gait events) and the norm of the accelerometer signal (same in lower left and right plots). It can be observed that the peaks in the norm of the accelerometer signal of the trunk ($\|\tilde{a}_t\|$) were more distinguishable and sharp than for the peaks in angular velocity ($\omega_{t,FP}$).

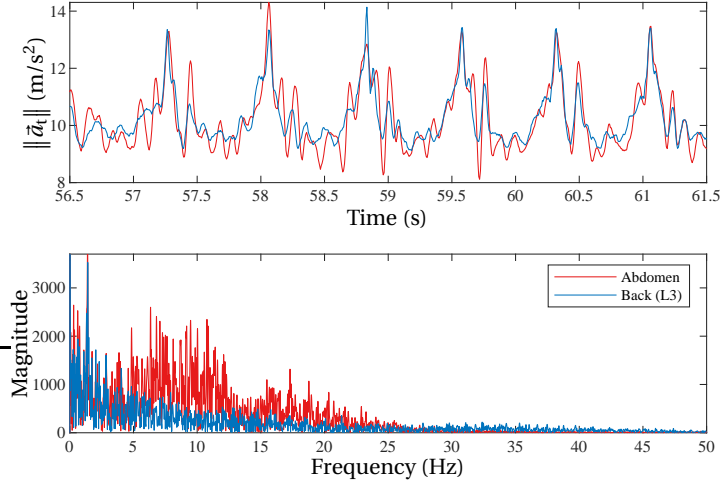


Figure 2.6: The upper plot compares the norm of the accelerometer signal from IMU mounted at the trunk (near L3) to that at the abdomen. Lower plot shows the frequency spectrum analysis of both the signals. The influence of soft tissues in the abdomen can clearly be seen through the difference in prominence of frequency components in the range 5Hz to 25Hz.

2.2.2. METHOD DESIGN: HEURISTICS-BASED GAIT DETECTION

It can be observed from Table 2.3 that for TO detection, zero crossing after PSw as well as high frequency content appears to be equally good candidates. Similarly, it can also be observed that HS can be identified from zero crossing after PSw as well as high frequency content with the exception that it does not perform well during foot drag. Further, as we discussed before, HS can also be detected from the trunk peak in the norm of the accelerometer signal.

It can also be observed from Table 2.3 that PSw peak is easily distinguishable in all the 9 scenarios which is also true of MSw peak except during foot drag where the peak is split. Since these two features are very robust and show up just before TO and HS events respectively, they were chosen to be used as heuristics to detect the events more robustly. Note that since peak detection is only used as heuristics, detecting them

in quasi-real-time is sufficient (as long as it is detected before the actual events), thereby circumventing the inherent problem of delay associated with using peak detection itself as a real-time gait detection method (as discussed in Chapter 1), but without giving up the advantage these peaks offers as robust features. Note that in this study, we used the `findpeaks` method in MATLAB to detect the peaks, the settings of which are reported in Appendix C for reproducibility.

Further, it can also be observed from Table 2.3 that for the stance phase detection, the norm of the accelerometer signal is better than the angular velocity signal. Although the angular velocity of the foot during stance phase for a healthy gait should be close to zero, this is not the case with SCI patients. As mentioned before, it was observed that when one leg is performing exaggerated hip flexion, the corresponding angular velocity of the contralateral leg during stance phase deviates significantly from zero as shown in Figure 2.1. This was also observed to be the case when the patient is using a walker (see Figure B.3). This artifact was much less prominent in the case of the norm of the accelerometer signal and hence it was the preferred choice for stance phase detection.

The state flow diagram in Figure 2.7 illustrates the proposed method graphically. The red path is to be traced when the method is performing as intended, (when there is no mis-detection), as is explained below:

1. A zero crossing or high frequency content is accepted as the TO event as soon as it is encountered, provided it follows a PSw heuristic in the sagittal plane angular velocity profile (of foot or shank) and does not overlap with stance phase.
2. A zero crossing, high frequency content or peak in the trunk norm of accelerometer signal is accepted as the HS event as soon as it is encountered, provided it follows a MSw heuristic in the sagittal plane angular velocity profile (of foot or shank) and does not overlap with the stance phase.
3. The stance phase interval is continuously updated based on the duration in which the norm of the accelerometer signal falls within a set range (see T8 in Figure 2.7). The range is set to be $(\|\vec{a}_{st}\| \pm 0.1g)$ where \vec{a}_{st} is the static acceleration reported by the IMU and g is the acceleration due to gravity. Note that although the static acceleration output of the IMU should ideally be the acceleration due to gravity, in practice, it was noticed that due to sensor error, the value was off by 5-10%. Thus, the static acceleration of each sensor used was noted at the beginning of the experiment and set as $\|\vec{a}_{st}\|$.

However, for the method to be robust to SCI gait and to recover in the event of a mis-detection, it needs to be tolerant to situations where the leg movement does not go as expected or when a step fails to take-off. Thus, fall back options are necessary, which are shown by the dotted lines (T1 to T7) in Figure 2.7. For instance, the importance of T7 (repeatedly detecting PSw before TO) can be understood from Figure 3.9 where back-to-back PSws were identified (where only the latter was actually a PSw, while the former was a spike in signal during stance phase) before identifying the corresponding TO correctly.

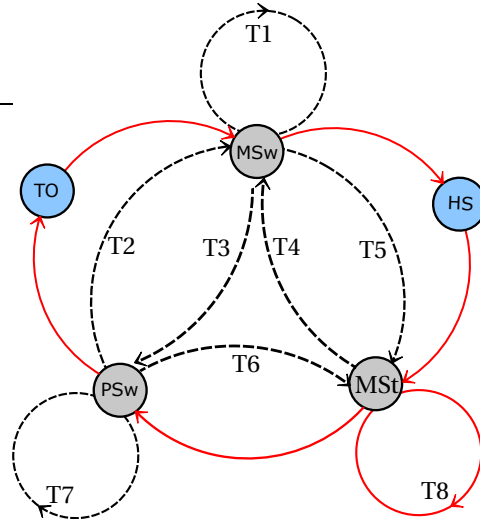


Figure 2.7: State flow diagram representing the proposed method. The red path is to be traced when the method is performing as intended. The dotted lines (T1-T7) represents fall back options to ensure that the method recovers in the event of a mis-detection.

2.2.3. METHOD TESTING

All the three versions of the proposed method were first tested using the mimicked dataset, with IMU signals from foot, shank and/or trunk, as illustrated in Table 2.4. The zero crossing-based method was tested, first based on foot IMU signals alone (ZC_F) where TO and HS were identified from zero crossings following PSw and MSw peaks. The same procedure was carried out with shank IMU signals alone (ZC_S). Finally, a third possibility was tested (ZC_SF) wherein the shank norm of accelerometer signal was replaced with the foot norm of accelerometer signal while everything else remained the same. This was motivated by the fact that the shank norm of accelerometer signal and the angular velocity in sagittal plane are not completely zero even during the stance phase, as opposed to the foot. This could also be seen as equivalent to stance phase detection coming from the foot-worn insole while the IMU is still at the shank. The same process was also repeated for the method based on high frequency content. Further, the trunk kinematics-based method was tested, first based on foot and trunk IMU signals (TK_F) where the trunk norm of accelerometer signal was used for HS event detection while MSw peak of foot angular velocity was used as the heuristics. Since no feature in the trunk signal could be identified for TO detection, (for symmetry and to be sure, not detecting TO was not impacting the detection performance of HS,) TO was detected using the same procedure as that of zero crossing-based method (ZC_F). The testing was also carried out using shank and trunk IMU signals (TK_S).

Unique Identifier	TO		HS		Stance
	Heuristics	Event detection	Heuristics	Event detection	
TK_F		F_AV	F_AV	T_NoA	F_NoA
TK_S		S_AV	S_AV	T_NoA	S_NoA
ZC_F		F_AV	F_AV		F_NoA
ZC_S		S_AV	S_AV		S_NoA
ZC_SF		S_AV	S_AV		F_NoA
HFC_F		F_AV	F_AV		F_NoA
HFC_S		S_AV	S_AV		S_NoA
HFC_SF		S_AV	S_AV		F_NoA

Table 2.4: Each version of the proposed method was tested with IMU signals from foot, shank and/or thigh, the combinations of which are shown in the table. For concise representation, the following abbreviations are used: AV - Angular Velocity, NoA - Norm of Accelerometer signal, F - Foot, S - Shank, SF - Shank-and-Foot, TK - Trunk Kinematics, ZC - Zero Crossing, HFC - High Frequency Content. Thus, for instance, HFC_SF is to be interpreted as High Frequency Content-based method tested with signals from the shank and the foot IMU as mentioned in last row of the table.

The method, in general, was tested in a simulated real-time environment. That is, the sensor data was played in real-time using the sensor time-stamp, as if the signal was being live-streamed, independent of the state of the algorithm. If the algorithm is not able to process the incoming data at the sensor sampling rate, (for instance, due to computational delay) the algorithm will have to either skip the unprocessed samples in favour of the latest ones or process multiple samples simultaneously and is not allowed to report events retroactively as it would not be useful in a real-time environment. An exception to this was the version involving wavelet transform, where such a set up was observed to be infeasible due to the computational delay of wavelet transform. Thus, the results presented for HFC-based method does not take into account, the computational delay, while the other two methods (zero-crossing based and trunk kinematics based) indeed take it into account.

Furthermore, the proposed methods were also tested on patient datasets D1 and D3 introduced earlier in Section 2.1.1. Since neither of the two datasets involved the trunk kinematics data, testing the method based on trunk kinematics was not possible. The results are presented in next chapter.

2.3. IMU EMULATION

As discussed in the previous chapter, to convert the current motion capture datasets (collected based on a minimal set of utmost 2 markers per segment) into corresponding IMU datasets, an IMU emulation method needs to be developed and this will be discussed in this section. We know that at least three points are required to fully define a plane and thus three markers per segment are necessary to fully define the 3D orientation of a body. However, the motion capture datasets generated from STIMO clinical study follow a marker placement protocol based on a modified version of the Vicon® Plug-in-Gait marker placement protocol, wherein four markers are placed on either side of lower body, one on the lateral epicondyle for the knee,

one on the lateral malleolus for the ankle, one on the second metatarsal head for the toe and finally, one on the grand trochanter for the hip (easy to feel by palpation). The approximate location of hip, knee and ankle markers are illustrated in Figure 2.9. These minimal set of markers translate into only up to 2 markers per body segment, making our problem of 3D IMU emulation non-trivial.

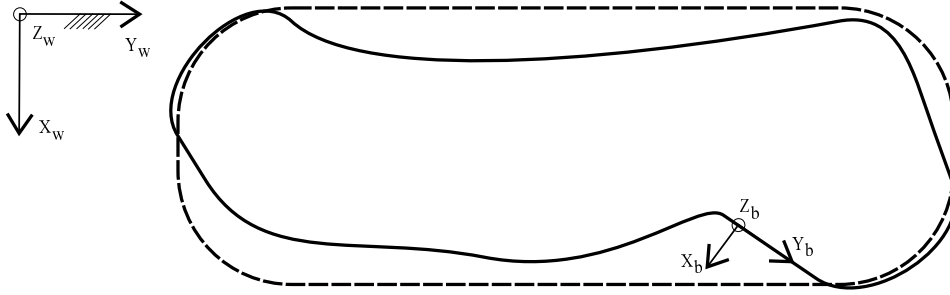


Figure 2.8: An illustration of the top view of the path covered by a patient in a typical session during the STIMO study. Here, frame w represents the world frame (motion capture) which is an inertial frame of reference while frame b represents any body-fixed coordinate system (for instance, attached to the thigh). Note that the Z_w and Z_b axis need not be aligned.

The irregular path traversed by the patients, as illustrated in Figure 2.8 means that the sagittal plane of the patient will not necessarily be aligned to any plane in the world frame at all times, but will rather have its components changing depending on the movement of the subject. Thus, although the direct evaluation of the 2D angular velocity and linear acceleration of the subject in the world frame from motion capture data is trivial, evaluating the same (from motion capture data) with respect to the body-fixed frame with minimal set of markers in this situation is non-trivial. We propose to solve this by introducing lower-body kinematic constraints into the 3D rotation matrix by adding the knee axis as the additional constraint.

2.3.1. ROTATION MATRIX AND AXIS STABILITY

Consider one body segment, let's say the thigh. Imagine two frames of reference; the world frame (frame w) which is static with respect to the motion capture system and the body-fixed frame (frame b) which is attached to the thigh. The orientation of the world frame is chosen to be consistent with the motion capture dataset while the orientation of the body-fixed frame is aligned as follows:

1. The Z-axis of the thigh was defined along the longitudinal axis joining the markers at hip and knee (P_1 and P_2), and calculated as the unit vector given by:

$$\hat{Z}_t = \frac{O\vec{P}_1 - O\vec{P}_2}{|O\vec{P}_1 - O\vec{P}_2|}, \quad (2.1)$$

where $O\vec{P}_1$ and $O\vec{P}_2$ are position vectors to hip and knee marker positions (P_1 and P_2) respectively from the origin of the world frame (motion capture system) as shown in Figure 2.9. In a similar fashion, the shank longitudinal axis can be obtained by replacing $O\vec{P}_1$ and $O\vec{P}_2$ with $O\vec{P}_2$ and $O\vec{P}_3$ respectively in the above equation, where $O\vec{P}_3$ is the position vector to the ankle marker (P_3).

2. The X-axis of the thigh was chosen as the mean of hip and knee joint axes. The hip axis was evaluated as the vector between left and right hip markers while the immediate choice for evaluating knee axis should be the unit vector along the plane normal to thigh and shank longitudinal axis, making use of the constraint that knee can approximately be modelled as a hinge joint. The knee axis could thus be evaluated as:

$$\hat{k} = \frac{\hat{Z}_t \times \hat{Z}_s}{|\hat{Z}_t \times \hat{Z}_s|} = \frac{\hat{Z}_t \times \hat{Z}_s}{|\hat{Z}_t| |\hat{Z}_s| \sin(\theta)}, \quad (2.2)$$

where θ is the angle between the Z-axis of the thigh (\hat{Z}_t) and that of the shank (\hat{Z}_s). However, normalising the vector means that it could become singular when the knee joint is fully extended and θ tend to zero or even switch the direction of axis to the other side as illustrated in Figure 2.10. This could be

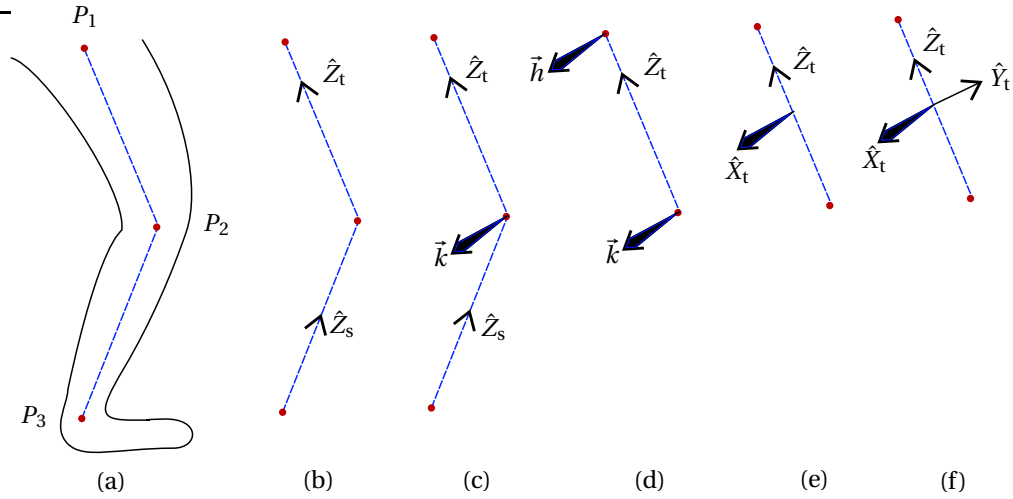


Figure 2.9: (a) Marker positions P_1 , P_2 and P_3 are shown at hip, knee and ankle joints respectively. (b) Longitudinal axis of segment is chosen as corresponding Z-axis where sub-scripts t and s correspond to thigh and shank respectively. (c) Knee axis is determined as the cross product of Z_t and Z_s (d) Hip axis is evaluated as the vector between the left and right hip marker positions (e) Thigh axis normal to sagittal plane (X_t) is evaluated by taking the weighted average of hip and knee axis as described in 2.3 (f) Y-axis is determined following the right-hand rule. Note that the solid (thick) arrow points out of the plane of the paper.

remedied by not normalizing the knee vector, but it means that we cannot directly take the mean of hip and knee axis any more to evaluate the thigh X-axis. Instead, we calculated the thigh axis as weighted average of knee and hip axis:

$$\hat{X}_t = \frac{\hat{h} + \vec{k} |\vec{k}|}{|\hat{h} + \vec{k} |\vec{k}||}, \quad (2.3)$$

where \hat{h} is the unit vector along the hip axis, evaluated as

$$\hat{h} = \frac{\vec{OP}_{1L} - \vec{OP}_{1R}}{|\vec{OP}_{1L} - \vec{OP}_{1R}|}, \quad (2.4)$$

where $\vec{OP}_{1,L}$ is the left hip marker and $\vec{OP}_{1,R}$ is the right hip marker.

3. The Y-axis of the thigh then follows as the normal to both X and Z-axis (right-hand rule).

The rotation matrix of the body-fixed frame with respect to world frame can thus be written as

$$\mathbf{R}_b^w = \left[\left(\hat{X}_t \right)^T \left(\hat{Z}_t \times \hat{X}_t \right)^T \left(\hat{Z}_t \right)^T \right]. \quad (2.5)$$

Before proceeding further, the additional constraint introduced in the rotation matrix (together with the weighted average proposition) to ensure the axis stability was validated. This result is presented in Section 3.2.1 and illustrated in Figure 3.15.

2.3.2. ANGULAR VELOCITY AND LINEAR ACCELERATION IN BODY-FIXED FRAME

For IMU emulation, it is necessary to transform the known orientation and position in the world frame (from motion capture data) into corresponding angular velocity and linear acceleration in the body-fixed frame (the emulated IMU data). Thus, in this section, our goal is to obtain the equation for angular velocity in the body-fixed frame, given the rotation matrix described in the previous section and the equation for linear acceleration in the body-fixed frame, given the rotation matrix and linear acceleration in world frame.

Since rotation and translation of a rigid body can be treated separately, first we will obtain the equation for angular velocity in the body-fixed frame, given the rotation matrix. Consider two frames, a non-inertial frame

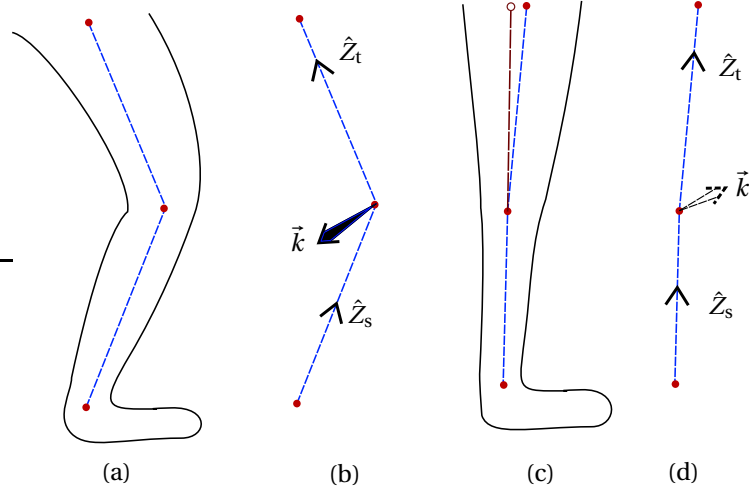


Figure 2.10: (a) Knee joint in a partially flexed state. (b) Resulting knee axis points out of the plane of the paper. (c) Knee in fully extended state. Depending on the position of markers, it is likely that they subtend a reflex angle (more than 180 degree). (d) Resulting knee axis points into the plane of the paper (Note that the solid arrow points out of the plane of the paper while the dotted line arrow points into the plane of the paper).

of reference, say frame b (body-fixed frame) with origin at O' and an inertial frame of reference, say frame w (world frame) with origin at O as shown in Figure 2.11. Since here we are interested in rotation, assume that both the origins O and O' coincide, thus allowing only rotation (and not translation) between them. Consider a point H attached to the body-fixed frame. The position vector of point H expressed in world frame ($\vec{O}H_w$) can be expressed as

$$\vec{O}H_w = \mathbf{R}_b^w \vec{O}H_b, \quad (2.6)$$

where $\vec{O}H_b$ is the position vector of point H expressed in the body-fixed frame and \mathbf{R}_b^w is the rotation matrix of the body-fixed frame expressed in the world frame (to be evaluated as described in the previous section, using Equation 2.5). Differentiating the above equation with respect to time gives:

$$\dot{\vec{O}H}_w = \dot{\mathbf{R}}_b^w \vec{O}H_b + \mathbf{R}_b^w \dot{\vec{O}H}_b. \quad (2.7)$$

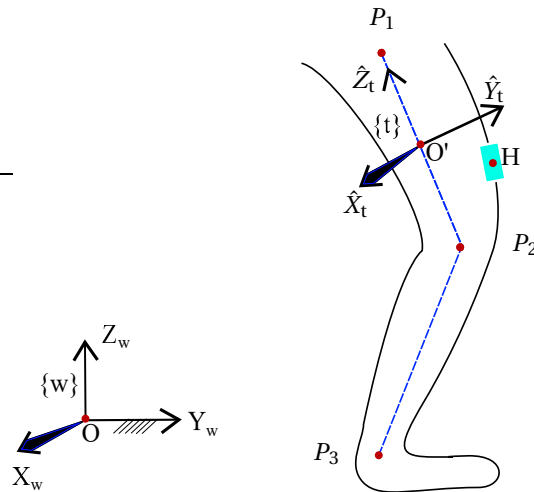


Figure 2.11: The world frame is represented by w with origin at O . A typical position of IMU is shown in cyan where H represents the centre of the IMU. Note that the body fixed frame (with origin O') illustrated in the figure corresponds to the thigh and hence was represented by more specific t (' t ' for thigh) instead of b (' b ' for the body-fixed frame). The vector $O'H$ is unknown and the position shown in figure is arbitrary.

Since point H is attached to the body-fixed frame b , $\dot{\vec{O}H}_b = 0$ (note that this is analogous to our situa-

tion where each IMU is fixed with respect to corresponding body segment). We can thus simplify the above equation as

$$\dot{O}H_w = \dot{\mathbf{R}}_b^w O\vec{H}_b. \quad (2.8)$$

Equation 2.6 can be re-written as $O\vec{H}_b = (\mathbf{R}_b^w)^{-1} O\vec{H}_w = (\mathbf{R}_b^w)^T O\vec{H}_w$ (since \mathbf{R} is orthogonal), which can then be substituted into equation 2.8, resulting in

$$\dot{O}H_w = \dot{\mathbf{R}}_b^w (\mathbf{R}_b^w)^T O\vec{H}_w. \quad (2.9)$$

Clearly, equation 2.9 is similar to the basic kinematic equation (the transport theorem) for pure rotation, given by

$$\dot{O}H_w = \tilde{\omega}_w O\vec{H}_w, \quad (2.10)$$

from which it can be inferred that the (instantaneous) angular velocity in world frame ($\tilde{\omega}_w$) can be evaluated as

$$\tilde{\omega}_w = \dot{\mathbf{R}}_b^w (\mathbf{R}_b^w)^T. \quad (2.11)$$

Note that $\tilde{\omega}_w$ is expressed in the matrix-vector representation. By using the orthogonality property of rotation matrix, it can be shown that $\tilde{\omega}_w$ is a skew-symmetric matrix, the components of which are given by

$$\tilde{\omega}_w = \begin{bmatrix} 0 & -\omega_z & \omega_y \\ \omega_z & 0 & -\omega_x \\ -\omega_y & \omega_x & 0 \end{bmatrix}, \quad (2.12)$$

where the three independent elements of this matrix correspond to the three angular velocity components ω_x , ω_y and ω_z in the world frame. The corresponding vector form follows as $\tilde{\omega}_w = [\omega_x \ \omega_y \ \omega_z]^T$. The angular velocity in the world frame (expressed in vector form, $\tilde{\omega}_w$) can be transformed to angular velocity in the body-fixed frame (expressed in vector form, $\tilde{\omega}_b$) using the coordinate transformation equation $\tilde{\omega}_b = \mathbf{R}_w^b \tilde{\omega}_w$. The equivalent transformation corresponding to the earlier mentioned matrix-vector representation follows from tensor calculus, giving

$$\tilde{\omega}_b = \mathbf{R}_w^b \tilde{\omega}_w (\mathbf{R}_w^b)^T. \quad (2.13)$$

Since, our goal is to obtain an equation for angular velocity exclusively in terms of the rotation matrix, we substitute equation 2.11 in equation 2.13, resulting in angular velocity expressed in the body-fixed frame as

$$\begin{aligned} \tilde{\omega}_b &= \mathbf{R}_w^b \dot{\mathbf{R}}_b^w (\mathbf{R}_b^w)^T (\mathbf{R}_w^b)^T \\ &= \mathbf{R}_w^b \dot{\mathbf{R}}_b^w \mathbf{I} \\ &= (\mathbf{R}_b^w)^T \dot{\mathbf{R}}_b^w. \end{aligned} \quad (2.14)$$

This equation is used to evaluate the emulated angular velocity in the body-fixed frame (similar to what an IMU attached to the same frame would measure) when the rotation matrix is known. Note that the above derivation is adapted in parts from [40] and [41].

Linear acceleration of the segment in the world frame can be evaluated by double differentiating the position vector from origin to the segment. A two-step finite central difference method was used for numerical differentiation. Although filtering could be used to reduce the error due to numerical differentiation, it was not used in the current study as optimum filter design was outside the scope of the current project. Note that the acceleration at each point in the segment will be different and hence it is necessary to choose that point where the IMU is placed. However, since the position of IMU is not known to us, we will assume that it is placed approximately in the middle of the body segment, between the two markers of the segment. That is, the point H (representing the center of IMU) coincides with origin of body fixed frame O' (located at the mid-point between the two markers). Hence, the position vector to the segment (\vec{x}_w) is evaluated as that vector pointing to mid-point connecting the two markers, given by

$$\vec{x}_w = \frac{\vec{OP}_1 + \vec{OP}_2}{2}. \quad (2.15)$$

Linear velocity ($\dot{\vec{x}}_w$) and subsequently linear acceleration ($\ddot{\vec{x}}_w$) in the world frame are obtained through numerical differentiation with finite central difference method as shown below:

$$\dot{\vec{x}}_w = \frac{\vec{x}_w(t + \Delta t) - \vec{x}_w(t - \Delta t)}{2\Delta t}, \text{ and} \quad (2.16)$$

$$\ddot{\vec{x}}_w = \frac{\dot{\vec{x}}_w(t + \Delta t) - \dot{\vec{x}}_w(t - \Delta t)}{2\Delta t}. \quad (2.17)$$

Subsequently, acceleration due to gravity is added to the vertical component (Z-axis) of linear acceleration in the world frame, to be able to compare it with acceleration estimated by IMU (since the accelerometer signal typically includes acceleration due to gravity), given by

$$(\vec{a}_w)_z = (\ddot{\vec{x}}_w)_z + g. \quad (2.18)$$

This acceleration in the world frame (say \vec{a}_w) can then be transformed to acceleration in the body-fixed frame (say \vec{a}_b) by pre-multiplying with the rotation matrix as $\vec{a}_b = \mathbf{R}_w^b \vec{a}_w$.

With no necessity to be real-time, the testing environment for IMU emulation was simpler than the one described in Section 2.2.3 for real-time gait detection. The method was tested on the patient dataset D1 where both IMU data and motion capture data were available. The motion capture data was used as input to IMU emulation whereas the actual IMU data was used for validating the IMU emulation result. As already discussed in Section 2.1.1, the dataset used had markers placed at hip, knee and ankle of both legs and IMUs placed at thigh and shank.

2.3.3. TIME SYNCHRONIZATION

The goal here is to identify the delay in number of samples between motion capture data and IMU data when both are collected from independent sources of sensors without being time-synchronised implicitly. First, a feasibility study was carried out wherein an IMU with a passive marker on its top was shaken for few a seconds. The idea is to compare the data from both sensors, after bringing them to the same variable, to assess the delay between them. The variable chosen for this was the norm of acceleration which was obtained by double differentiating the marker position (see Figure B.4) using finite central difference method and gravity was added to the vertical component, and then compared the result to the norm of the accelerometer signal from IMU. It can be noted from the upper plot in Figure 2.12 that the signal evaluated from both the sources are identical, except a lag in actual IMU signal with slightly higher amplitude compared to the emulated IMU signal from motion capture data. The lag was then estimated using cross-correlation which compares both signals throughout their duration by shifting one signal with respect to the other in time domain and evaluating the correlation at each instance. The correlation should be the highest when the signals overlap the best, from which the delay in number of samples can be estimated. Once the delay in number of frames between the two sources of data is identified, the signals can be explicitly time-synchronized.

It can be noted from this feasibility study that if signals from both the sensors are brought to the same variable, the cross correlation could be used to analyse the delay in the number of samples between them effectively. This procedure was extended together with IMU emulation to time-synchronize patient datasets from STIMO. First, the motion capture dataset was transformed to emulated IMU data and then one of the channels from the emulated IMU data was compared to corresponding signal from actual IMU using cross correlation to identify the delay. The method was tested on patient dataset D2. As already discussed in Section 2.1.1, this motion capture dataset and corresponding IMU dataset were not implicitly time-synchronized since they were both collected using independent sources of sensors. Once the signals were time-synchronized, the motion capture dataset, which was not useful before, could now be used to label ground truth events for the synchronized IMU data. The test results are presented in the next chapter.

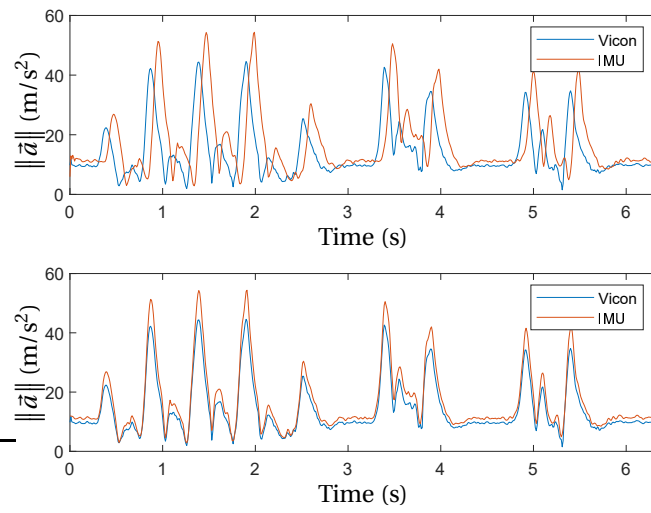


Figure 2.12: The norm of the accelerometer signal emulated from motion capture data is compared to the norm of the accelerometer signal from IMU; upper figure before compensating for the delay and lower figure after compensating for the delay.

3

RESULTS

This chapter is organized as follows: Section 3.1 presents the results of gait detection methods tested on the mimicked datasets and the patient datasets while Section 3.2 presents the result of IMU emulation method and time-synchronisation introduced in the previous chapter.

3.1. GAIT DETECTION

3.1.1. ZERO CROSSING WITH PEAK HEURISTICS

The result of the heuristics-based gait detection method using zero crossing, proposed in the previous chapter and tested using the mimicked dataset, is presented here. In Figure 3.1, the detection performance is reported in terms of F1 score. Note that the F1 score was chosen because it combines the essence of precision and recall in one variable (thereby making comparison across results easier) by taking the harmonic mean of both. It can be noticed that when the foot IMU signal alone is used, the performance of HS detection drops to a very low F1 score of around 0.27 when the foot drag is involved. Although the low performance is reflected only in the right HS, it is to be recalled here that this is because the foot drag was mimicked only using the right leg and hence the better detection performance for the left HS should be discounted. It can be noticed that the performance of the TO detection reduced during the foot drag (0.59 for the left TO and 0.57 for the right TO) and gait asymmetry (0.54 left TO and 0.32 for right TO) when shank IMU signal is used. It can also be noticed that when shank and foot IMU signals are used together, the detection performance is much higher with the lowest F1 score being 0.91 and 0.82 for the left and the right TO respectively while 0.93 and 0.89 for the left and the right HS respectively.

In Figure 3.2, the corresponding latencies are reported as compact box plots showing the variation within and across scenarios. The line joining the median latencies corresponding to each scenario highlights the trend. It can be noticed that the latency during HS detection is almost the same irrespective of which IMU signal was used, with average of median latencies across scenarios to be around less than 10 ms. However, for TO detection, it can be noticed that the latency is low only when foot IMU signal alone is used with an average of median latencies across scenarios at 30 ms and 27 ms for left and right respectively while in the other two cases at around 66 ms and 63 ms for left and right respectively.

3.1.2. HIGH FREQUENCY CONTENT WITH PEAK HEURISTICS

The result of the heuristics-based gait detection method using HFC, proposed in previous chapter and tested using the mimicked dataset, is presented here. In Figure 3.3, the detection performance is reported in terms of the F1 score. It can be noticed that the method based on the foot IMU signal fails completely during HS detection with an F1 score of zero when there is foot drag, while reporting noticeably higher scores in other scenarios. It can also be noticed that when the shank IMU signal is used, the performance of TO detection reduced during low cadence (0.17 for right TO and 0.53 for left TO), foot drag (0.53 for left TO and 0.48 for right TO) and gait asymmetry (0.25 left TO and 0.29 for right TO). Further, it can also be noticed that when shank and foot IMU signals are used together, the detection performance improves, but still with the lowest F1 score being 0.50 and 0.59 for left and right TO respectively while it was 0.70 and 0.86 for left and right HS respectively.

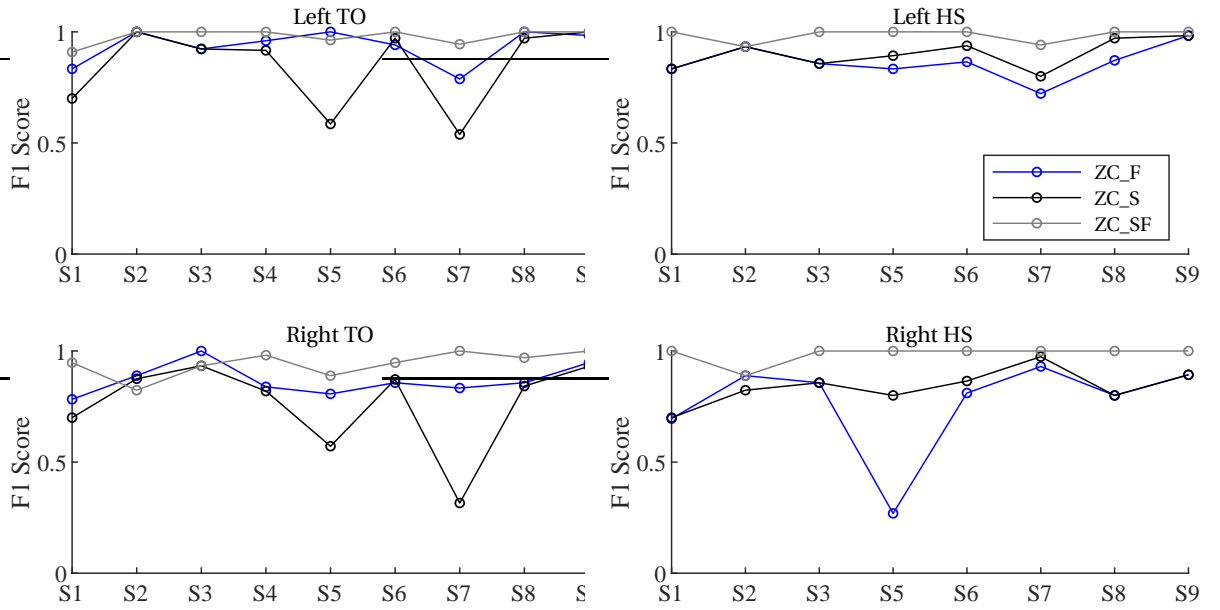


Figure 3.1: Gait detection using zero crossing with peak heuristics: Figure shows the performance (F1 score) of the method when tested using IMU signals from foot (ZC_F), shank (ZC_S) and shank + foot (ZC_SF) against all the walking scenarios discussed earlier.

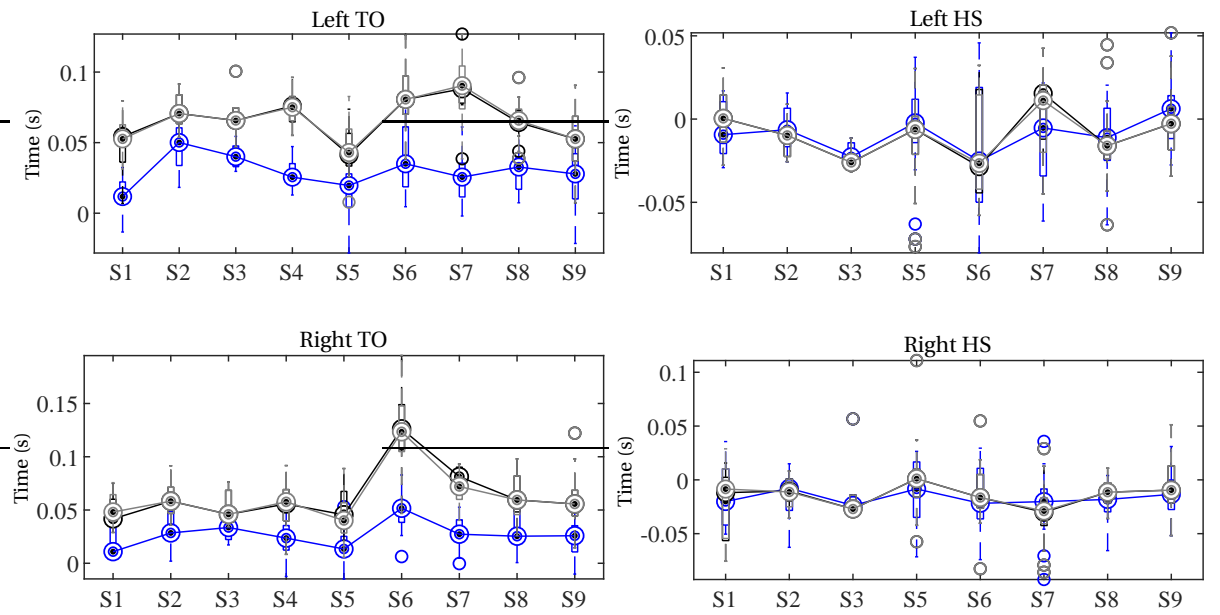


Figure 3.2: Gait detection using zero crossing with peak heuristics: Figure shows latency in detection when tested using IMU signals from foot (ZC_F), shank (ZC_S) and shank + foot (ZC_SF) against all the walking scenarios discussed earlier. Note that the central mark indicates the median, the bottom and top edges of the box indicate the 25th and 75th percentiles respectively while the whiskers extend to the most extreme data points not considered outliers, and the outliers are plotted individually using the 'o' symbol.

In Figure 3.4, the corresponding latencies are reported as compact box plots. It can be noticed that the latency is relatively high for HS detection, with the average of median latencies across scenarios around 50 ms when the foot IMU signal alone is used while at around 70 ms in the other two cases. For TO detection, the latency is lower when the foot IMU signal alone is used with the average of median latencies across scenarios around 31 ms while in the other two cases at around 82 ms and 66 ms respectively for the left and the right TO with latency during low cadence for the left foot TO detection going as high as 150 ms. It is worth noting here that this latency is without considering the computational delay contributed by wavelet transform, as mentioned earlier in Chapter 2.

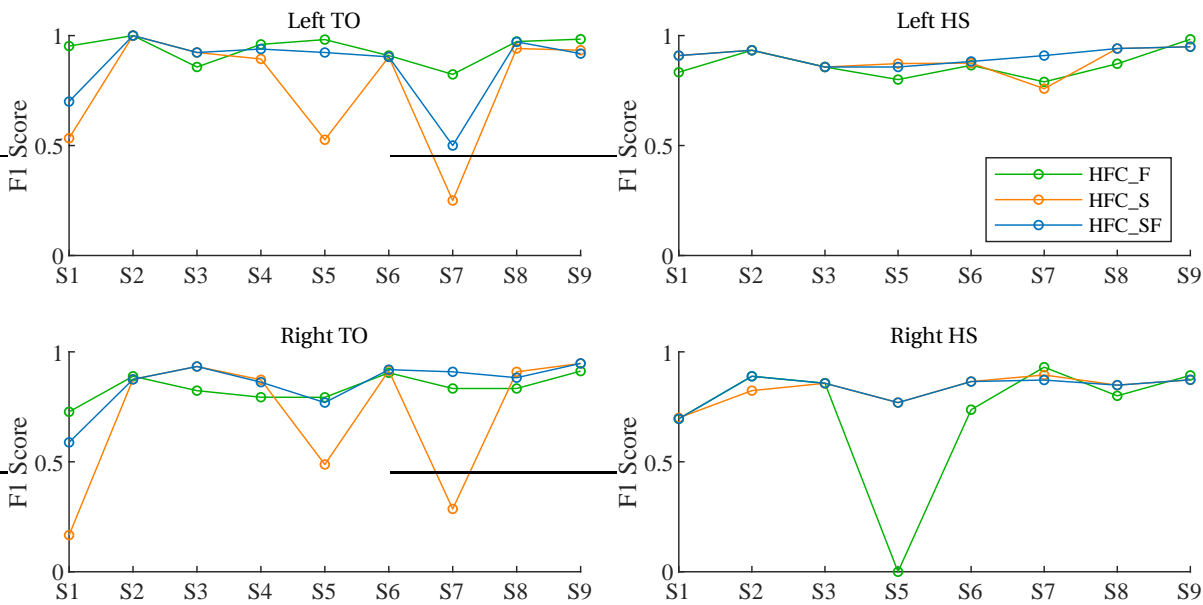


Figure 3.3: Gait detection using High frequency content with peak heuristics: Figure shows the performance (F1 score) of the method when tested using IMU signals from foot (HFC_F), shank (HFC_S) and shank + foot (HFC_SF) against all the walking scenarios discussed earlier.

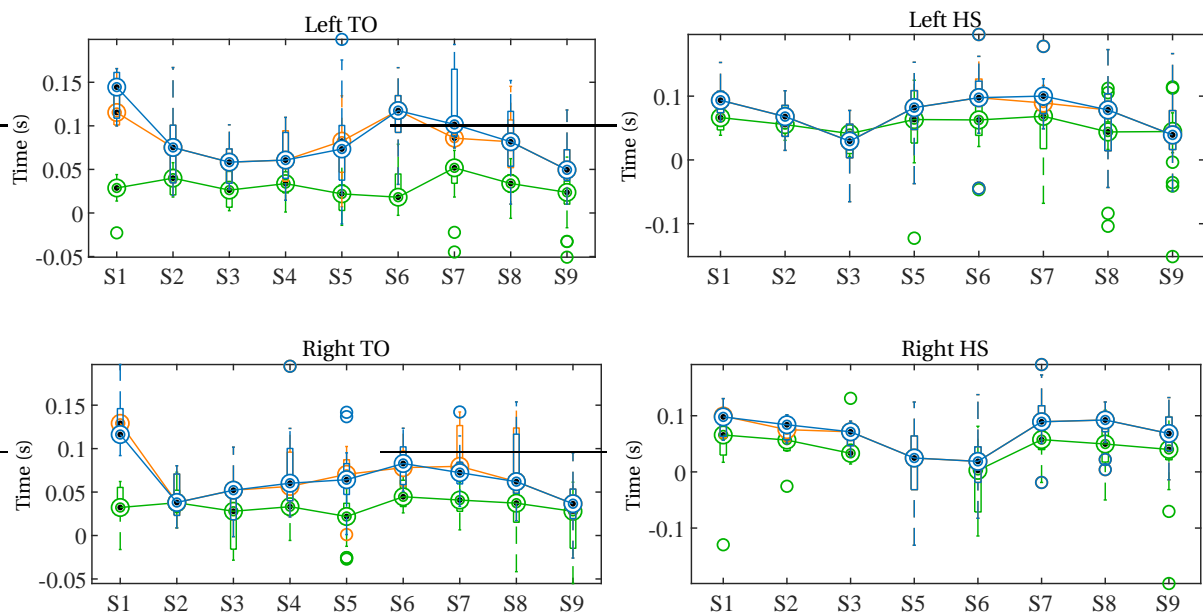


Figure 3.4: Gait detection using High frequency content with peak heuristics: Figure shows latency in detection when tested using IMU signals from foot (HFC_F), shank (HFC_S) and shank + foot (HFC_SF) against all the walking scenarios discussed earlier. Conventions described in Figure 3.2 applies.

3.1.3. TRUNK KINEMATICS WITH PEAK HEURISTICS

The result of the heuristics-based gait detection method using trunk kinematics, proposed in the previous chapter and tested using the mimicked dataset, is presented here. In Figure 3.5, the detection performance is reported in terms of the F1 score. It can be noticed from Figure 3.5 that unlike in the previous two cases (zero crossing based and high frequency content based methods), the performance of HS detection increases with trunk kinematics, particularly during foot drag. F1 scores of 0.84 for right HS and 0.88 for left HS can be noticed when using trunk and foot IMU signals together. Replacing foot with shank improves the score further to 0.95 and 1 respectively for right and left HS. This is a remarkable improvement from the previous two methods where the lowest scores were reported to be 0 and 0.27 for HFC and zero crossing based methods

respectively. However, it can also be noticed that the HS detection performance drops with low cadence (lowest F1 score of 0.29). It is to be recalled here that the TO performance is the same as zero-crossing method since TO was detected in the same manner, as discussed in Chapter 2.

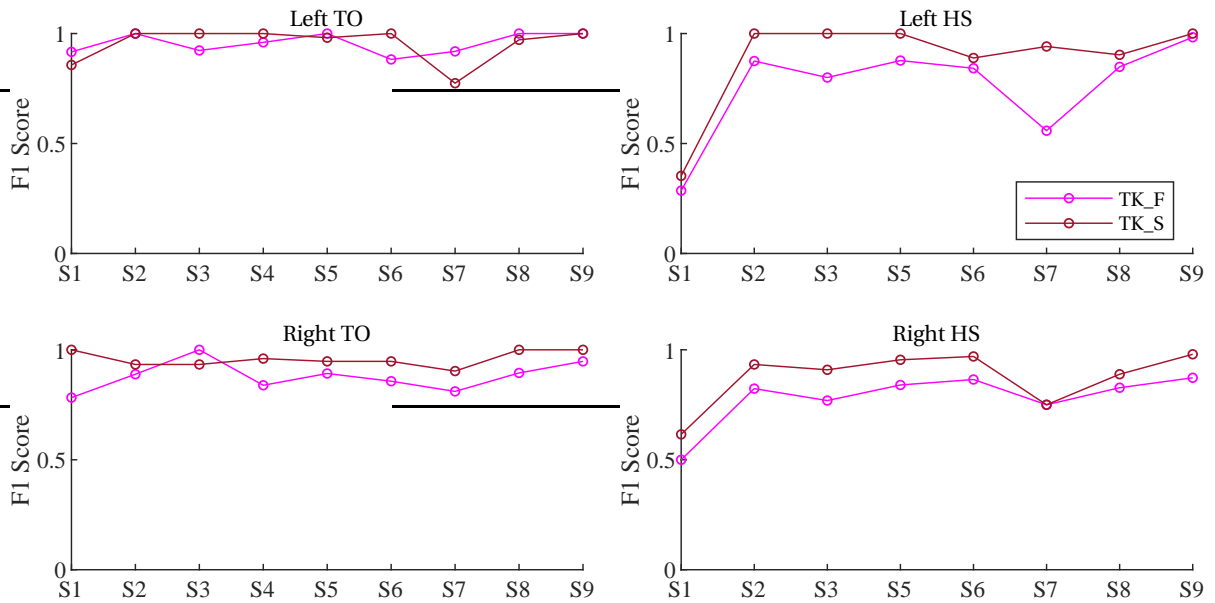


Figure 3.5: Gait detection using trunk kinematics together with peak heuristics: Figure shows the performance (F1 score) of the method when tested using IMU signals from foot (TP_F) and shank (TP_S) against all the walking scenarios discussed earlier.

In Figure 3.6, the corresponding latencies are reported as compact box plots. Despite the high overall detection performance, it can be noticed that the latency is relatively high for HS detection, with an average of median latencies across scenarios close to 100 ms, which is much higher compared to the 20 ms reported by zero-crossing based method with foot IMU signal.

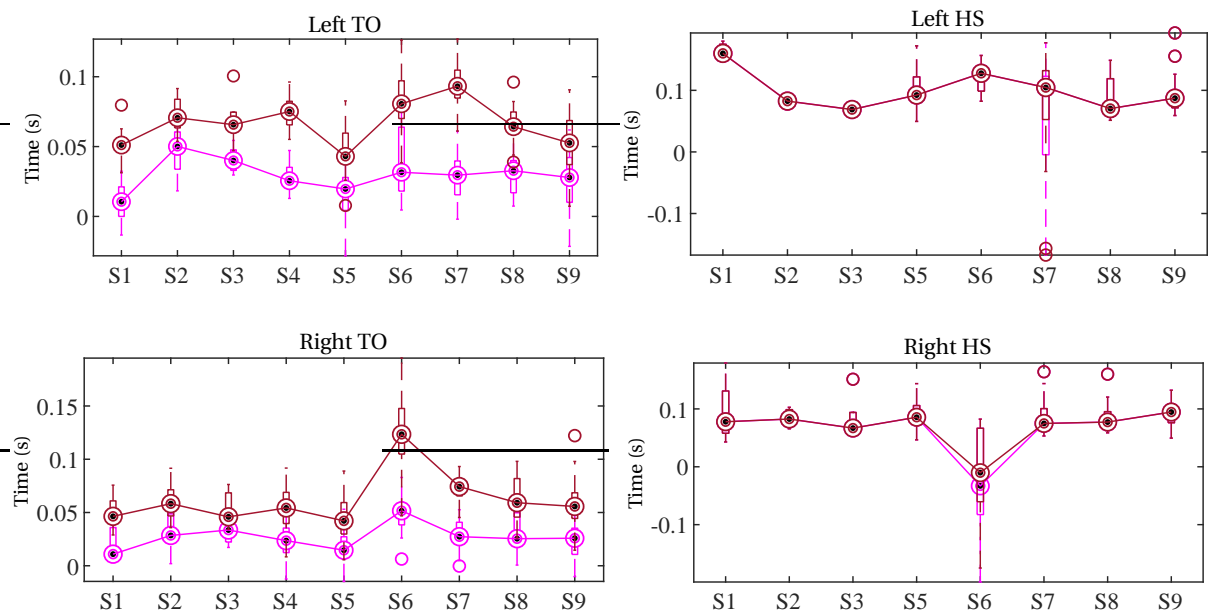


Figure 3.6: Gait detection using trunk kinematics together with peak heuristics: Figure shows latency in detection when tested using IMU signals from foot (TP_F) and shank (TP_S) against all the walking scenarios discussed earlier. Conventions described in Figure 3.2 applies.

3.1.4. BENCHMARKING

The best of the results from the previous sections are compared against a real-time gait event detection method proposed in [18] (here after simply called the benchmark method). The method reports a 100% detection rate when tested on healthy subjects as well as on trans-femoral and trans-tibial amputees. The rule-based method, implemented using threshold and peak detection, is as illustrated in Figure B.5.

The results obtained when the method was tested on the mimicked dataset, is presented here. It can be noticed from Figure 3.7 that the TO detection performance of benchmark method drops noticeably for most of the scenarios, except during normal walking. But it can also be observed that the performance during HS detection is high with a minimum F1 score of 0.83 (corresponding to gait assymetry). However, it can also be noticed from Figure 3.8 that TO is detected earlier than it should have been, with an average of median latencies across scenarios at around -43 ms for right TO and -52 ms for left TO.

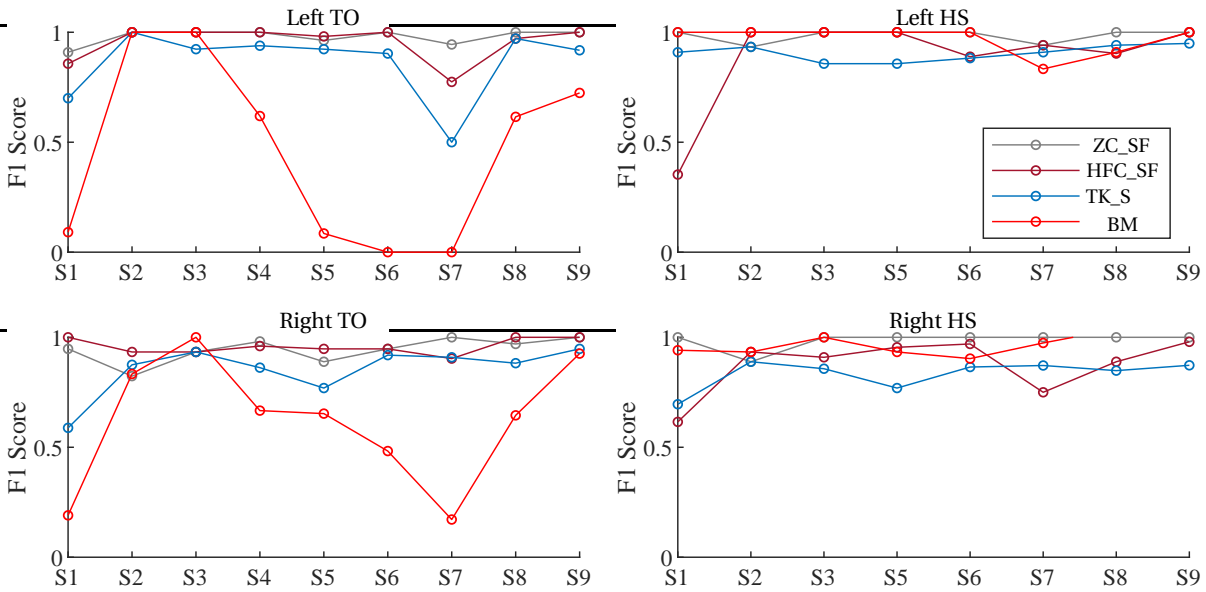


Figure 3.7: Benchmarking: Comparing the best of solutions from the previous cases with literature. Figure shows the performance (F1 score) of the best configurations from all the three methods discussed earlier together with the performance of Benchmark Method.

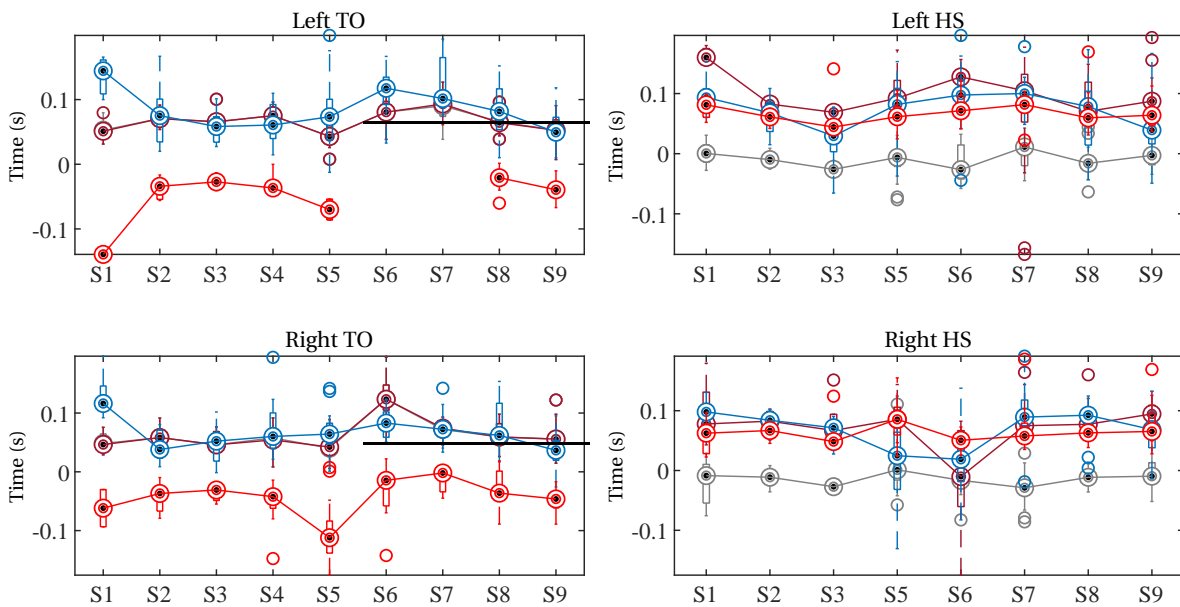


Figure 3.8: Benchmarking: Comparing the best of solutions from the previous cases with literature. Figure shows the latency of the best configurations from all the three methods discussed earlier together with latency of BM. Conventions described in Figure 3.2 applies.

3.1.5. TESTING WITH PATIENT DATASETS

TESTING ON AIS-D GAIT DATA (D1)

The proposed heuristics based method using zero crossing was tested on the D1 dataset, results of which are presented in Figure 3.9. Note that since there was no toe marker available in the motion capture data, ground truth gait events could not be labelled, and thus no quantification of results (F1 score and latency) could be reported. However, it can be visually observed from the location of each gait event in the snapshot provided that the method plausibly identified both the gait events 9 out of 10 times correctly with the only likely mis-detection being around $t=38$ s.

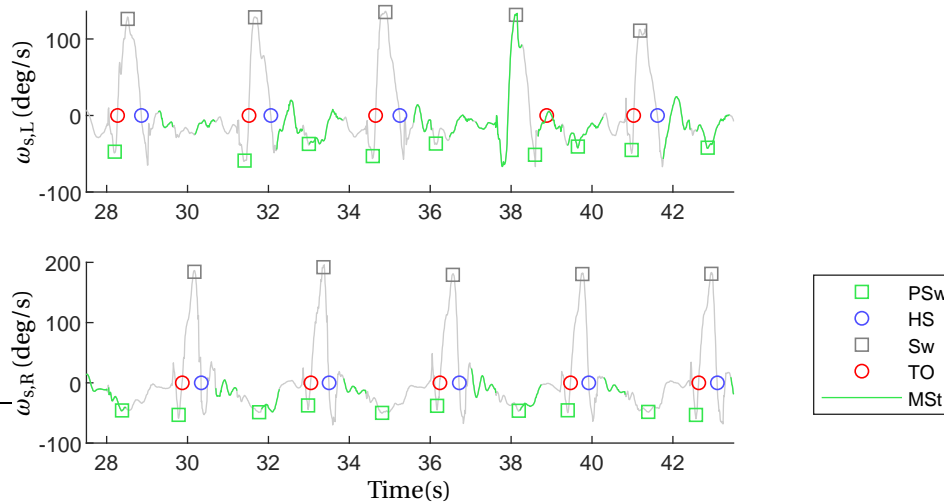


Figure 3.9: Test results for the proposed heuristics based method using zero crossing when tested on D1 dataset is presented here. Upper plot shows the sagittal plane angular velocity of shank for the left side ($\omega_{s,L}$) together with the events and phases detected while the lower plot shows the same for the right side.

For comparison, the benchmark method was tested on the same dataset (D1), results of which are presented in Figure 3.10. It can be observed from the current snapshot that while all the HS events were plausibly detected correctly, none of the TO events seem to be detected correctly.

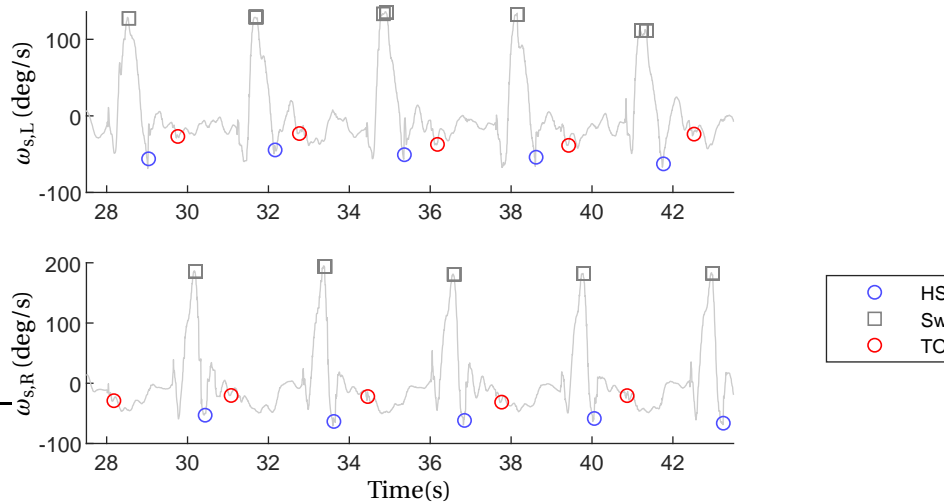


Figure 3.10: Test results for the benchmark method on dataset (D1). Upper plot shows the sagittal plane angular velocity of shank for the left side ($\omega_{s,L}$) together with the events and phases detected while the lower plot shows the same for the right side. It can be observed from the current snapshot that while all the HS events were detected correctly, none of the TO events were detected correctly.

Note that since the trunk kinematics data was not part of any of the patient datasets discussed in Table 2.1, the proposed heuristics based method using trunk kinematics could not be tested on patient datasets. Further, because of the high latency and computational demand by the proposed heuristics-based method using high frequency content, it made little sense to test the method here as the micro-processor originally

being used in the neuro-stimulator system has much limited computational resources compared to the PC where the current tests were carried out.

TESTING ON AIS-B GAIT DATA (D3)

The proposed heuristics based method using zero crossing was tested on the D3 dataset, results of which are presented in Figure 3.11. The result obtained for the left shank is shown in the upper plot while for the right shank is shown in the lower plot, together with the events and phases detected as well as the ground truth events.

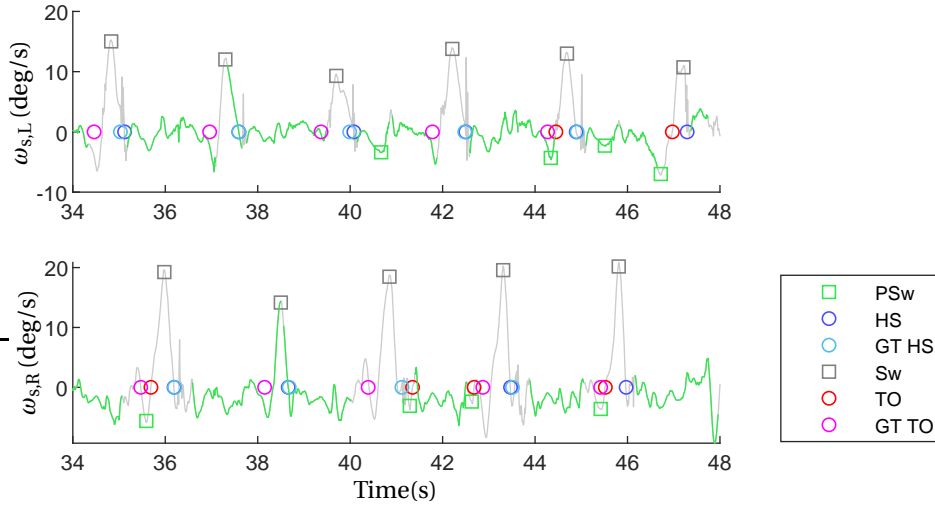


Figure 3.11: Test results for the proposed heuristics based method using zero crossing when tested on D3 dataset is presented here.

The quantitative analysis of the above test is presented in Table 3.1. For HS, the F1 score was observed to be 0.8293 for both legs while for TO, it was observed to be much lower at around 0.2353 for right leg and 0.2424 for left leg.

ZC_S	TP	FN	FP	Precision	Recall	F1 Score
RTO	4.0000	16.0000	10.0000	0.2857	0.2000	0.2353
LTO	4.0000	12.0000	13.0000	0.2353	0.2500	0.2424
RHS	17.0000	1.0000	6.0000	0.7391	0.9444	0.8293
LHS	17.0000	2.0000	5.0000	0.7727	0.8947	0.8293

Table 3.1: The performance score of the proposed heuristics based method using zero crossing when tested on D3 dataset is presented in the table. F1 scores along with precision and recall, number of TP, FP, and FN are reported. ZC_S - Zero crossing based method tested with signals from shank mounted IMU. TP - (number of) True Positives, FP - (number of) False Positives, TN - (number of) True Negatives.

The corresponding latency distribution in detection is reported in Figure 3.12. HS events were detected with a median latency of around 40 ms for the left leg while around -10 ms for the right leg. Detection of TO events resulted in higher latency, with a median at around 180 ms for the left leg and 130 ms for right leg.

For comparison, the benchmark method was tested on the same dataset (D3). The result obtained for the left shank is shown in the upper plot in Figure 3.13 while for the right shank is shown in the lower plot, together with the gait events and phases detected as well as the ground truth events. It is to be noted here that because the leg movements of this subject were slow (as can be observed from the maximum value of angular velocity in the plot), the threshold values for the benchmark method had to be reduced proportionately as the method was otherwise not detecting any gait events at all.

The quantitative analysis of the above test is presented in Table 3.2. The F1 score observed for right HS was 0.7692 while that for left HS was around 0.6154. For TO, the score obtained was around 0.0526 for right and 0.3333 for left leg.

The corresponding latency in detection is reported in Figure 3.14. HS events were detected with a median latency of around 110 ms for left leg while at 70 ms for the right leg. Detection of TO events resulted in similar latency, with median at around 105 ms for the left leg and 70 ms for right leg.

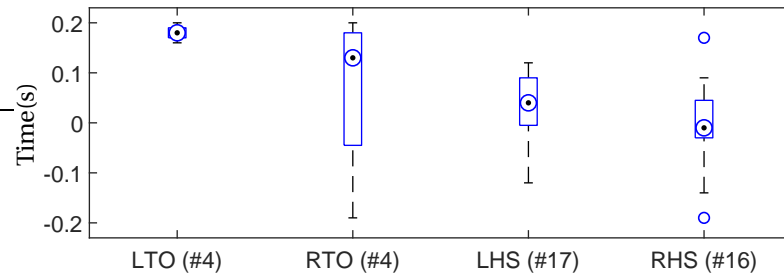


Figure 3.12: The latency of the proposed heuristics based method using zero crossing when tested on D3 dataset is presented in the figure. In the parenthesis, the number of gait events used for the evaluation (the number of true positives) is also listed. For instance, 17 left heel-strike gait events were compared to the corresponding ground truth HS events to estimate the latency distribution.

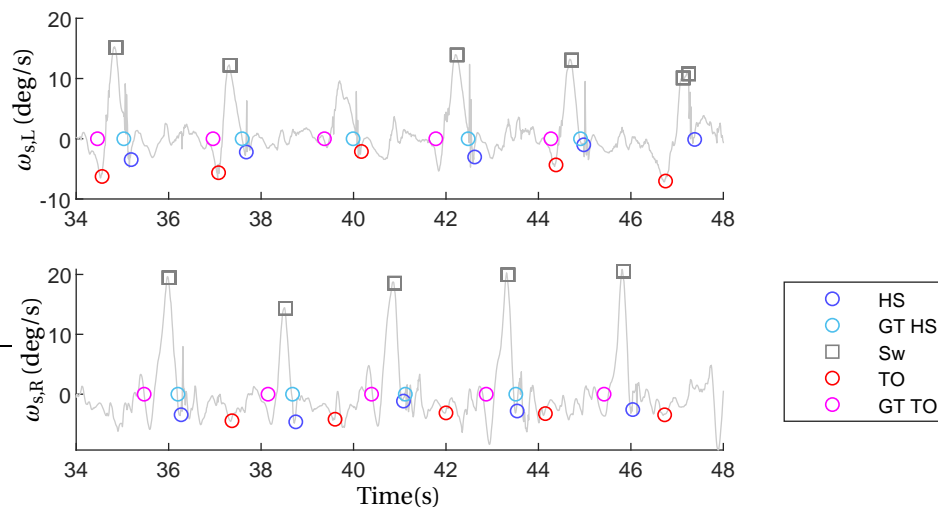


Figure 3.13: Test results for the benchmark method when tested on D3 dataset is presented here.

BM	TP	FN	FP	Precision	Recall	F1 Score
RTO	1.0000	19.0000	17.0000	0.0556	0.0500	0.0526
LTO	6.0000	10.0000	14.0000	0.3000	0.3750	0.3333
RHS	15.0000	3.0000	6.0000	0.7143	0.8333	0.7692
LHS	12.0000	7.0000	8.0000	0.6000	0.6316	0.6154

Table 3.2: The performance score of the benchmark method when tested on D3 dataset is presented in the table. F1 scores along with precision and recall, number of TP, FP, and FN are reported. ZC_S - Zero crossing based method tested with signals from shank mounted IMU. TP - (number of) True Positives, FP - (number of) False Positives, TN - (number of) True Negatives.

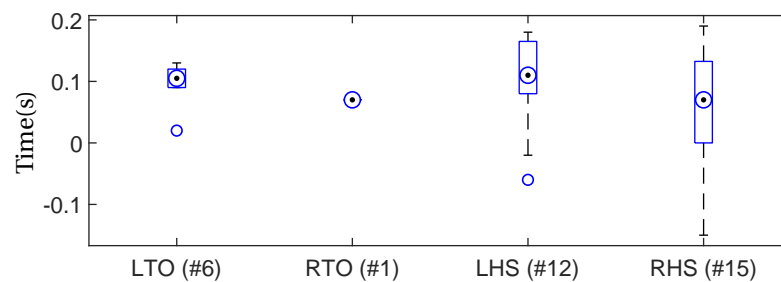


Figure 3.14: The latency of the benchmark method when tested on the D3 dataset is presented in the figure. In the parenthesis, the number of gait events used for the evaluation (the number of true positives) is also listed.

3.2. IMU EMULATION

3.2.1. SEGMENT AXIS STABILITY

In Section 2.3.1, we discussed about the formulation of rotation matrix, the additional constraint introduced in the rotation matrix and the weighted average proposition used for the same to ensure the axis stability. In Figure 3.15, we compare the pitch extracted with respect to the vertical axis of world frame (Vicon) to that of the pitch extracted from rotation matrix with and without the weighted average proposition to illustrate the axis stability. It can easily be seen that the constrain with weighted average significantly improves the axis stability, there by estimating the angle correctly.

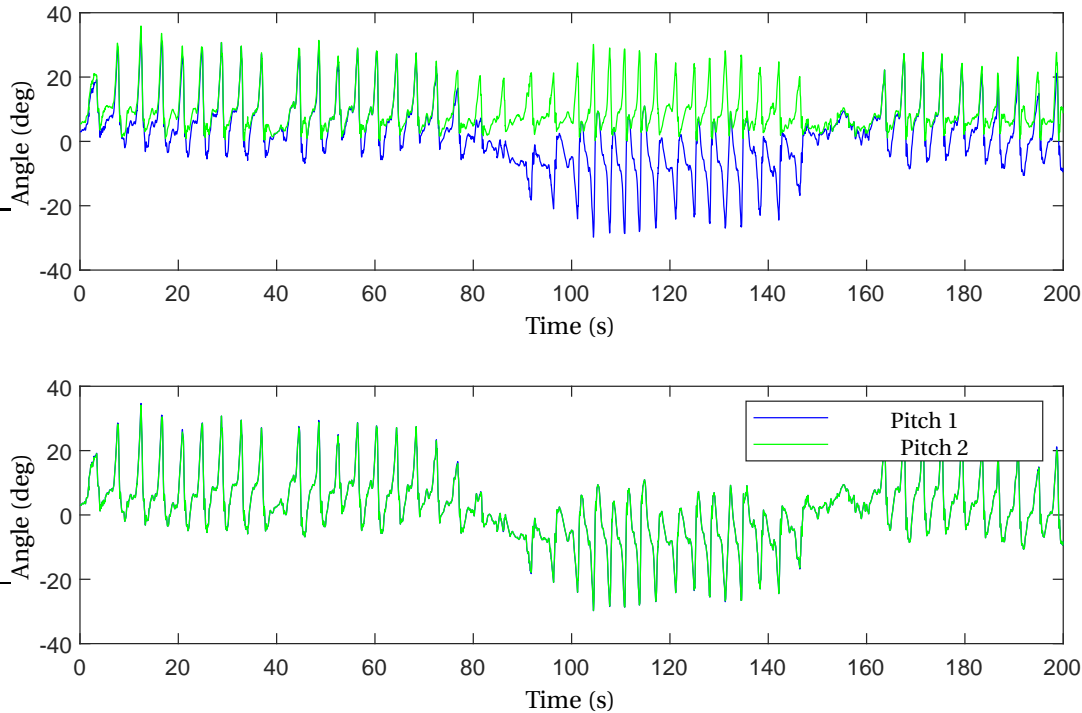


Figure 3.15: The shank pitch extracted with respect to the vertical axis of the world frame (Pitch 2) is compared with the pitch extracted from the rotation matrix (Pitch 1). Pitch 1 in the upper figure is without the weighted average proposition discussed earlier, while pitch 1 in the lower figure is with the weighted average proposition, thus justifying the choice.

3.2.2. CREATING SYNTHETIC IMU DATA

As discussed in the previous chapter, the IMU emulation method proposed was tested using the patient dataset D1 where both motion capture data (used for emulating IMU signals) and IMU data (used for validation) were available. The result of IMU emulation for left shank is as shown in Figure 3.16. First, the emulated signals were calculated from the motion capture data and was then compared to the actual IMU signal to assess the feasibility of the method. Emulated angular velocity in sagittal plane (medio-lateral axis) comes very close to the gyroscope signal from the corresponding IMU, with a correlation value around 0.977. Other component signals such as the angular velocity in anterior-posterior axis and acceleration in superior-inferior axis follow closely with correlation values of 0.747 and 0.793 respectively, as shown in the figure.

3.2.3. TIME SYNCHRONIZING IMU AND MOTION CAPTURE DATA

The method proposed in Section 2.3.3 for time synchronization was tested with the patient dataset D2, result of which is presented here. The IMU emulation was performed first, after which the signals are resampled to have the same sampling frequency and then the cross-correlation is evaluated to identify the delay in number of samples. This is illustrated in Figure 3.17 from where it can be noted easily that there is a delay of 344 samples between the signals in the current example. The delay thus obtained was used to synchronize the original IMU data to original motion capture data. The post-synchronized signal for sagittal plane foot angular velocity is as shown in the lower plot.

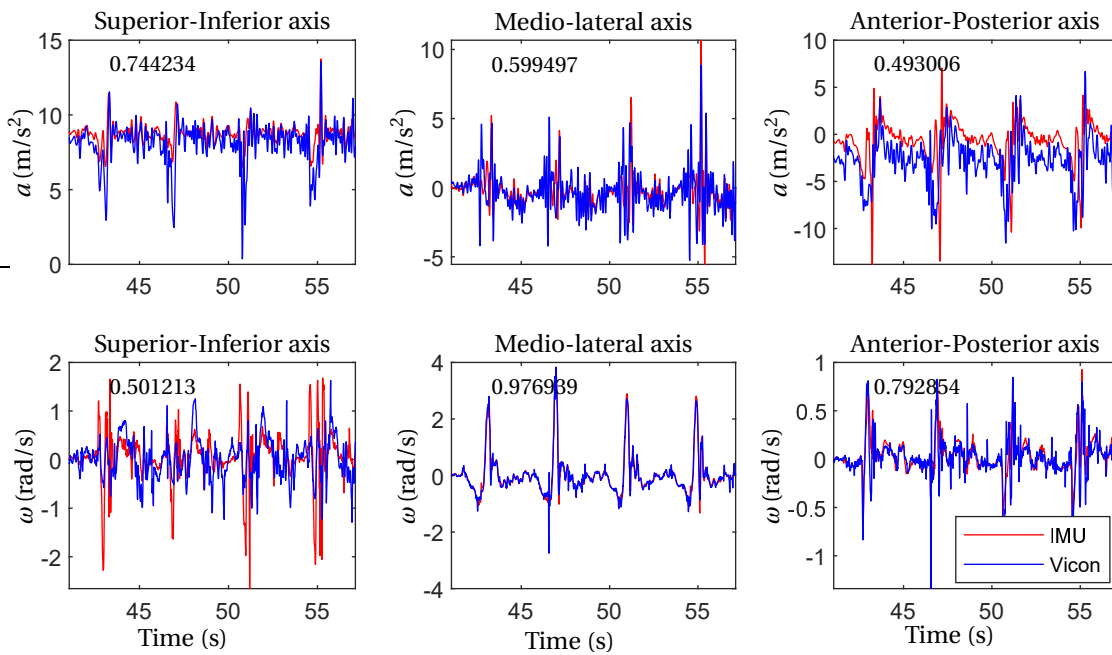


Figure 3.16: IMU emulation results for all the 6 axis of the IMU (3 acceleration components and 3 angular velocity components) are shown in figure with the corresponding cross-correlation value printed on top of it. The legend Vicon represented IMU signal emulated from Vicon while the legend IMU represents the original signals from IMU. It can be noticed that the emulated angular velocity along medio-lateral axis very closely follows the original signal from the IMU.

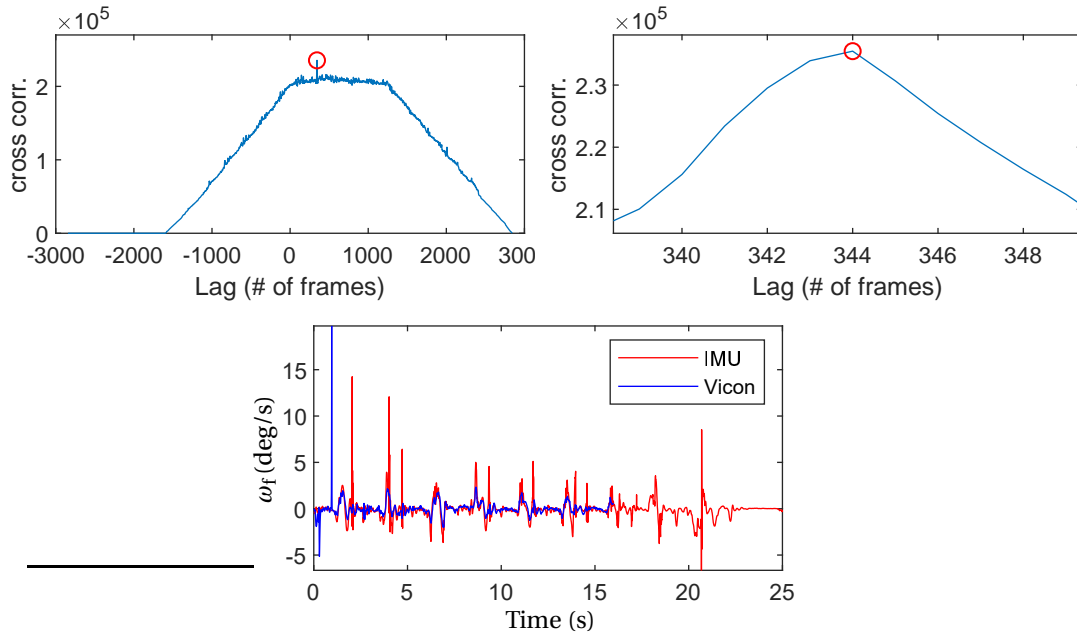


Figure 3.17: Upper left figure shows the cross-correlation plot with respect to number of frames. The red circle highlights the sharp peak which corresponds to the exact number of frames by which the signals need to be synchronized. The upper right figure is a zoomed-in version of the left figure, from which it can be noted that the delay is exactly 344 samples in this example. The delay of 344 samples thus observed was used to explicitly time-synchronise the original IMU data to original motion capture data. The delay thus obtained was used to synchronize the original IMU data to original motion capture data. The sagittal plane angular velocity of foot (ω_f) thus synchronized is as shown in the lower plot.

4

DISCUSSION

4.1. GAIT DETECTION

4.1.1. PEAK HEURISTICS IMPROVES ROBUSTNESS

As we discussed earlier in Figure 3.7, the proposed method with peak heuristics improves robustness of gait detection significantly across all scenarios (in the mimicked dataset) when compared to the benchmark method. The low TO detection rate of the benchmark method was observed to be due to the strategy used for pre-swing peak detection (inflection point detection based on 3 data points after reaching the minimum threshold). We observed the algorithm to incorrectly identify other local peaks as pre-swing peaks, as shown in Figure 4.1. Note that although we re-created the method solely based on the information described in [18], the 100% detection rate corresponding to S2 and S3 (normal walking at medium and high cadence), as was also reported by 4.1, confirms that the re-implementation of the benchmarking method was done correctly. It is also to be noted that although [18] tested for three conditions (low, normal and medium cadence), it was noted that their low cadence corresponded to our medium cadence and their medium cadence corresponded to our high cadence. Thus, it can be seen that the benchmark method was not really prepared to work with cadence as low as the ones dealt with in the present study (S1) which explains why the performance of the benchmark method is poor for S1. Further, the strategy used for HS detection in benchmark method, although detecting events with good performance, adds significant delay (between 70-90ms). This is because HS is detected based on loading response peak, which indeed happens after the heel strikes the ground.

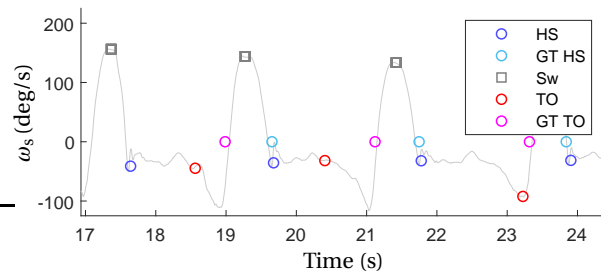


Figure 4.1: A snapshot from the result of the benchmark method when tested on S2 dataset. Note how the TO event (red marker) was mis-detected. In the first two gait cycles shown, some of the low prominent local peaks are incorrectly identified as pre-swing peak and hence TO. However, it can be noticed that in the third gait cycle, the event is detected correctly. GT - Ground Truth.

The enhanced robustness of using peak heuristics together with zero crossing is evident from the lower plot in Figure 3.9 where it can be observed that despite the system identifying back-to-back potential PSw peaks, the algorithm still manages to identify the TO event correctly. On the other hand, the benchmark method which accepts PSw peak directly as TO event, fails to identify any TO event correctly, as can be observed in Figure 3.10. It can thus be concluded that the proposed heuristics-based method improves robustness of real-time gait event detection, not only for the mimicked data, but also for the patient data. To the best of the author's knowledge, the proposed method is unique in itself and no similar studies could be identified from the literature.

4.1.2. FOOT IMU SIGNAL ALONE MAY BE INSUFFICIENT FOR SCI GAIT DETECTION

Of all the walking scenarios considered in the study, it was illustrated earlier that foot drag was contributing to the one of the most deviating gait patterns (see Figure 2.2) and this had the most significant effect in the foot IMU signals. It can also be noted easily from the results presented in the previous chapter that the performance of the proposed methods dropped when the IMU was placed at the foot than when it was at the shank, particularly during foot drag. Neither of the methods based on the foot IMU signal alone could predict HS event robustly in the presence of foot drag, as shown earlier in Figure 3.1 and Figure 3.3. This is due to the fact that the swing peak is split or scattered when the foot is dragged across the floor, as can be observed in Figure 2.1 which is also reflected in Table 2.3. As far as gait detection algorithms are concerned, swing peak is typically the most prominent feature that can be identified from the signal (angular velocity in sagittal plane) and it is exactly this feature that gets affected by the foot drag, making gait detection using foot IMU signals difficult (see Figure 4.2). With foot drag being common in SCI gait, the method is not expected to perform well in patients when the IMU is placed at the foot, despite the foot-based methods performing well in all other scenarios with low latency.

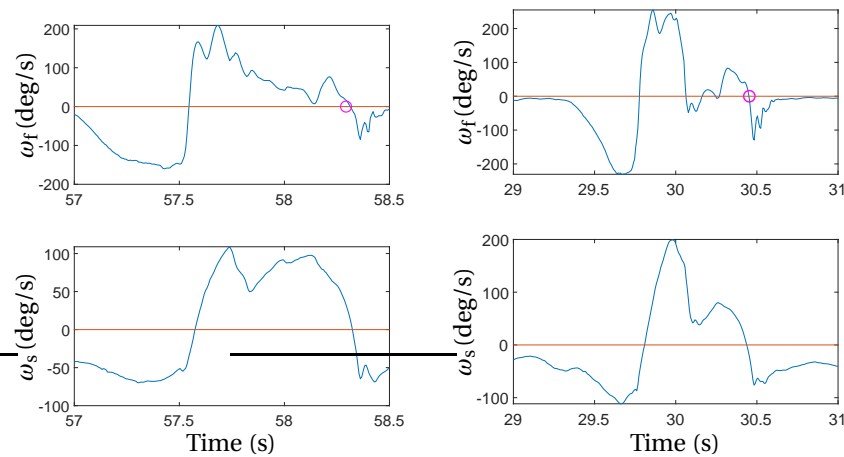


Figure 4.2: Two gait cycles involving foot drag are shown here. The upper figures show the right foot angular velocity while the lower figures show the corresponding shank angular velocity. The gait cycle shown in the right is much more impacted by the foot drag as the swing peak of foot angular velocity crosses the zero line much before the actual foot strike (shown by the pink marker). While the gait cycle in left is not going to impact the proposed solution based on zero crossing, the second gait cycle may result in an incorrect solution since the first zero crossing after swing peak will be taken as HS.

Although not part of this study, it was at a later stage noted that foot crossing is also another commonly observed problem in SCI gait which distorts the swing peak. This happens due to insufficient stimulation in the hip abduction muscles. The new electrodes for spinal cord stimulation being developed by GTX with improved specificity may address this issue.

4.1.3. SHANK/TRUNK KINEMATICS ENHANCES ROBUSTNESS OF HEEL STRIKE PREDICTION

As illustrated in Figure 4.2, most of the disturbances or deviating gait patterns observed in foot angular velocity are much less prominent in the shank angular velocity profile. This is believed to be contributed by the following factors:

1. The high frequency contents are less prominent in shank IMU signal than the foot, thereby reducing spurious deviations in the signal.
2. Appropriate shank movement is more of a necessity in enabling a step than the foot movement. For instance, subjects who have foot orthosis are still able to walk despite the movement being restricted by the orthosis while it might be much more difficult to make a step when shank movement is restricted.

Although the robustness increases for both TO and HS prediction, the delay in TO prediction with shank IMU signal is somewhat higher as can be noted in Figure 3.2. This could be because TO event happens well before the shank zero crossing.

In the case of the trunk, the prominent peaks reported earlier corresponding to HS are observed to barely be affected by the disturbances at the foot. Although this is working fairly well for the current datasets, it

was noted that this feature is subtle; it has been observed that during gait asymmetry, instead of two peaks per gait cycle (one each for left and right HS), a third peak of similar characteristic (see Figure 4.3) was noted corresponding to the act of leaning towards one side of the body (to mimic gait asymmetry). This was also reflecting to some extent in the HS detection performance illustrated earlier in Figure 3.5. We are yet to have a dataset of patients with trunk IMU data; it thus remains to be seen how trunk kinematics based method would perform well in patients; the influence of body weight support system and other undesirable movements created by patients may affect the performance of the method.

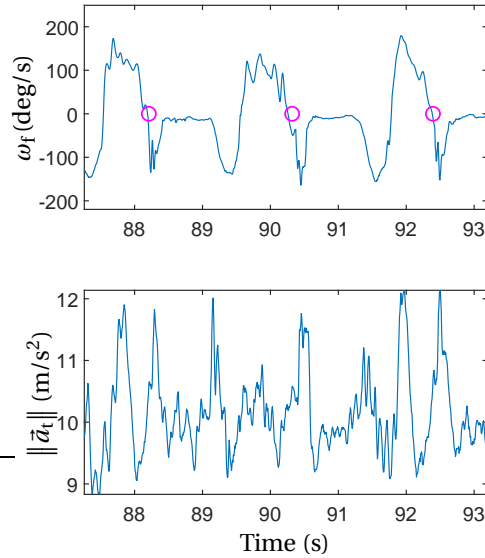


Figure 4.3: The Norm of Accelerometer (NoA) signal of the trunk IMU signal is shown in the lower figure. (The foot angular velocity is shown in the upper figure for reference.) The additional peak (3 peaks per gait cycle instead of 2) is the reason why trunk based HS detection performance drops with gait asymmetry.

4.1.4. WAVELET TRANSFORM MIGHT BE UNSUITABLE FOR REAL-TIME APPLICATIONS

Despite wavelet transform being tested outside a simulated real-time environment (so as to eliminate the impact of computational latency on the performance of method), the latency in detection alone was much higher than zero-crossing based method (which was indeed tested in a simulated real-time environment, meaning the latency included also the computational delay). Although we tried to keep the latency as low as possible by considering only the high frequency content, it was still not sufficient, with median latencies going as high as 150 ms without even considering the computational latency. Thus, it can be observed that wavelet transform based gait detection is only suitable for quasi-real-time systems and not strictly real-time systems, which is in-line with the observations made by previous gait detection studies that used wavelet transform ([28], [27], [31]).

4.1.5. LIMITATIONS OF THE MIMICKED DATASET

Although the proposed method performs well with the mimicked dataset (which was recreated based on patient video references), the dataset has been observed to have the following limitations:

1. The jitter (undesirable oscillations, for instance in the stance phase) is less in the mimicked dataset compared to the patient datasets (compare and contrast angular velocity profile in Figures 3.9 and 3.11 to 4.1). Overall, the mimicked dataset appears to be smoother and consistent than the patient datasets. Note that the natural human gait involves real-time control of hundreds of muscles working in synergy with each other while the therapy on the other hand only stimulates the bare minimum muscles groups necessary to perform a step. Thus, some gap between the mimicked dataset and actual patient dataset is inevitable.
2. It is to be noted that the mimicked dataset was not influenced by stimulation, body weight support system or walker.

3. Foot crossing was not part of the study, despite it being prominent in many SCI patients, as observed at a later point in time.
4. The scenarios were replicated separately in the mimicked dataset while the actual patient data may have several scenarios appearing together in the same gait cycle.
5. The prominence of pre-swing peak in some of the patient datasets is much less prominent than in the mimicked dataset (see Figure B.2). This might be contributed by the lack of specificity of the therapy to target foot muscles. For instance, due to limited specificity of electrodes used for spinal cord stimulation or because the appropriate nerves cannot be targeted specifically (for instance, peroneal nerves innervating the ankle dorsiflexor muscles run down the leg as part of the sciatic nerves). It could also be argued that the usage of foot orthosis might be restricting the natural foot movement and thus the reduced P_{Sw} peak prominence, but it can also be noted that the prominence is low, not just for foot IMU signals, but also for shank (see 3.11).

4.1.6. CAUSAL DILEMMA: PATIENT-GROUP-SPECIFIC STRATEGIES MIGHT BE NECESSARY

The gait detection method in its current form expects P_{Sw} before it can detect TO. The therapy on the other hand is to be designed to deliver the stimulation block only after the corresponding gait event is detected, which means it expects the patient to initiate some movement. This presents a causal dilemma, especially when the patient has a complete loss of motor control. AIS-A and -B patients who have complete loss of motor control can barely initiate any movement in the lower limbs for the gait detection method to pick up and thereby deliver further stimulation. AIS-C or -D patients on the other hand can influence some residual movements in lower limbs, thereby being able to initiate the gait, from where the gait detection method can pick up and in turn deliver further stimulation. When comparing the result obtained for D1 (Figure 3.9) to the result obtained for D3 (Figure 3.11), it can be seen that the TO detection performance is significantly low in the latter, which is in-line with our observation. Thus, patient-group-specific strategies might be necessary. For patients who can influence some degree of residual movements, gait detection alone might suffice while for the other group of patients, further motion intention recognition methods may be necessary, for instance based on upper body kinematics.

4.2. IMU EMULATION

4.2.1. ANGULAR VELOCITY

The high correlation value (0.977) of emulated angular velocity in sagittal plane with the actual IMU signal, as presented in the previous chapter (see Figure 3.16), could be due to the effectiveness of additional constraint introduced in establishing the relationship between the local and global co-ordinate systems despite using less than 3 markers per segment. It could also be contributed by the fact that, for the specific dataset, the sensor co-ordinate system of IMU in that segment was aligned as much close to the body-fixed frame established between the two markers in that segment. On the other hand, the relatively lower correlation values for the other two directions (0.8 and 0.5) could be contributed by the fact that only two markers were used utmost per segment, thus not having sufficient information to extract the full 3D information about the segment. This is particularly true of the longitudinal axis (superior-inferior axis) which is much more difficult to be constrained with the limited set of markers than the anterior-posterior axis and hence the lower score (0.5).

4.2.2. LINEAR ACCELERATION

The position of the actual IMU in the segment was unknown. This motivated to make the assumption that the IMU is placed exactly at the midpoint between the two markers of the segment. However, this is often not the case practically. Markers are typically placed on the lateral side of the body, such as the lateral epicondyle for the knee or the lateral malleolus for the ankle (as suggested in the Vicon® Plug-in-Gait marker placement protocol) or the grand trochanter for the hip (easy to feel by palpation) while the IMU is typically placed on the anterior side of the body segment (front of the shank, on the tibia bone). This means that even in the best-case scenario where the IMU is placed at the middle of the segment and as much aligned to the body frame system as possible, the distance from the midpoint of the markers (on the lateral side) to the IMU (on the anterior side) is still unknown. Although this is not a significant problem for angular velocity (since angular velocity of a rigid body is the same at all points), this offset will affect the linear acceleration. This could be the reason for relatively low correlation coefficient for linear acceleration.

Another factor that could be affecting the quality of the result is error amplification due to double differentiation (double differentiation was necessary to calculate linear acceleration from marker positions). The effect is illustrated in Figure 4.4.

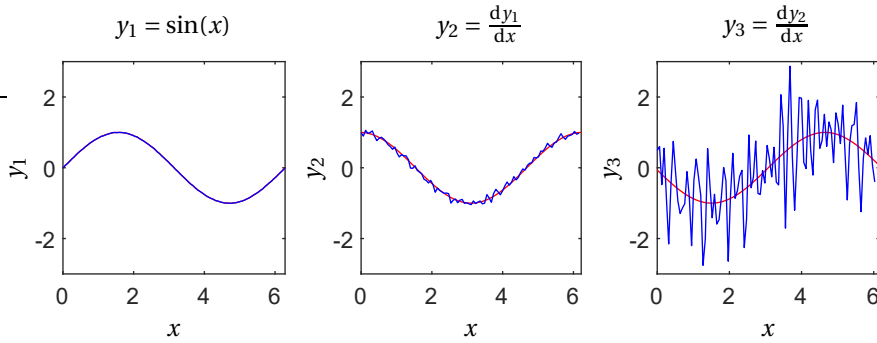


Figure 4.4: Illustration of noise amplification with double differentiation. There are two sine waves in the left most image, one with additional 1% white noise is in blue colour. Upon double differentiation, the noise amplifies as can be noticed in the right most image.

Further, the difference could also be contributed by the difference in the frequency components present in both sensing modalities. Markers are typically placed on bone landmarks which are easily identifiable by palpation, which means that the amount of soft tissue on it is less, compared to the IMU which is often placed on soft tissues (such as the anterior side of mid-thigh). The impact of the difference in strength of frequency components present between signals for sensors placed on rigid body parts and for those placed on soft tissues was already discussed (although in a different context) in Section 2.2 and illustrated in Figure 2.6.

4.2.3. TIME SYNCHRONIZATION

Results presented in Section 3.2.3 for time synchronization of IMU signals with motion capture data showed that the method worked as intended. This means that some of the existing datasets where motion capture data and IMU data are collected independently could be time synchronized explicitly during post-processing. This would enable the motion capture data to be used for ground truth validation, which was not possible before.

4.3. CONCLUSION AND FUTURE WORK

The primary aim of this thesis was to investigate the possibility of a robust real-time gait detection method for SCI patients based on IMUs. The project started off with a thorough systematic review from which several gait detection methods were identified. Because of limited patient datasets available especially at the beginning of the study, new datasets were created by studying video references of patients from the clinical study and mimicking it in the gait lab. A heuristic-based gait detection method with three variations of it - one using zero crossings of angular velocity in sagittal plane, one using high frequency contents extracted using wavelet transform and another one using additional trunk kinematics - was presented and tested with IMU signals from foot, shank and trunk. It was noted that the foot alone was an insufficient choice for robust gait detection of SCI patients due to noticeable jitter, while the shank and the trunk were observed to be offering better performance, but with increased latency. The shank was a reasonable trade-off between latency and detection performance. It was also observed that the high frequency content and trunk kinematics based approaches had very high latency, of the order of 70-100 ms. Overall, the performance of the method was observed to be better than the method used for benchmarking. The mimicked dataset had its limitations and did not involve as much intricacies and jitter as the patient datasets, but it enabled the study of several scenarios separately; among all the scenarios tested, it was learnt that foot drag was the toughest. Towards the end of the thesis, the proposed heuristics-based method was tested using zero crossing on patient datasets. The performance of both HS and TO detection on patient with motor-incomplete paralysis (AIS-D) was satisfactory as the algorithm detected 9 out of 10 gait events (both TO and HS) correctly. However, the performance of TO detection dropped when tested on the patient with motor-complete paralysis (AIS-B). We concluded that patient-group-specific strategies might be necessary and that motor-complete patients may require additional motion-intention-recognition strategies. Further, the newly developed IMU emulation tool has opened up the possibility to transform and make use of the existing patient datasets (although

collected with limited sensors) that were otherwise not very useful without ground truth validation. With new datasets and a way to transform the existing datasets to a useful form, this will also open up the possibility of using machine learning methods (which according to the systematic review was the most accurate method for gait detection) in SCI gait detection.



WAVELET TRANSFORM

A.1. INTRODUCTION

Fourier transform is a very useful tool to analyse the frequency distribution of a time series signal. While Fourier transform decomposes the time domain signal into corresponding frequency components, the frequency domain will have no notion of time and vice versa. This means that if we are interested in locating in time domain, the characteristic change in frequency of a signal, Fourier transform will not be sufficient. It is known that the kinematic gait signals collected using IMU (for instance, the angular velocity or the linear acceleration of the foot) exhibit such characteristic changes in frequencies during the moment of foot-ground interaction. This could potentially be used to identify gait events as proposed by [31].

Wavelet transform is a signal processing method to be used when the frequency content of a signal varies over time. The method can decompose a signal into both time and frequency domains simultaneously (the so called time-frequency domain). The method is similar to Fourier Transform in the sense that it deals with expansion of functions in terms of a set of basis functions. Such basis functions in the case of Fourier transform are typically infinite sine-wave basis functions. Since each sinusoid can have only one fixed frequency, Fourier transform is best suitable for signals composed of only stationary signals. Any sudden change in a non-stationary signal in the time domain analysed using Fourier transform will thus be spread over the whole frequency domain.

A.2. THEORY

In this section, the theory behind wavelet transform is discussed with some illustrative examples to highlight the potential of the method. For more detailed explanations, the reader is encouraged to refer [30] and [29].

There are several types of wavelets used with wavelet transform. One of the most simple and commonly used is Morlet wavelet which is formed by a complex sinusoid windowed with a Gaussian envelope. Figure A.1 illustrates the wavelet formation with a simple exponential function of the form $y_1 = e^{-\frac{x^2}{2}}$ multiplied with sinusoid $y_2 = \sin(x)$ resulting in

$$y = e^{-\frac{x^2}{2}} \sin(x), \quad (\text{A.1})$$

giving a simpler form of the Morlet wavelet. The complex form of the wavelet could be written as

$$y = e^{-\frac{x^2}{2}} e^{i2\pi x}, \quad (\text{A.2})$$

which follows from the Euler identity. Let $s(t)$ be a signal in the time domain and $\Psi(t)$ be the Morlet wavelet in the time domain, then the wavelet transform of the signal can be represented as

$$s(b, a) = \frac{1}{\sqrt{a}} \int_{-\infty}^{\infty} \Psi' \left(\frac{t-b}{a} \right) s(t) dt \quad (\text{A.3})$$

where Ψ' is the complex conjugate of the mother wavelet Ψ , b is the time shift parameter and a is the scale parameter. Equation A.3 can be re-written as

$$s(b, a) = \int_{-\infty}^{\infty} \Psi'_{a,b}(t) s(t) dt \quad (\text{A.4})$$

where

$$\Psi_{a,b}(t) = \frac{1}{\sqrt{a}} \Psi\left(\frac{t-b}{a}\right) \quad (\text{A.5})$$

Equation A.4 can be seen as an inner product between Ψ' and $s(t)$ which measures the similarity between the wavelet and the original signal. Equation A.5 can be viewed as the mother wavelet being shifted by 'b' and scaled by a factor 'a'.

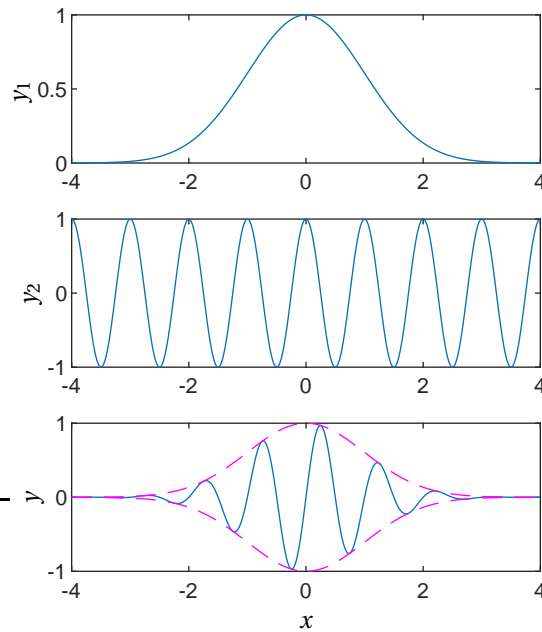


Figure A.1: Generating a simple Morlet wavelet by multiplying sine wave and Gaussian function

A.3. WAVELET TRANSFORM ILLUSTRATION

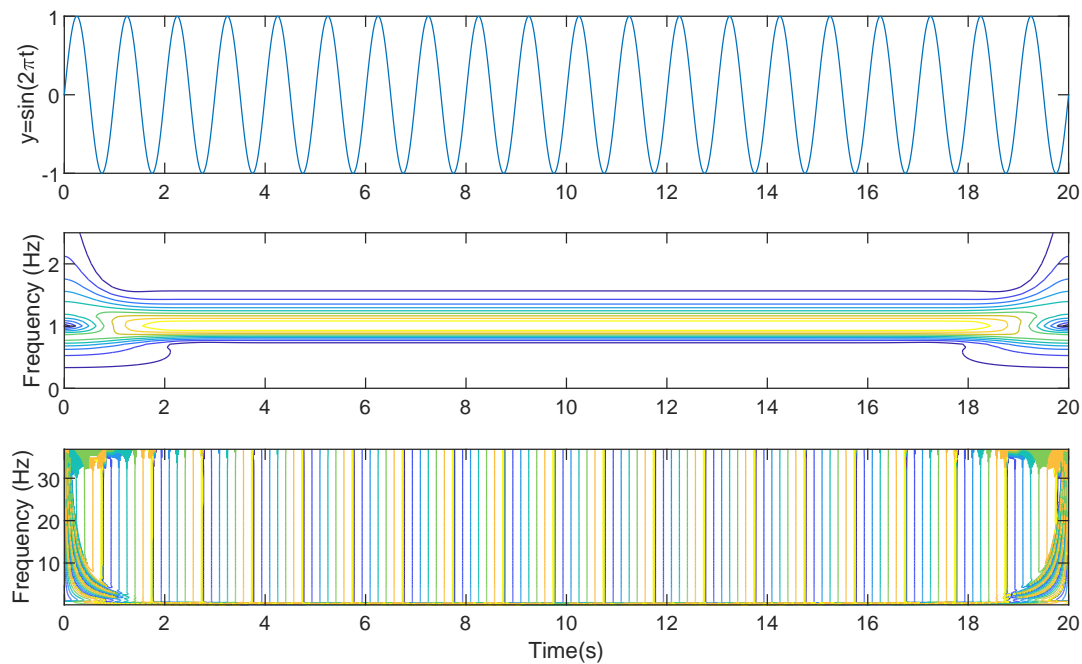


Figure A.2: The upper figure shows the signal in the time domain (a sine wave) while the middle and lower figures represent the contour plots of the magnitude and phase of wavelet transform of the signal. It can be noticed from the yellow region in the magnitude plot that the wavelet transform was able to extract the correct frequency of the sine wave (1Hz), much like what Fourier transform could have done.

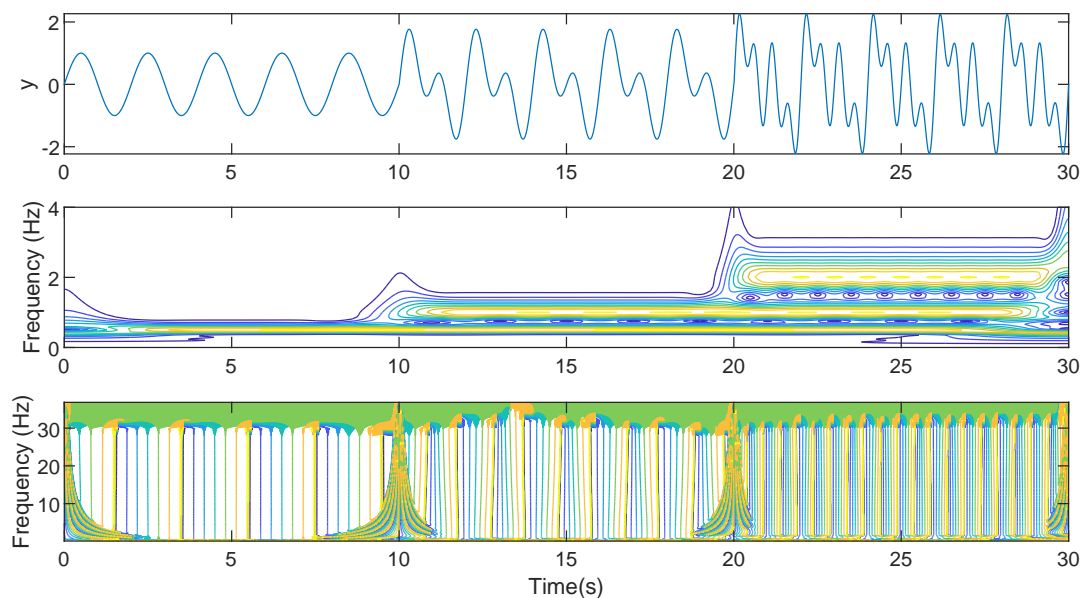


Figure A.3: The upper figure shows the signal in the time domain; a combination of finite sine waves, each starting at distinct points in the time domain. The middle and lower figures represent the contour plots of the magnitude and phase of wavelet transform of the signal. It can be noticed that the wavelet transform was able to extract the correct frequencies of all the three sine waves (1Hz, 1.5Hz and 2Hz). Not only that it extracted the frequencies, but it also **simultaneously** preserves the temporal information, meaning that it tells us, at what point the second sine wave at 1.5Hz starts and at what point in time, the third sine wave at 2Hz starts. This is something one cannot expect from Fourier transform.

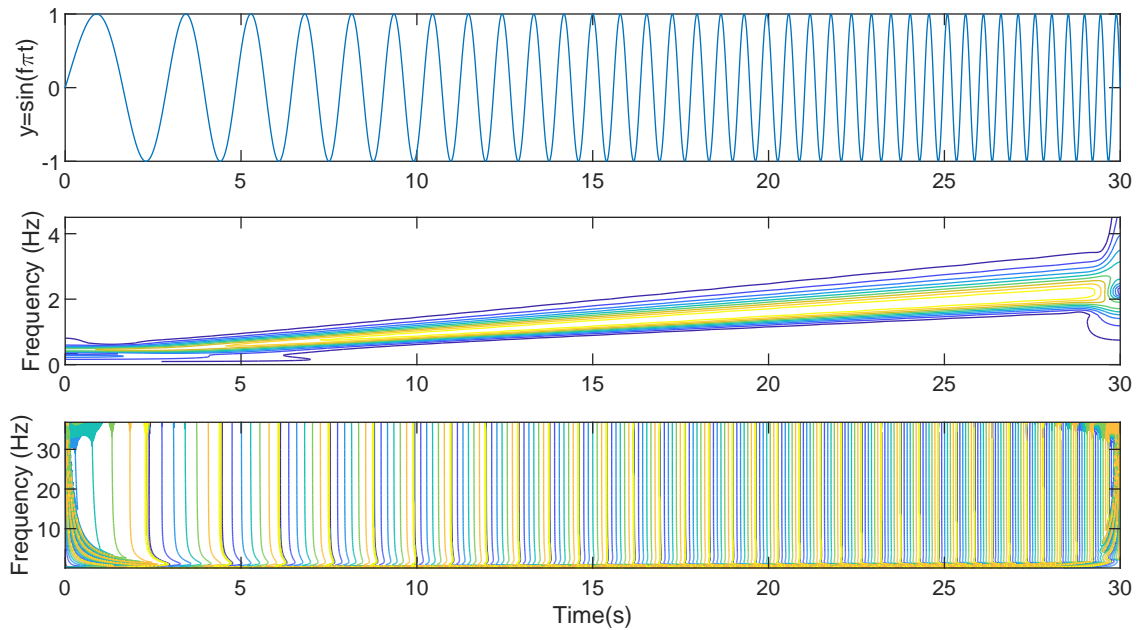


Figure A.4: An extended version of the example given in Figure A.3 is illustrated here, where instead of discrete frequency components, continuously varying frequency is used. As can be seen, wavelet transform can successfully resolve the signal in time-frequency domain.

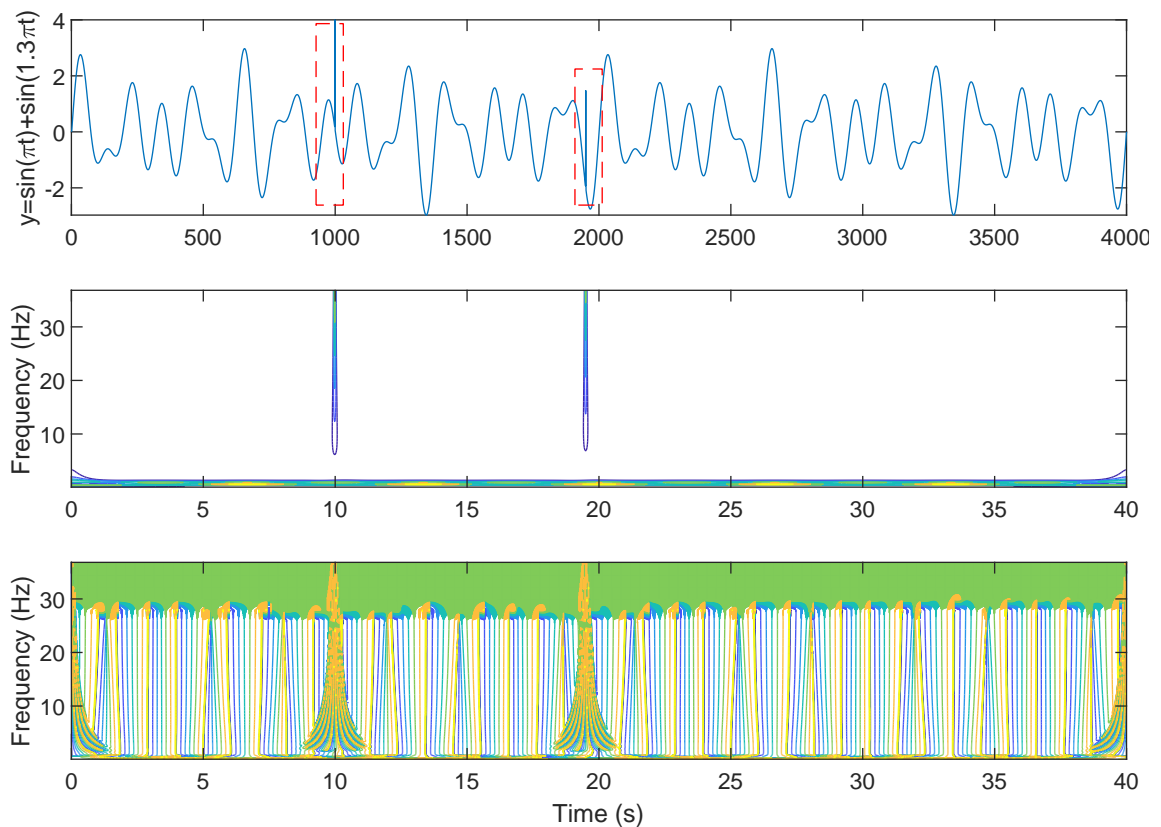


Figure A.5: In this example, together with a signal composed of 2 sine waves of different frequencies, Dirac-delta functions are introduced at specific points in time. These functions may, in practice, represent artefacts that are interesting to us, for instance for a specific event detection. As can be noticed in the upper figure, although the first impulse can be distinguished from the signal using a threshold, the second impulse is more "inscribed" and difficult to detect in the classical approach. However, since these are high frequency events, wavelet transform can easily pin point them as can be noticed in the middle figure.

A.4. WAVELET TRANSFORM AND GAIT SIGNALS

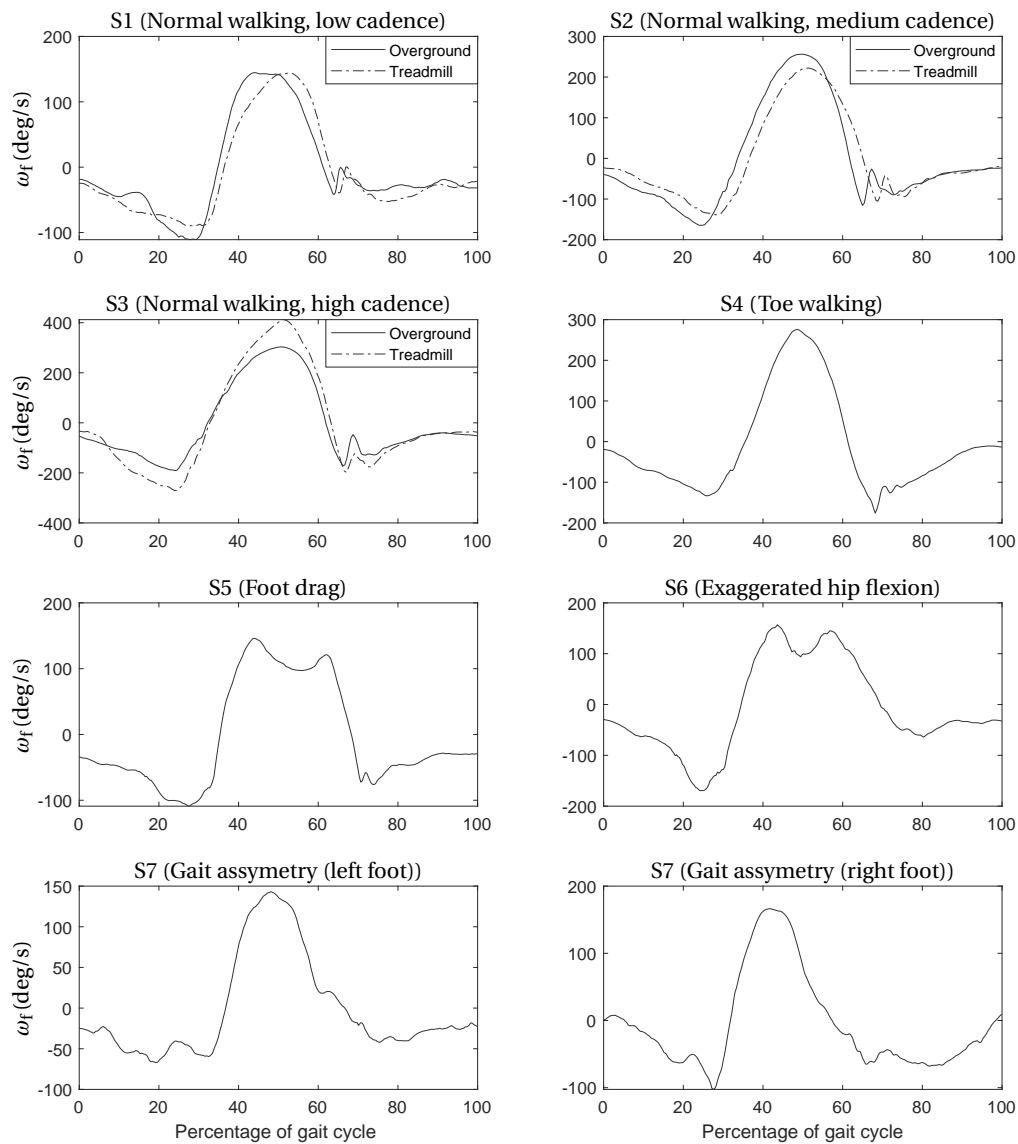


Figure A.6: Investigating the presence of characteristic peaks reported by [31] corresponding to TO and HS across multiple gait pathologies. It can be observed that the characteristic peaks (see Figure 1.8) can barely be identified across all pathologies, particularly during exaggerated hip flexion and gait asymmetry. Despite this "hidden feature" as it appears in the time domain, wavelet transform still manages to extract it as illustrated in Figure A.8.

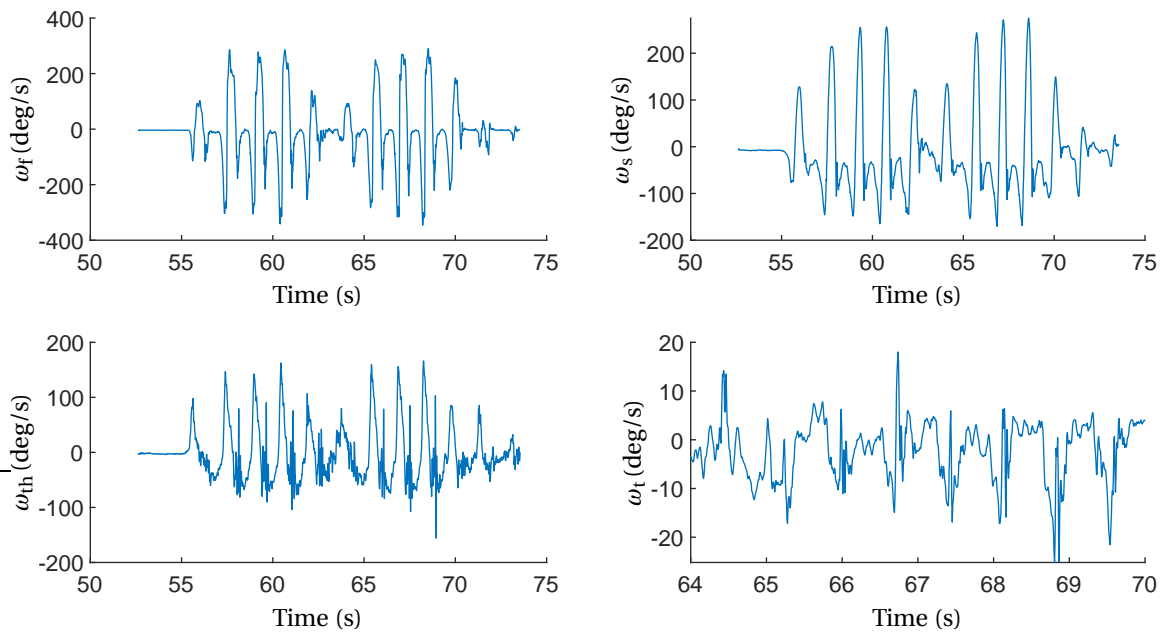


Figure A.7: Comparison of sagittal plane angular velocity foot (ω_f), shank (ω_s), thigh (ω_{th}) and trunk (ω_t) mounted IMU signals in the time domain. Contrast this with Figure A.8.

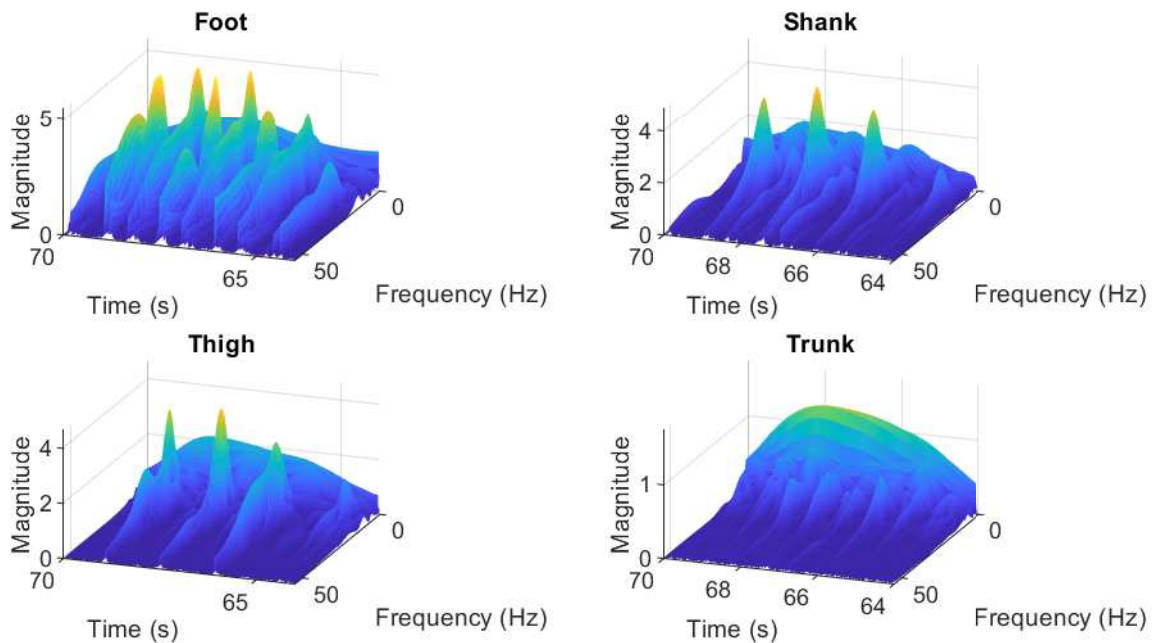


Figure A.8: Comparison of foot, shank, thigh and trunk mounted IMU signals in time-frequency domain, extracted using wavelet transform. It can be observed that the prominence of high frequency content in the signal reduces as we go higher up in the body.

A.5. CONE OF INFLUENCE AND INHERENT DELAY

Much like filtering a signal, wavelet transform also suffers from delay when used in real-time. This inherent delay is caused by the cone of influence; region where the wavelet transform results are not reliable any more. This is analogous to half the window width in linear phase filters, but here the "window width" varies continuously with frequency. Higher the frequency, smaller the delay and vice versa. This is because higher frequencies can be decomposed with compressed wavelets (thus smaller "window width") while lower frequencies need to be decomposed with stretched wavelets (thus higher "window width"). The cone of influence is as shown in Figure A.9. A consequence of the cone of influence is the edge effect, giving inaccurate result at the beginning and end of a signal (see Figures A.2, A.3, A.4, A.5). During off-line and quasi-real-time approaches using wavelet transform, this is not a problem. But in real-time systems that cannot tolerate much delay, this becomes significant. In real-time systems, often what we are interested in is the most recent signal received and that is exactly where the outcome is unreliable because of the edge effect. In the current study, we remedy this problem by only making use of high frequency content above 20 Hz, thus keeping the inherent delay as low as 25 ms.

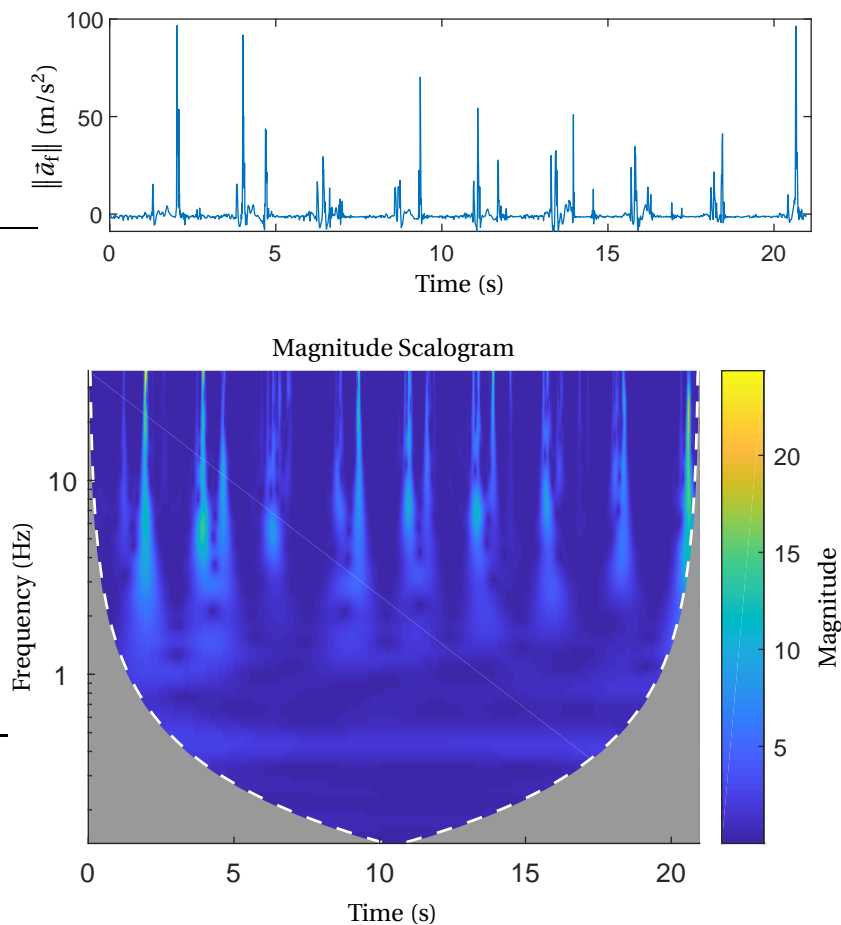


Figure A.9: The lower plot represents the wavelet transform with the grey region carved out representing the cone of influence (where the wavelet transform result is not reliable any more). The upper plot shows the foot norm of acceleration signal used as input for the wavelet transform.

B

SUPPLEMENTARY IMAGES

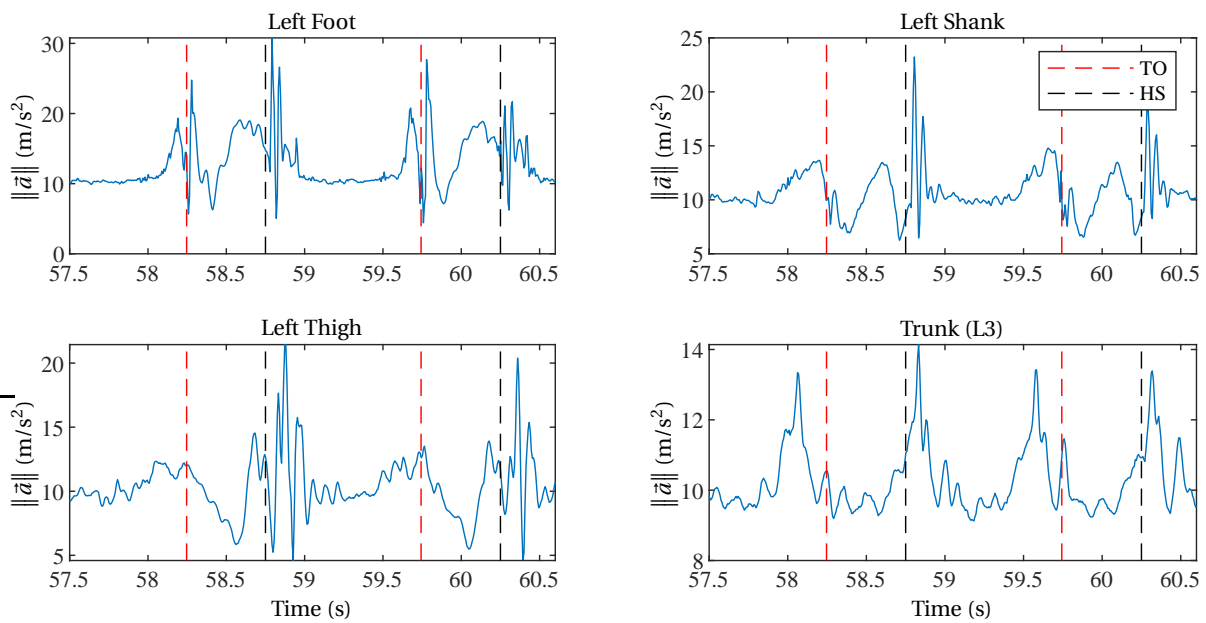


Figure B.1: Visualisation of the norm of the accelerometer signal of the trunk and the lower limbs together with the temporal location of the (ground truth) gait events during normal walking with medium cadence.

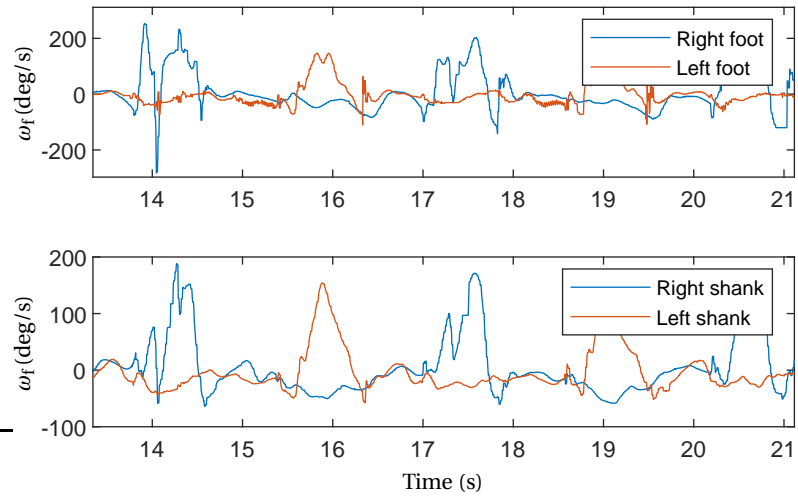


Figure B.2: Typical gait of an SCI patient as observed from one of the STIMO datasets. Note how much the gait patterns are deviating compared to a healthy subject's gait shown 2.1

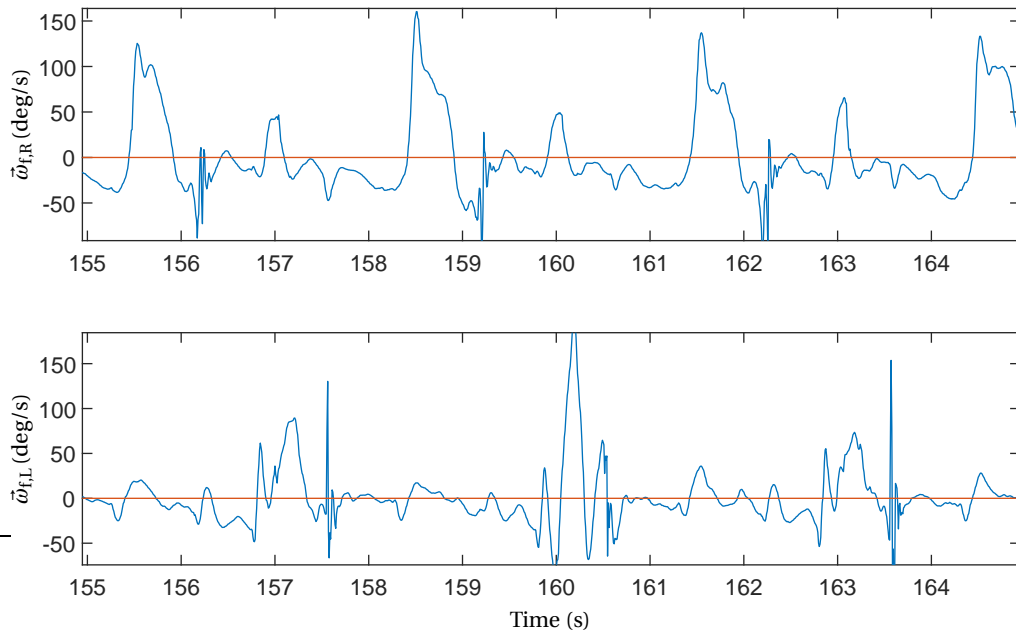


Figure B.3: Gait of the same subject as in Figure B.2, but now walking with the support of a walking aid. Note the stance phase distortion of the right foot during the swing phase of the left foot.

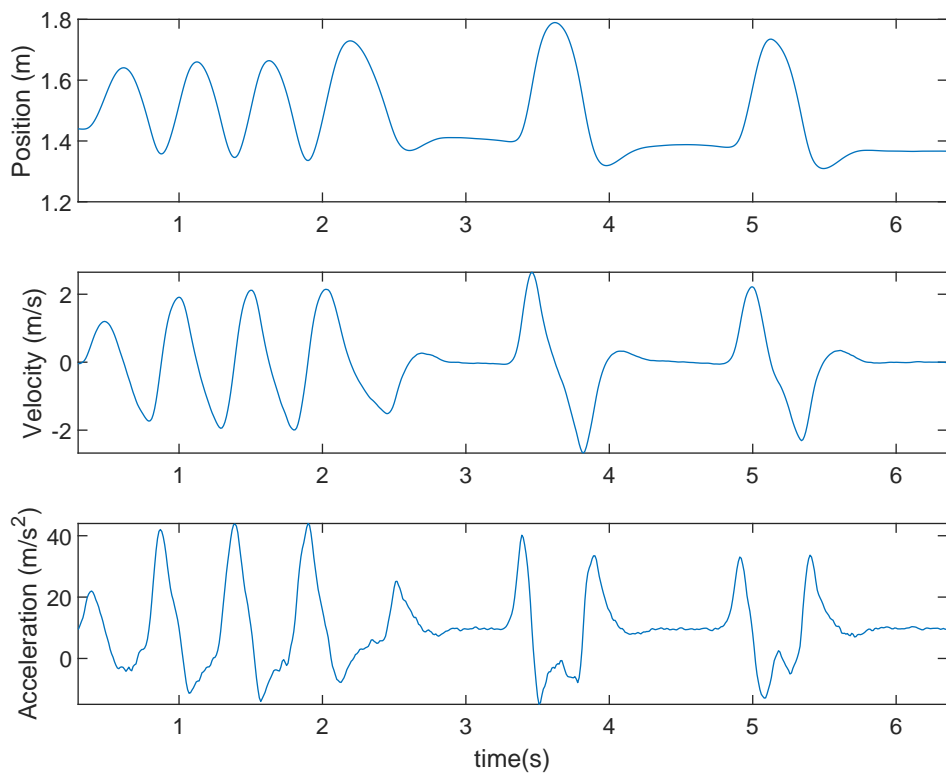


Figure B.4: Marker position vector components are double differentiated using finite central difference method to get the linear acceleration components. The vertical component is shown here. Acceleration is shown after adding gravity to it.

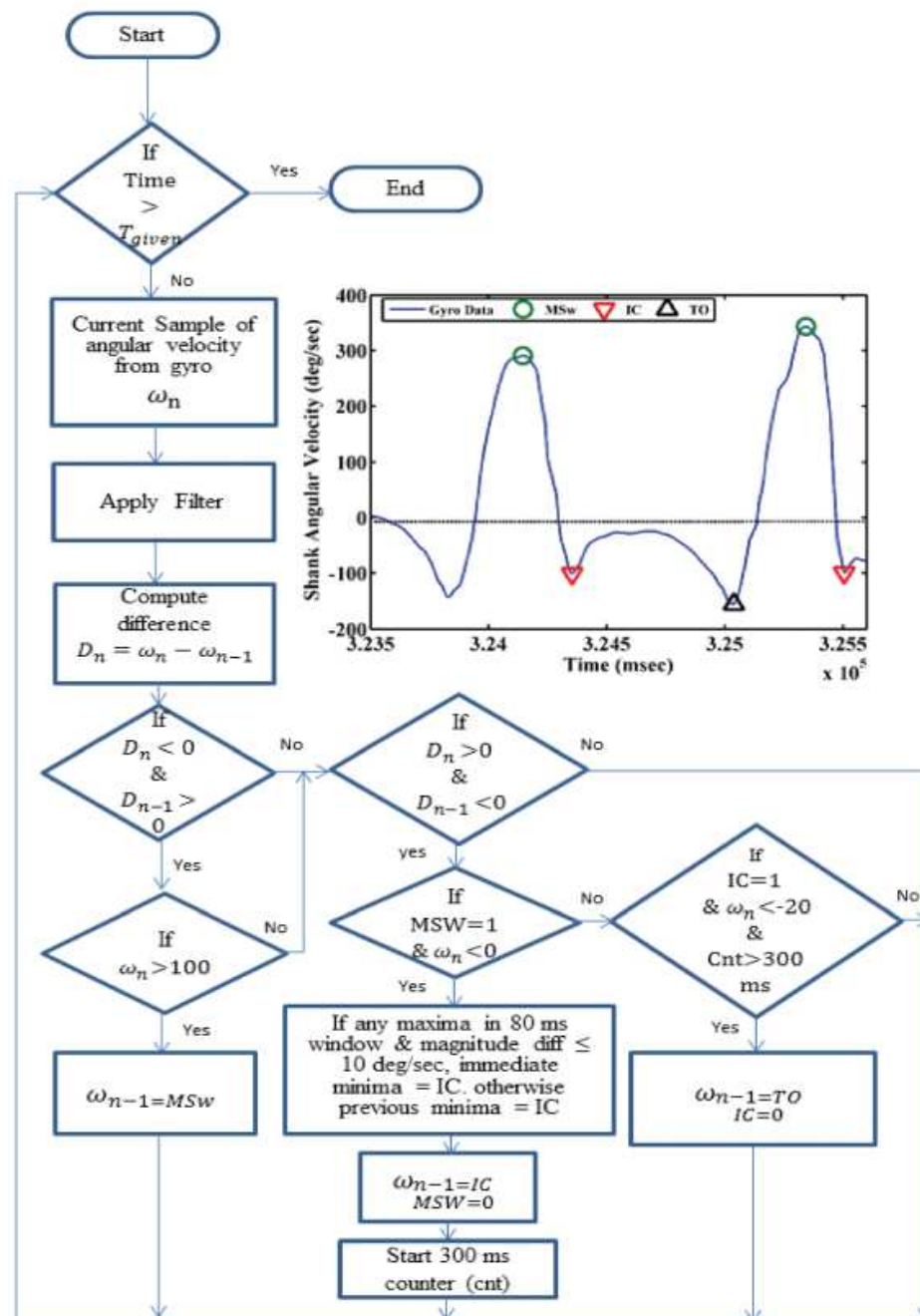


Figure B.5: Flow chart of the benchmarking method proposed in [18] for rule-based real-time gait event detection. Note that the method uses both threshold and peak detection. ©2017 IEEE. Reprinted, with permission, from [18]

C

MATLAB SCRIPT AND SETTINGS

C.1. SIMULATED REAL-TIME ENVIRONMENT

A minimal version of the MATLAB wrapper script implementing the simulated real-time testing environment is shown below:

```
%load sensor data
Fs                %Sampling frequency of sensor data
RFNormAcc         %Right foot norm of acceleration
LFNormAcc         %Left foot norm of acceleration
RFAngVel          %Right foot angular velocity
LFAngVel          %Left foot angular velocity
sensor_data_time  %actual time points of sampling as recorded in the sensor during data ...
                  collection

%set variables
wwd=2;            %Window width duration in seconds

%start system clock
tic

%simulated real-time environment for testing
while (sensor_data_time(i) < sensor_data_time(end) - wwd) %continue iteration until ...
    sensor data is available
    start_index=i;           %Starting index of window
    end_index=i+windowSize; %Ending index of window

    SearchMSt(RFNormAcc); %identify and/or update MSt interval
    SearchPSw(RFAngVel);  %identify PSw peak
    SearchTO(RFAngVel);   %identify TO
    SearchSw(RFAngVel);   %identify Sw peak
    SearchHS(RFAngVel);   %identify HS

    SearchMSt(LFNormAcc); %identify and/or update MSt interval
    SearchPSw(LFAngVel);  %identify PSw peak
    SearchTO(LFAngVel);   %identify TO
    SearchSw(LFAngVel);   %identify Sw peak
    SearchHS(LFAngVel);   %identify HS

    current_time = toc;    %copy current system clock time

    if(current_time > sensor_data_time(i) %if going slower than sensor streaming...
        rate
        [ ~, j ] = min( abs( t-current_time ) ); %skip samples
    else %else
        while(current_time < t(j)) %wait until system clock time equals ...
            current_sensor_data_time
            current_time = toc; %by updating to current system time
        end
    end
end
```

 end

C.2. MATLAB BUILT-IN FUNCTION SETTINGS

The MATLAB built-in function `findpeaks` was used extensively for peak detection. The settings of the function was largely determined from the dataset empirically and is as reported in Table C.1 below, for reproducibility. The freedom of setting parameters meant that no fine tuning was necessary and thus the concern of over-fitting was avoided to an extent. It is also to be noted that the parameters of the function were unchanged across all the nine scenarios tested, and was only updated when the sensor positions were changed. The only difference between shank and foot is the 'MinPeakProminence' value of P_{Sw} peak. This was updated empirically after observing the noticeable difference in peak prominence between P_{Sw} peaks of foot and shank.

<code>findpeaks</code>	'MinPeakHeight'	'MinPeakDistance'	'MinPeakProminence'
P _{Sw} peak (foot)	50 deg/s	1.5 s	75 deg
S _w peak (foot)	50 deg/s	1.5 s	100 deg
P _{Sw} peak (shank)	50 deg/s	1.5 s	40 deg
S _w peak (shank)	50 deg/s	1.5 s	100 deg
Trunk Peak	0.5 m/s ²	0.5 s	1.5 m/s

Table C.1: Settings used corresponding to the MATLAB built-in function's (optional) arguments.

BIBLIOGRAPHY

- [1] W. H. Organization and I. S. C. Society, *International perspectives on spinal cord injury* (World Health Organization, 2013).
- [2] S. C. Kirshblum, S. P. Burns, F. Biering-Sorensen, W. Donovan, D. E. Graves, A. Jha, M. Johansen, L. Jones, A. Krassioukov, M. Mulcahey, *et al.*, *International standards for neurological classification of spinal cord injury (revised 2011)*, *The journal of spinal cord medicine* **34**, 535 (2011).
- [3] A. Esquenazi, M. Talaty, A. Packel, and M. Saulino, *The rewalk powered exoskeleton to restore ambulatory function to individuals with thoracic-level motor-complete spinal cord injury*, *American journal of physical medicine & rehabilitation* **91**, 911 (2012).
- [4] H. C. Park, Y. S. Shim, Y. Ha, S. H. Yoon, S. R. Park, B. H. Choi, and H. S. Park, *Treatment of complete spinal cord injury patients by autologous bone marrow cell transplantation and administration of granulocyte-macrophage colony stimulating factor*, *Tissue Engineering* **11**, 913 (2005).
- [5] J. Sharp, J. Frame, M. Siegenthaler, G. Nistor, and H. S. Keirstead, *Human embryonic stem cell-derived oligodendrocyte progenitor cell transplants improve recovery after cervical spinal cord injury*, *Stem cells* **28**, 152 (2010).
- [6] J. W. McDonald, X.-Z. Liu, Y. Qu, S. Liu, S. K. Mickey, D. Turetsky, D. I. Gottlieb, and D. W. Choi, *Transplanted embryonic stem cells survive, differentiate and promote recovery in injured rat spinal cord*, *Nature medicine* **5**, 1410 (1999).
- [7] S. Grobelnik and A. Kralj, *Functional electrical stimulation-a new hope for paraplegic patients*, *Bull. Prosthet. Res* **20**, 75 (1973).
- [8] T. Bajd, B. Andrews, A. Kralj, and J. Katakis, *Restoration of walking in patients with incomplete spinal cord injuries by use of surface electrical stimulation-preliminary results*, *Prosthetics and orthotics international* **9**, 109 (1985).
- [9] F. B. Wagner, J.-B. Mignardot, C. G. Le Goff-Mignardot, R. Demesmaeker, S. Komi, M. Capogrosso, A. Rowald, I. Seáñez, M. Caban, E. Pirondini, M. Vat, L. A. McCracken, R. Heimgartner, I. Fodor, A. Watrin, P. Seguin, E. Paoles, K. Van Den Keybus, G. Eberle, B. Schurch, E. Pralong, F. Becce, J. Prior, N. Buse, R. Buschman, E. Neufeld, N. Kuster, S. Carda, J. von Zitzewitz, V. Delattre, T. Denison, H. Lambert, K. Minassian, J. Bloch, and G. Courtine, *Targeted neurotechnology restores walking in humans with spinal cord injury*, *Nature* **563**, 65 (2018).
- [10] M. L. Gill, P. J. Grahm, J. S. Calvert, M. B. Linde, I. A. Lavrov, J. A. Strommen, L. A. Beck, D. G. Sayenko, M. G. Van Straaten, D. I. Drubach, *et al.*, *Neuromodulation of lumbosacral spinal networks enables independent stepping after complete paraplegia*, *Nature medicine* , 1 (2018).
- [11] N. Wenger, E. M. Moraud, J. Gandar, P. Musienko, M. Capogrosso, L. Baud, C. G. Le Goff, Q. Barraud, N. Pavlova, N. Dominici, *et al.*, *Spatiotemporal neuromodulation therapies engaging muscle synergies improve motor control after spinal cord injury*, *Nature medicine* **22**, 138 (2016).
- [12] J. V. Hari Prasanth, Heike Vallery, *Wearable sensor based real-time gait analysis: A systematic review*, (2018).
- [13] L. Yang, S. Ye, Z. Wang, Z. Huang, J. Wu, Y. Kong, and L. Zhang, *An error-based micro-sensor capture system for real-time motion estimation*, *Journal of Semiconductors* **38**, 105004 (2017).
- [14] G. Reganha, *Closed-loop control of spatiotemporal stimulation of the spinal cord based on wearable inertial sensors*, Master's thesis, Ecole Polytechnique Federale De Lausanne (2017).

- [15] L. Van Nguyen and H. M. La, *Real-time human foot motion localization algorithm with dynamic speed*, IEEE Transactions on Human-Machine Systems **46**, 822 (2016).
- [16] A. Behboodi, H. Wright, N. Zahradka, and S. Lee, *Seven phases of gait detected in real-time using shank attached gyroscopes*, in *Engineering in Medicine and Biology Society (EMBC), 2015 37th Annual International Conference of the IEEE* (IEEE, 2015) pp. 5529–5532.
- [17] J. K. Lee and E. J. Park, *Quasi real-time gait event detection using shank-attached gyroscopes*, Medical & biological engineering & computing **49**, 707 (2011).
- [18] H. F. Maqbool, M. A. B. Husman, M. I. Awad, A. Abouhossein, N. Iqbal, and A. A. Dehghani-Sanij, *A real-time gait event detection for lower limb prosthesis control and evaluation*, IEEE transactions on neural systems and rehabilitation engineering **25**, 1500 (2017).
- [19] J. Rueterbories, E. G. Spaich, B. Larsen, and O. K. Andersen, *Methods for gait event detection and analysis in ambulatory systems*, Medical Engineering and Physics **32**, 545 (2010).
- [20] A. U. Alahakone, S. A. Senanayake, and C. M. Senanayake, *Smart wearable device for real time gait event detection during running*, in *Circuits and Systems (APCCAS), 2010 IEEE Asia Pacific Conference on* (IEEE, 2010) pp. 612–615.
- [21] D. J. Villarreal, H. A. Poonawala, and R. D. Gregg, *A robust parameterization of human gait patterns across phase-shifting perturbations*, IEEE Transactions on Neural Systems and Rehabilitation Engineering **25**, 265 (2017).
- [22] D. Quintero, D. J. Lambert, D. J. Villarreal, and R. D. Gregg, *Real-time continuous gait phase and speed estimation from a single sensor*, in *Control Technology and Applications (CCTA), 2017 IEEE Conference on* (IEEE, 2017) pp. 847–852.
- [23] G. Chen, P. Qi, Z. Guo, and H. Yu, *Gait-event-based synchronization method for gait rehabilitation robots via a bioinspired adaptive oscillator*, IEEE Transactions on Biomedical Engineering **64**, 1345 (2017).
- [24] T. Yan, A. Parri, V. R. Garate, M. Cempini, R. Ronsse, and N. Vitiello, *An oscillator-based smooth real-time estimate of gait phase for wearable robotics*, Autonomous Robots **41**, 759 (2017).
- [25] F. MARTEL, *Control of an active implanted device for spinal cord injury rehabilitation*, Master's thesis, Ecole Polytechnique Federale De Lausanne (2017).
- [26] T. Yoshida, F. Mizuno, T. Hayasaka, K. Tsubota, Y. Imai, T. Ishikawa, and T. Yamaguchi, *Development of a wearable surveillance system using gait analysis*, Telemedicine and e-Health **13**, 703 (2007).
- [27] D. Han, V. Renaudin, and M. Ortiz, *Smartphone based gait analysis using stft and wavelet transform for indoor navigation*, in *Indoor Positioning and Indoor Navigation (IPIN), 2014 International Conference on* (IEEE, 2014) pp. 157–166.
- [28] L. Klingbeil, T. Wark, and N. Bidargaddi, *Efficient transfer of human motion data over a wireless delay tolerant network*, in *Intelligent Sensors, Sensor Networks and Information, 2007. ISSNIP 2007. 3rd International Conference on* (IEEE, 2007) pp. 583–588.
- [29] D. T. Lee and A. Yamamoto, *Wavelet analysis: theory and applications*, Hewlett Packard journal **45**, 44 (1994).
- [30] O. Rioul and M. Vetterli, *Wavelets and signal processing*, IEEE signal processing magazine **8**, 14 (1991).
- [31] K. Aminian, B. Najafi, C. Büla, P.-F. Leyvraz, and P. Robert, *Spatio-temporal parameters of gait measured by an ambulatory system using miniature gyroscopes*, Journal of biomechanics **35**, 689 (2002).
- [32] N. Abaid, P. Cappa, E. Palermo, M. Petrarca, and M. Porfiri, *Gait detection in children with and without hemiplegia using single-axis wearable gyroscopes*, PloS one **8**, e73152 (2013).
- [33] J. Taborri, S. Rossi, E. Palermo, F. Patanè, and P. Cappa, *A novel hmm distributed classifier for the detection of gait phases by means of a wearable inertial sensor network*, Sensors **14**, 16212 (2014).

-
- [34] W. Chen, Y. Xu, J. Wang, and J. Zhang, *Kinematic analysis of human gait based on wearable sensor system for gait rehabilitation*, *Journal of Medical and Biological Engineering* **36**, 843 (2016).
- [35] M. Derawi and P. Bours, *Gait and activity recognition using commercial phones*, *computers & security* **39**, 137 (2013).
- [36] E. Pignat, *Wearable sensors for robust gait event detection*, Master's thesis, Ecole Polytechnique Federale De Lausanne (2015).
- [37] R. Chereshevnev and A. Kertész-Farkas, *Hugadb: Human gait database for activity recognition from wearable inertial sensor networks*, in *International Conference on Analysis of Images, Social Networks and Texts* (Springer, 2017) pp. 131–141.
- [38] G. B. Moody, R. G. Mark, and A. L. Goldberger, *Physionet: a web-based resource for the study of physiologic signals*, *IEEE Engineering in Medicine and Biology Magazine* **20**, 70 (2001).
- [39] S. Zheng, K. Huang, T. Tan, and D. Tao, *A cascade fusion scheme for gait and cumulative foot pressure image recognition*, *Pattern Recognition* **45**, 3603 (2012).
- [40] R. van der Linde and A. L. Schwab, *Multibody dynamics b lecture notes*, (1997).
- [41] R. M. Murray, *A mathematical introduction to robotic manipulation* (CRC press, 2017).